# SPACE SHUTTLE PROXIMITY OPERATION SENSOR STUDY

FINAL REPORT

Contract No. NAS 9-15502

Prepared for

NASA Lyndon B. Johnson Space Center
Houston, Texas 77058

Prepared by

Charles L. Weber
Waddah K. Alem

Axiomatix
13900 Panay Way, Suite 110M
Marina del Rey, California 90291

Axiomatix Report No. R7802-2
February 15, 1978



[redacted]

Axiomatix



Marina del Rey • California

TABLE OF CONTENTS


| | | Page |
|---|---|---|
| LIST OF TABLES | | iv |
| LIST OF FIGURES | | v |
| 1.0 | INTRODUCTION AND SUMMARY | 1 |
| 1.1 | Recommendation for Angle and Angle Rate Tracking Problem at Close Ranges | 2 |
| 1.2 | Ku-Band Radar Simulation | 4 |
| 2.0 | TARGET ACQUISITION - PASSIVE TARGET | 5 |
| 2.1 | Target Detection Processing Losses | 6 |
| 2.2 | Radar Detection Performance Philosophy | 11 |
| 2.3 | Radar Detection Performance | 11 |
| 2.4 | Alternatives and Recommendations | 18 |
| 3.0 | POINT TARGET TRACKING | 21 |
| 3.1 | Thermal Noise and Target Scintillation Effects on Tracking Accuracies for Passive Point Targets | 21 |
| 3.1.1 | Angle and Angle Rate Tracking Accuracies | 22 |
| 3.1.2 | Range Tracking Accuracies | 26 |
| 3.1.3 | Range Rate Tracking Accuracy | 30 |
| 3.2 | Effects of Point Target Accelerations | 33 |
| 3.2.1 | Introduction | 33 |
| 3.2.2 | Radial Accelerations | 33 |
| 3.2.3 | Tangential Acceleration | 37 |
| 3.2.4 | Angular Acceleration Testing | 44 |
| 4.0 | SIMULATION AT SHORT RANGE | 49 |
| 4.1 | Simulation of Thermal Noise and Target Scintillation Effects | 51 |
| 4.1.1 | Tracking Error Simulation Due to Thermal Noise and Target Scintillation in Range, Angle, and Angle Rate Tracking | 51 |
| 4.1.2 | Stochastic Process Modeling | 54 |
| 4.1.3 | Software Implementation | 58 |
| 4.1.4 | Tracking Errors Simulation Due to Thermal Noise and Target Scintillation in Range Rate Tracking | 60 |
| 4.2 | Radar Simulation of Relative Accelerations | 62 |
| 4.2.1 | Closed Loop Transfer Functions | 62 |
| 4.2.2 | Digital Simulation Algorithms for Acceleration | 68 |
| 4.3 | Range Rate Logarithmic Discriminant Error Simulation | 72 |

Page

4.3.1 Finding the Doppler Offset $\Delta f_d$ . . . . . 74
4.3.2 Methods for Finding the Error . . . . . 76

4.4 Simulation of Target Effects . . . . . 78

4.4.1 Target Effects on Range Errors . . . . . 78
4.4.2 Target Effects on Range Rate Errors . . . . . 81
4.4.3 Target Effects on the Angle Tracking Loop . . . 83
4.4.4 Target Effects on Angle Rate Estimation . . . . 89

4.5 Overall Description of Ku-Band Radar Simulation . . . 89

4.5.1 Range Error Simulation . . . . . 92
4.5.2 Range Rate Error Simulation . . . . . 92
4.5.3 Angle and Angle Rate Error Simulation . . . . . 96
4.5.4 Additional Comments . . . . . 96

5.0 ELECTRO-OPTICAL DOCKING TECHNIQUES . . . . . 99

5.1 Analysis of Ranging Techniques . . . . . 99

5.1.1 Triangulation . . . . . 99

5.2 Direct Rangefinder (No Angle Measurement) . . . . . 105
5.3 Description of Electro-Optical Concepts . . . . . 107

5.3.1 Cooperative Satellites . . . . . 109
5.3.2 Noncooperative Satellites . . . . . 113

REFERENCES . . . . . 115

APPENDIX A. MODELING A CONTINUOUS STOCHASTIC PROCESS BY A DISCRETE TIME STOCHASTIC PROCESS . . . . . 116

LIST OF TABLES


| | | Page |
|---|---|---|
| 1. | Summary of Target Detection Processing Losses . . . . . | 7 |
| 2. | Doppler Mismatch Losses of DFT Filters . . . . . | 7 |
| 3. | Summary of Tracking Loop Parameters (Passive Target) . . . | 23 |
| 4. | $\alpha$-$\beta$ Tracker Parameters . . . . . | 35 |
| 5. | Angle Tracking Loop Parameters . . . . . | 37 |
| 6. | Tracking Loop Parameters . . . . . | 55 |
| 7. | General Transfer Function Parameters . . . . . | 55 |
| 8. | Discriminants for Acceleration Transfer Functions . . . . . | 67 |
| 9. | Typical Case of Proximity Operations Range Errors . . . . . | 94 |
| 10. | Proximity Operations Range Rate Errors . . . . . | 94 |

LIST OF FIGURES


| | | Page |
|---|---|---|
| 1. | General Block Diagram for Slaving Ku-Band Antenna to Two TV Cameras at Short Ranges | 3 |
| 2. | Antenna Beam Shape Loss Description | 8 |
| 3. | Range Straddling Loss in Undesignated Mode of Detection | 10 |
| 4. | Target Detection Design Margin Versus Range for Worst Case Losses in Table 1 | 12 |
| 5. | Target Detection Design Margins Versus Range for Average Losses in Table 1 | 13 |
| 6. | Cumulative Detection Probability Versus Range for Worst Case Losses in Table 1 | 15 |
| 7. | Cumulative Probability of Detection Versus Range for Average Losses in Table 1 | 16 |
| 8. | Cumulative Probability of Detection Versus Scan Time for Various Ranges | 17 |
| 9. | Cumulative Detection Probability Versus Range for Various Scans | 19 |
| 10. | Angle Tracking Error of Passive Point Target Due to Thermal Noise and Target Scintillation Versus Range | 24 |
| 11. | Angle Rate Estimation of a Passive Point Target Due to Thermal Noise and Target Scintillation Versus Range | 25 |
| 12. | RMS Range Tracking Error of Point Passive Targets Versus Range | 27 |
| 13. | Specification for Three-Sigma Random Range Error Versus LOS Range | 28 |
| 14. | RMS Range Tracking Error of Passive Point Targets at Close Range Versus Range | 29 |
| 15. | RMS Range Rate Tracking Error Due to Thermal Noise and Target Scintillation of Passive Point Targets Versus Range (Long Ranges) | 31 |
| 16. | RMS Range Rate Tracking Error Due to Thermal Noise and Target Scintillation of Passive Point Targets Versus Range (Short Ranges) | 32 |

| | | Page |
|---|---|---|
| 17. | Radial and Tangential Accelerations | 34 |
| 18. | Deterministic Range Tracking Loop | 35 |
| 19. | Range Error Due to Constant Acceleration Lasting T Seconds (R = 10 nmi) | 38 |
| 20. | Range Error Due to Constant Acceleration Lasting T Seconds (R = 2 nmi) | 39 |
| 21. | Deterministic Angle Tracking Loop | 40 |
| 22. | Angle Error Due to Tangential Acceleration With Range as a Parameter | 42 |
| 23. | Angle Error Due to Acceleration With Burn Time as a Parameter | 43 |
| 24. | Angle Rate Error Due to Acceleration With Range as a Parameter | 45 |
| 25. | Angle Rate Error Due to Acceleration With Burn Time as a Parameter | 46 |
| 26. | Radar Angle Tracking Testing | 47 |
| 27. | General Block Diagram of Orbital Simulation and the Simulation of the Ku-Band Radar | 50 |
| 28. | Range Tracking Loop Block Diagram | 52 |
| 29. | Angle Tracking Loop Block Diagram Showing Angle Rate Estimator | 52 |
| 30. | Continuous Stochastic Model | 54 |
| 31. | Diagram of Discrete Time Model for Range and Angle Tracking Loops | 59 |
| 32. | $\sigma_X$ Versus SNR for Range, Angle and Range Rate Tracking Loops | 61 |
| 33 | Simulation - Range Rate - Thermal Noise and Amplitude Scintillation Errors | 63 |
| 34. | Range Tracking Loop Without Noise | 64 |
| 35. | Angle Tracking Loop with Angle Rate Estimation Without Noise | 66 |
| 36. | General Block Diagram of Digital Simulation for Acceleration | 69 |

Page

37. Direct Recursive Realization . . . . . 70

38. Canonic Realization . . . . . 70

39. Parallel Canonic Realization . . . . . 71

40. The Mean of the Logarithmic Discriminant Output Versus Normalized Doppler Offset . . . . . 73

41. Doppler Filter Configuration in Track Mode . . . . . 75

42. Range Rate Log Discriminant Error, Using HAC Method . . . . 77

43. Analog Model of Target Effects on Range Errors . . . . . 78

44. Description of Rotating Target Dimensions . . . . . 80

45. Simulation of Target Effects in Range . . . . . 82

46. Analog Model of Target Effects on Range Rate Errors . . . . 83

47. Simulation - Target Effects in Range Rate . . . . . 84

48. Angle Errors Due to Target Effects . . . . . 85

49. Angle Errors Due to Target Effects . . . . . 87

50. Range at Which the Antenna Field of View is Filled . . . . 88

51. Angle Rate Errors From Angle Errors Due to Target Effects . . . . . 90

52. Angle Rate Errors Due to Target Effects . . . . . 91

53. Range Error Simulation . . . . . 93

54. PDF for Data Staleness Model . . . . . 94

55. Range Rate Errors Simulation . . . . . 95

56. Angle and Angle Rate Error Simulation . . . . . 97

57. Two-Pole Butterworth Response to a Pulse of 0.122 μsec . . 98

58. Co-Planar Case of Triangulation . . . . . 101

59. Special Case of Co-Planar Triangulation (b = a) . . . . . 101

60. Angle Error Budget Versus Range for Fixed RMS Range Precision . . . . . 103

Page

61. RMS Range Error Versus Range for Fixed Angle Error . . . . 104

A-1. White Noise Through a First-Order Filter . . . . . 120

A-2. Diagram of Discrete Time Model for First-Order Stochastic Process . . . . . 121

# 1.0 INTRODUCTION AND SUMMARY

The Orbiter Ku-band radar is presently being developed [2] the hope is that the present design is "molded in concrete" as much as possible. With that in mind, when problem areas arise in the radar performance, the solutions recommended in this report are those which involve minimum cost, minimum (essentially zero) design changes in hardware, and little variation in software development.

The performance of the Ku-band radar is analyzed in detail in [1], and the performance is updated and summarized in sections 2.0 and 3.0 of this report. In so doing, two different radar design philosophies are described, and the corresponding differences in losses are enumerated. The resulting design margins are determined for both design philosophies and for both the designated and nondesignated range modes of operation. In some cases, the design margin is about zero, and in other cases it is significantly less than zero (-4 to -5 dB). With the point of view described above, the recommended solution is to allow more scan time (2 minutes as opposed to 1 minute) but at the present scan rate. With no other changes in the present configuration, the radar will meet design detection specifications for all design philosophies at a range of 11.3 nautical miles.

In the tracking mode, the Ku-band radar meets specifications satisfactorily at all ranges in the range and range rate tracking loops. This is with the assumption, however, that there is no significant degradation due to angle tracking errors. As is shown in sections 3.0 and 4.0, this is not the case. At short ranges, the angle tracking loop and angle rate estimator are not reliable with the present configuration The reason for this is primarily due to target glint effects which can and do become significant when the target fills more than 10% of the 3 dB beamwidth of the antenna pattern. In addition, the monopulse difference patterns are unpredictable at short ranges. In the next section, the recommended solution to this problem is described. This solution is effective in all dimensions of the point of view described above.

## 1.1 Recommendation for Angle and Angle Rate Tracking Problem at Close Ranges

A rough description of the suggested solution to the proximity operations problem in the angle tracking loop of the Ku-band radar is presented. The approach centers around slaving the Ku-band antenna to the TV camera during a portion of the approach phase in the rendezvous and docking of a target.

The situation with the present configuration is as follows: There is a transition period during approach in which neither the Ku-band radar nor the two TV systems individually provide all the desired information at acceptable accuracies to carry out a rendezvous and docking profile. Using the two TV systems and the Ku-band radar, however, all of the necessary position and velocity information can be satisfactorily obtained.

There is presently a TV camera at each end of the Shuttle's stowage bay. Each camera has an 8:1 zoom lens and is mounted on a pan and tilt, thereby giving each camera two degrees of angular freedom. In addition, each pan and each tilt is encoded into a video signal using a Binary Gray Code of 11 bits. This corresponds to angular intervals of 0.18 degrees. The accuracy off each shaft has been quoted as 0.3 degrees. These four encoded angular signals are readily available at the pans and tilts. The operations interface (OI-MDM) does not presently receive this angular information, and the information is not now being telemetered back to a ground station. However, these video signals with the angular information can easily be sent to the OI-MDM interface. This is shown as connecting lines (a) in Figure 1. Also, both TV cameras can presently be simultaneously monitored by the rendezvous operator on two adjacent CRTs.

The Ku-band presently "talks" to an MDM, as shown in Figure 1. As described in sections 3.0 and 4.0, the angle and angle rate accuracies of the radar become unacceptable at a larger range than do the accuracies of range and range rate. When the radar provides no useful angle and angle rate information, however, the antenna must clearly be kept pointed toward the target in order to provide accurate range and range rate information.

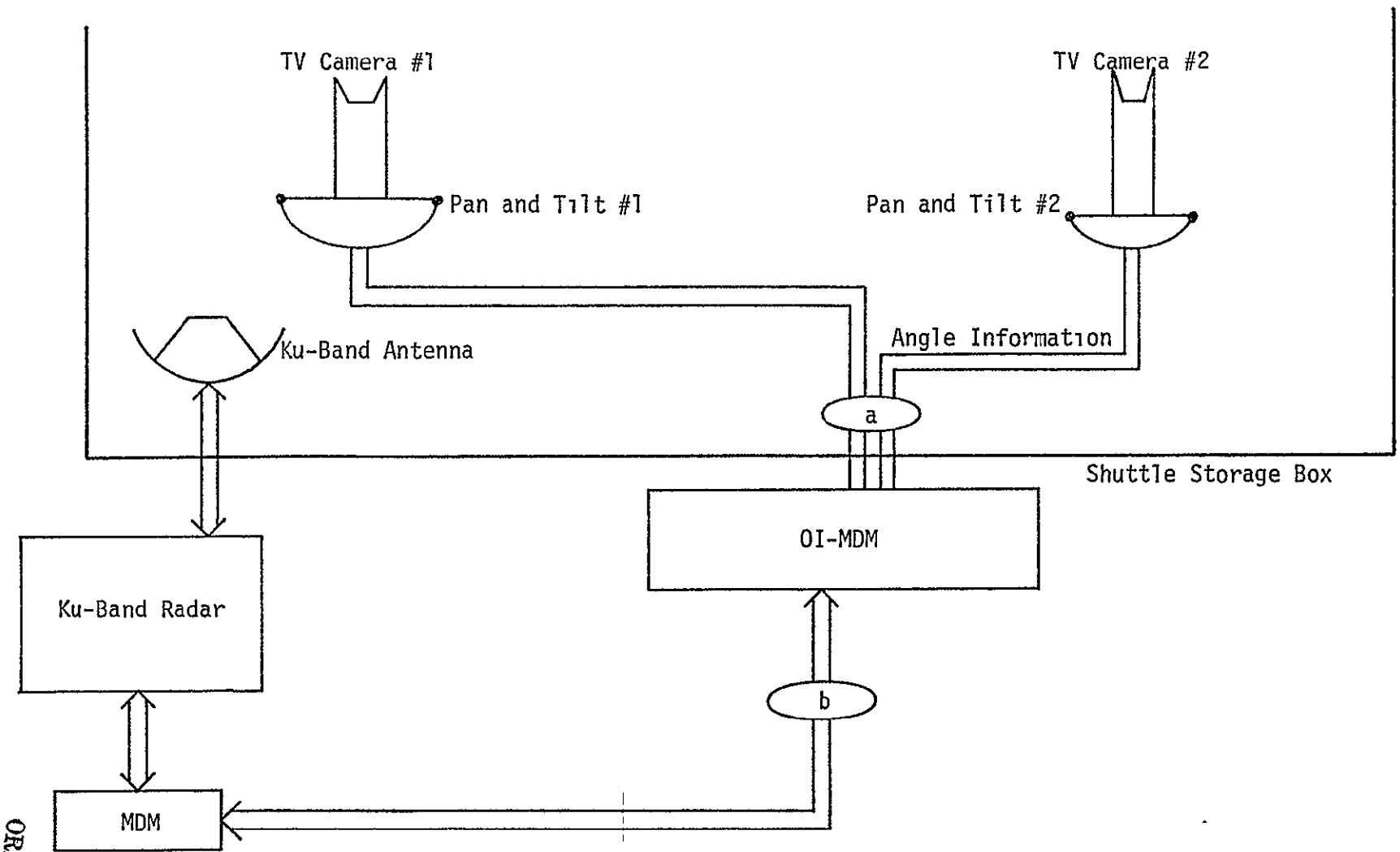


Figure 1. General Block Diagram for Slaving Ku-Band Antenna to Two TV Cameras at Short Ranges

The suggested solution would slave the Ku-band antenna to the TV cameras, which are manually pointed toward the target. Both TV cameras would be used, and a relatively simple software algorithm would be developed to best use this information to direct the Ku-band antenna toward the target. To accomplish this, a communication link (cable) would have to be created so that the MDM and OI-MDM can "talk" to each other. From a hardware implementation and cost point of view, this appears to be the largest item and should be nominal compared to all the other alternatives that have been examined (primarily the addition of a laser or lasers). These alternatives are described in section 5.0 of this report.

In summary, the suggested solution requires cable and software development. Neither of these, however, appears to be extensive.

## 1.2 Ku-Band Radar Simulation

A model of the Ku-band radar has been developed and is presented in section 4.0 of this report The model is described such that it is directly programmable into a digital simulation. It can operate in "real time" with a man in the loop and with arbitrary maneuvers in the orbital geometry. Some minimal computation rate will be necessary, however, in order to operate in real time.

The model is given as a simulation modular package so that it can be placed in any of the present Orbiter simulations at NASA JSC with minor interfacing.

One of the purposes of the digital simulation of the Orbiter Ku-band radar is to determine operating procedures when operating manually. This is particularly pressing with the present radar schedule due to the Skylab trajectory [13].

The successful completion and operation of the proposed radar simulation should add significant confidence to the concept that satellites can indeed be tracked and docked and a complete rendezvous performed. Some of the example performance computations are carried out for the LDEF Satellite.

## 2.0 TARGET ACQUISITION - PASSIVE TARGET

A significant part of the overall proximity operation of the Ku-band radar is the capability to detect and re-acquire the target at all ranges less than 10 nmi. The acquisition capability of the present configuration of the Ku-band radar is summarized in this section. The development in Appendix A of [1] is used extensively.

There are several facts which are used as assumptions and taken advantage of when assessing the acquisition capability of the Ku-band radar. These assumptions are actually assets, in particular:

(a) The target size is known. Other properties are known, such as shape, composition, and possibly even the average radar cross-section (RCS) This provides preliminary information about expected target strength at the time of acquisition.

(b) The target's angular rotation is small. This is a self-evident requirement if a rendezvous and eventual placement into the Shuttle payload bay is to be carried out.

(c) There exists no jamming. The passive targets will be truly passive, and the active targets will be cooperative. No additional signals of an interfering or jamming nature are anticipated.

(d) In almost all configurations, there exists no clutter. The only possible exception is when the target is directly below the Shuttle and the radar sees earth clutter. If clutter does present a problem, various methods have been suggested to overcome it, including the appropriate rate of frequency hopping.

(e) One possible situation is AGC saturation in the detection mode at close ranges. This is expected to be highly unlikely because detection at close ranges invariably will be a reacquisition. In that case, the TWT is either attenuated or removed so that the power level will not cause AGC saturation during at least a portion of the short range detection time.

The primary emphasis in the evaluation of the Ku-band radar during acquisition is "how the radar performs." Comparison will be made to the specification values, but no heavy emphasis is placed on it. In those situations where the performance does not meet the specification requirements, reasonable alternatives are proposed which will provide satisfactory performance in all rendezvous profiles.

## 2.1 Target Detection Processing Losses

The target detection processing losses as they are presently estimated are summarized in Table 1. The losses anticipated by both Hughes and Axiomatix are shown. The reasons for the agreements and disagreements and the resulting philosophies in radar performance are as follows:

The transmit loss is a hardware loss. It is presently estimated at 3.7 dB by Hughes, and Axiomatix believes this is a realistic value.

The beam shape loss is listed as an average of 2 dB by Hughes and 3.2 dB maximum by Axiomatix. The difference is seen by inspection of Figure 2. If a target remained at boresight during its entire period of illumination, the antenna beam shape loss would be zero. The target location for maximum beam shape loss is also shown in Figure 2. The loss for this path is the one used by Axiomatix. If the beam shape loss is averaged over the region indicated in Figure 2, the result is approximately 2 dB when the scan overlap is 15% to 30%. This average is reasonably insensitive to the amount of overlap when the scan overlap is within this region. For a detailed analytical description of beam shape loss, see [4].

The pre-sum mismatch has been evaluated as 0.57 dB in Appendix A of [1] for the parameters of the Ku-band radar. Hughes also uses this value.

The constant F.A.P. loss has been set at 1.7 dB. This is an approximation and is an area which deserves more study.

The doppler mismatch is a loss of signal gain due to the fact that the doppler frequency is not at the center of one of the filters in the DFT. The loss varies from 0 dB to 3.9 dB, with an average of approximately 1.1 dB.

For an N point DFT, the filter transfer function is given by [1]:

$$F(\Delta f) = \frac{\sin\left(2\pi \Delta f N \frac{T_p}{2}\right)}{N \sin\left(2\pi \Delta f \frac{T_p}{2}\right)}, \qquad (1)$$

where $\Delta f$ = frequency difference from the center of the doppler filter to the doppler frequency of the target

Table 1. Summary of Target Detection Processing Losses

| | | Hughes (average) (dB) | Axiomatix (worst case) (dB) |
|---|---|---|---|
| Transmit Loss | | 3.7 | 3.7 |
| Beam Shape Loss | | 2 (avg) | 3.2 (max) |
| Pre-Sum Mismatch | | 0.57 | 0.57 |
| Constant FAP | | 1.7 | 1.7 |
| Doppler Mismatch | | 1.1 (avg) | 3.9 (max) |
| Range Gate Straddle | | | |
| | Designated Mode | 1.76 | 1.76 |
| | Undesignated Mode | $L_{str} = f(R)$ | $L_{str} = f(R)$ |
| Processor Loss | | 1.25 | 1.25 |
| Totals | Designated Mode | 12.08 | 16.08 |
| | Undesignated Mode | $10.32 + L_{str}$ | $14.32 + L_{str}$ |

Table 2. Doppler Mismatch Losses of DFT Filters

| N = | 1 | 2 | 4 | 8 | 16 | 32 |
|---|---|---|---|---|---|---|
| Average Loss (dB) | 0 | -0.871 | -1.055 | -1.100 | -1.111 | -1.113 |
| Maximum Loss (dB) | 0 | -3.010 | -3.698 | -3.867 | -3.908 | -3.919 |

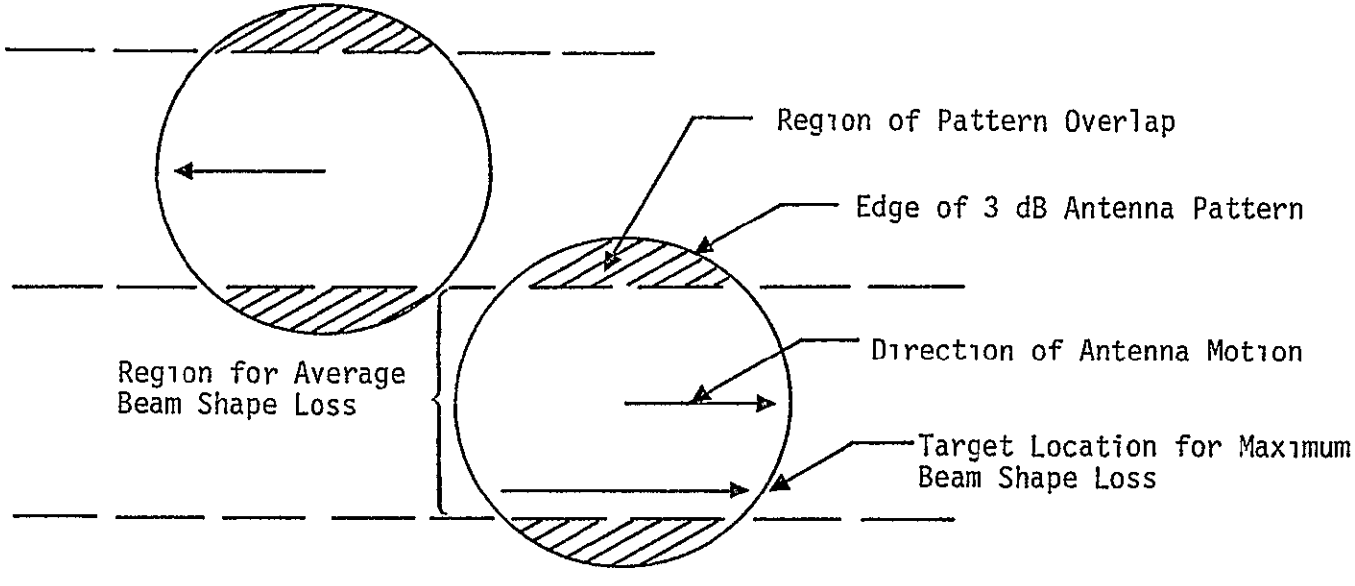


Figure 2. Antenna Beam Shape Loss Description

N = number of points in the DFT

$T_p = [PRF]^{-1}$ seconds.

The filters are placed $(NT_p)^{-1}$ Hz apart, so that the maximum value of $\Delta f$ is $(2NT_p)^{-1}$, at which value maximum signal strength moves to the adjacent filter in the DFT.

The value of $|F(\Delta f)|^2$ at $\Delta f = 0$ is 0 dB. The peak loss occurs at $\Delta f = (2NT_p)^{-1}$, which is given by

$$\text{Maximum Loss} = |F(\Delta f)|^2 \Big|_{\Delta f = \frac{1}{2NT_p}} = \left| \frac{1}{N \sin(\pi/2N)} \right|^2 . \quad (2)$$

The average loss is evaluated from

$$\text{Avg Loss} = \left(\frac{1}{2NT_p}\right) \int_0^{\left(\frac{1}{2NT_p}\right)} |F(\Delta f)|^2 \, d(\Delta f) = \int_0^1 \left| \frac{\sin(\pi x/2)}{N \sin(\pi x/(2N))} \right|^2 dx . \quad (3)$$

These doppler mismatch losses have been computed, and the results are shown in Table 2 for various values of N. The present radar has an N = 16 point DFT, which results in 1.11 dB average loss and 3.90 dB maximum loss. These numbers are used for the doppler mismatch loss in Table 1.

The range gate straddling loss [1, Appendix A] is 1.76 dB in the range designate mode. This is a factor of 1.5 (1.76 in dB), which arises since the range gates during acquisition are 1.5 times wider than the pulse width. In the undesignated mode, the range gate straddling loss is a function of range and is plotted in Figure 3. This variation in range is taken into account in evaluating detection performance.

At a PRF of approximately 3 kbps, the unambiguous range is approximately 27 nmi. As the range gets close to multiples of 27 nmi, the SNR must get arbitrarily large for detection to take place, due to eclipsing of the received pulse by a new transmitted pulse. When the radar is operating in the cooperative mode with an active target, the unambiguous range increases to 300 nmi. The SNR clearly is a problem at ranges much above 10 nmi, and acquisition is not expected to be reliable.

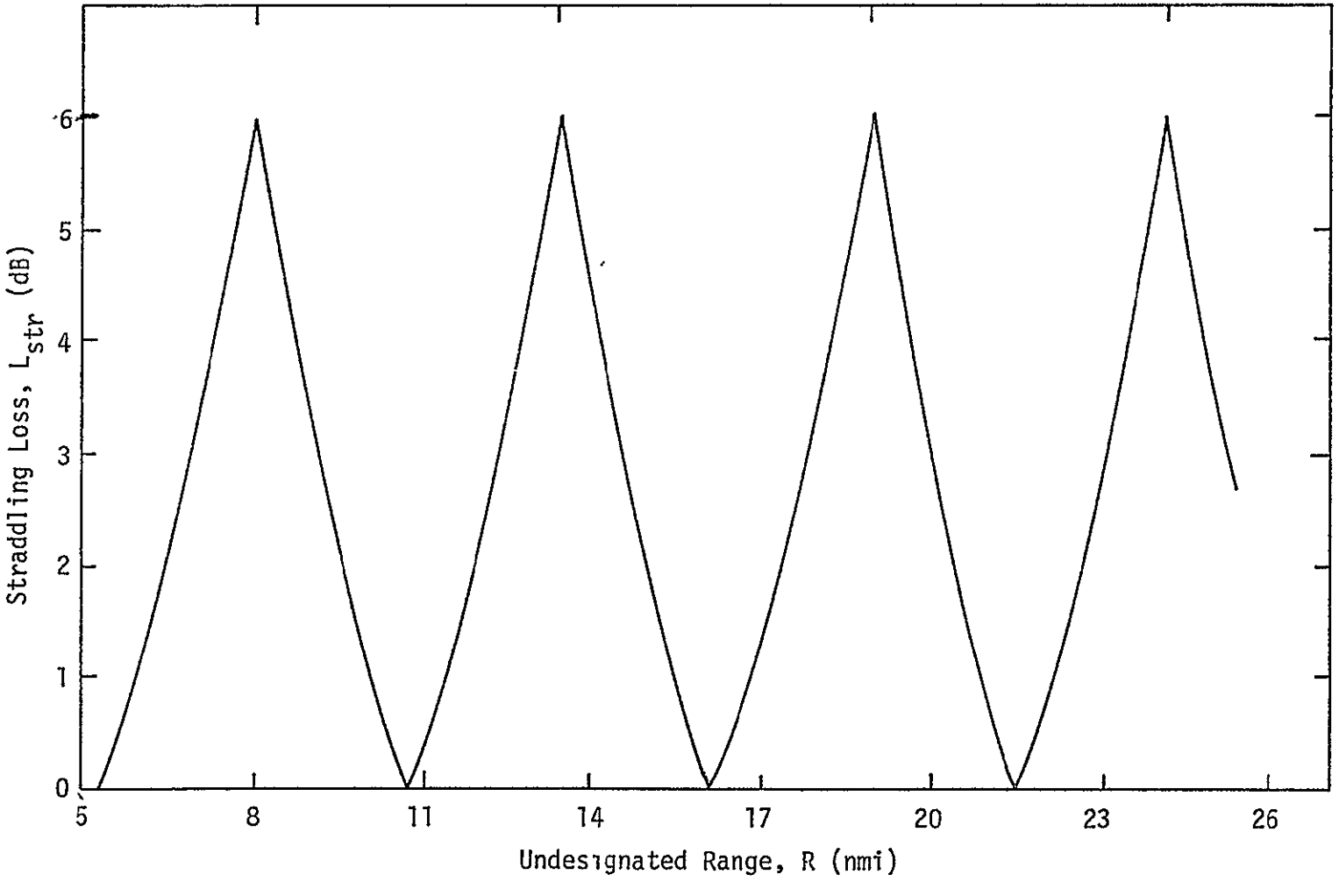


Figure 3. Range Straddling Loss in Undesignated Mode of Detection

The last loss that has been accounted for is a processor algorithm loss Most of the algorithms are approximations to the ideal computation. Although the loss is small in each algorithm, the cumulative effect of all of these approximations is estimated to be approximately 1.25 dB.

The totals of the losses in Figure 3 are used in evaluating radar detection performance in section 2.3. It is noted that the difference between the average losses and worst case losses is 4.0 dB. In the next section, the differences in these losses and their implications are discussed.

## 2.2 Radar Detection Performance Philosophy

The losses enumerated in the last section demonstrate two approaches in establishing a radar detection performance philosophy. The differences center around what is to be taken into account when averages are performed. The "Hughes" approach is to average over all target positions and velocities when carrying out an average. The "Axiomatix" approach is somewhat more pessimistic in that the average is carried out over thermal noise, target scintillation effects, and other radar parameters. This is done, however, for a target located at the worst possible velocity and worst possible angular position.

We believe there is merit to both approaches. Therefore, the detection results to be subsequently presented are carried out under both performance philosophies.

In the one case, the design philosophy is that

$$\text{Average } P_d = 0.99 \tag{4}$$

for a 1 square meter target. In the latter case, the design philosophy is

$$\text{Average } P_d \geq 0.99 \tag{5}$$

for a 1 square meter target for all target velocities and spatial positions.

## 2.3 Radar Detection Performance

Based on the losses discussed in the previous sections, the Ku-band radar detection performance is summarized. In Figures 4 and 5, the target detection design margins are plotted versus range for both

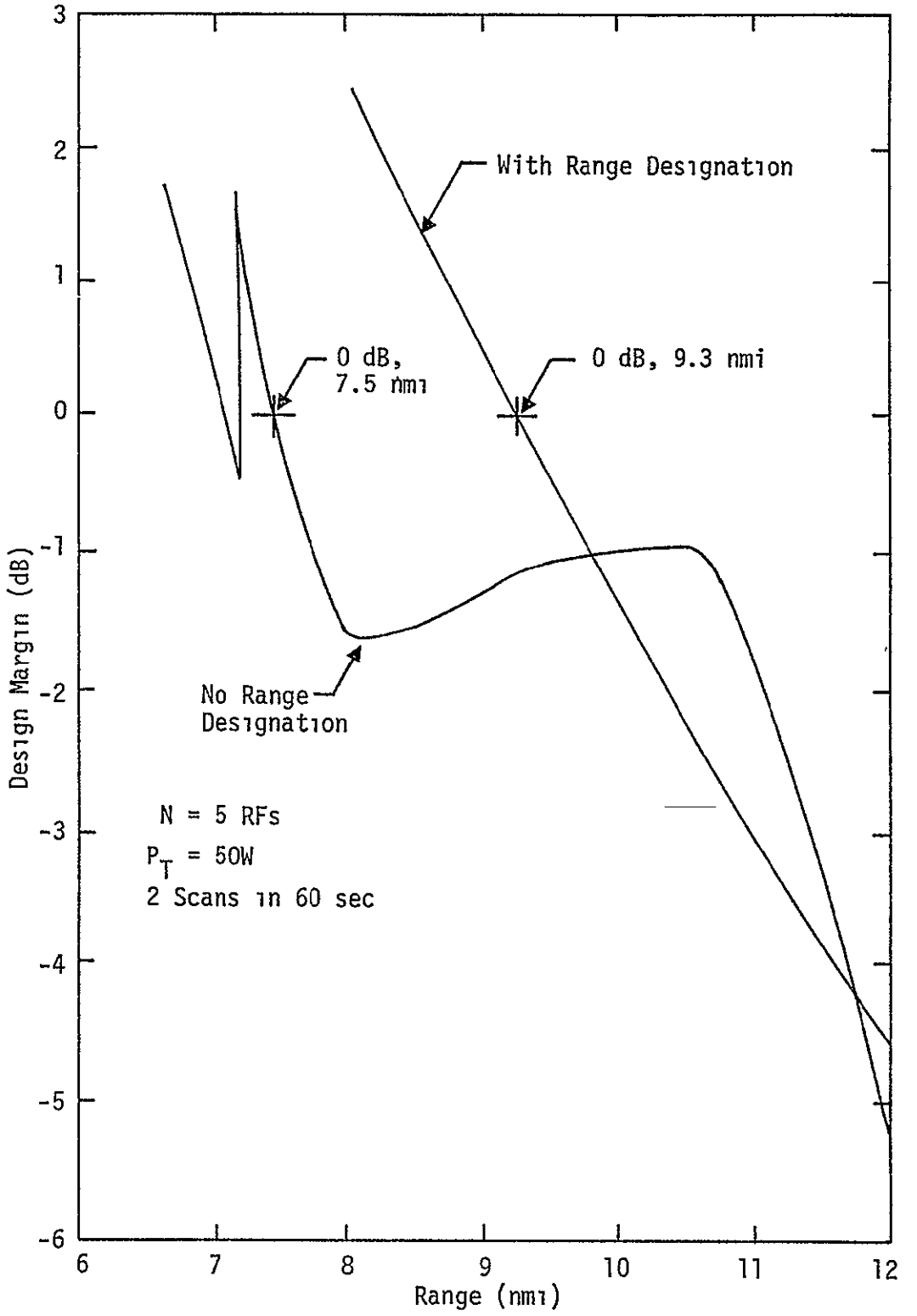


Figure 4. Target Detection Design Margin Versus Range for Worst Case Losses in Table 1

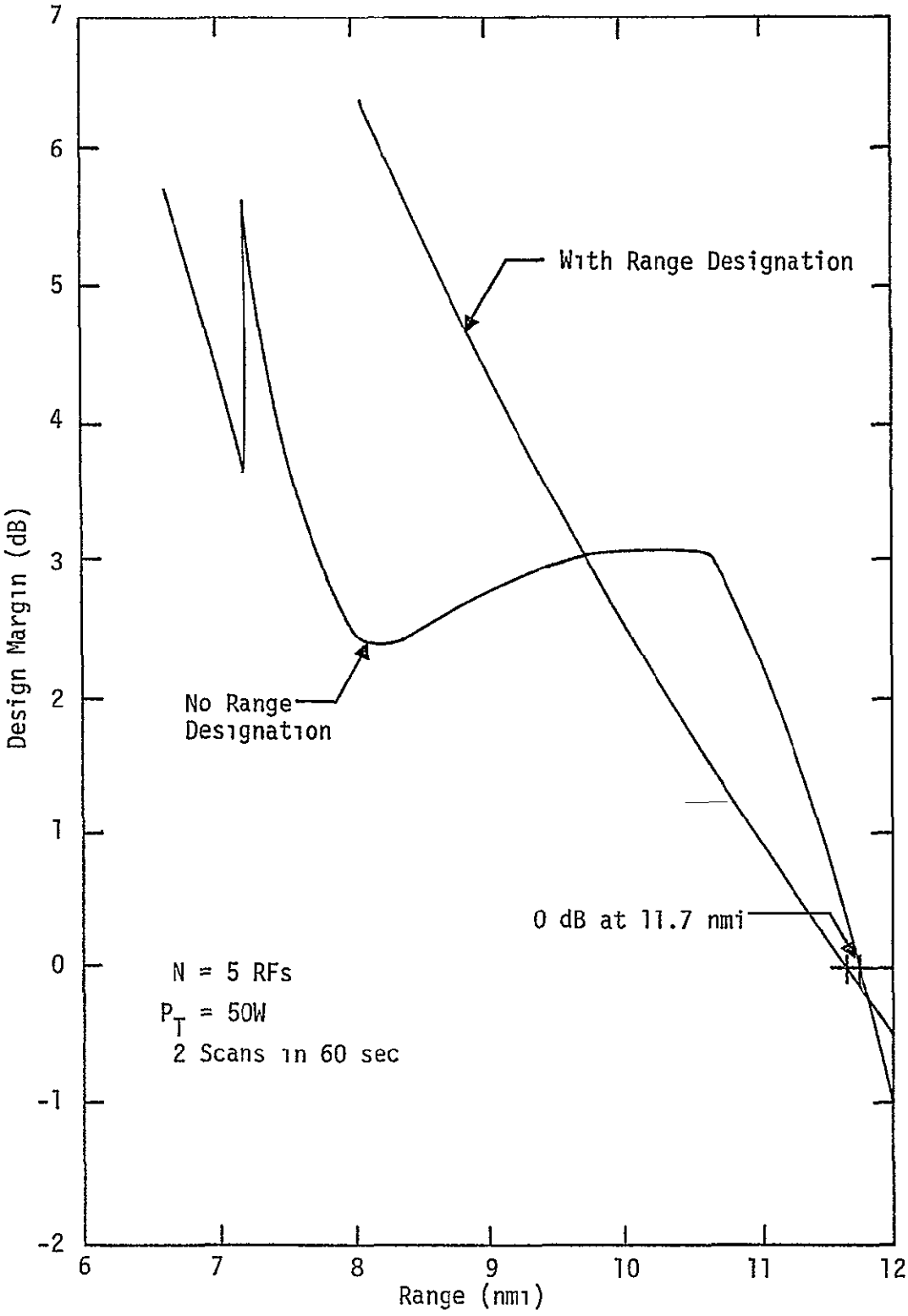


Figure 5. Target Detection Design Margins Versus Range for Average Losses in Table 1

the designated range and nondesignated range modes of operation. Except for the losses, all radar equation parameters are the same as used in [1, Appendix A]. In Figure 4, the worst case losses of Table 1 are used. Also, a transmitted power of 50 watts is used, although the present system configuration consists of a 60-watt TWT. This is approximately a 0.8 dB improvement. For the range designation mode, a design margin of 0 dB is obtained at approximately 9.3 nmi. For the nondesignated range mode, it is about 7.5 nmi. The design margin for the nondesignated range mode deteriorates as the range is reduced in the interval of 8 to 11 nmi because in this interval, the range gate straddling loss is increasing faster than the factor $R^{-4}$ in the radar equation. At 12 nmi, the design margin is -4.5 dB for the range designated mode and -5.1 dB for the nondesignated range mode.

In Figure 5, the design margin is shown versus range for the average losses in Table 1. In this case, a 0 dB design margin is obtained at approximately 11.7 nmi; at 12 nmi, the design margin is greater than -1 dB.

The cumulative detection probability is plotted versus range for the worst case and average losses in Figures 6 and 7, respectively. Both M = 1 and M = 2 scans are shown. It is seen that the two-scan case uniformly outperforms the single scan case for both the designated and nondesignated range modes. In these computations, a transmitted power of 60 watts was used.

Inspection of Figures 6 and 7 reveals that, depending on the range, the cumulative detection probability for the designated range can be both smaller and larger than that for the nondesignated case. This is also the case for the design margins in Figures 4 and 5. At 12 nmi, the cumulative detection probability is approximately 75% for two scans and approximately 50% for one scan This is the case for both the designated and nondesignated range modes.

In order to determine what can be gained by allowing more total time to detect the target, the cumulative probability of detection was determined for various scan times and at various ranges. In Figure 8, the cumulative probability of detection versus total scan time is shown for various ranges. In these computations, two scans were assumed so that the scan rate varies with the total scan time. By allowing a slower

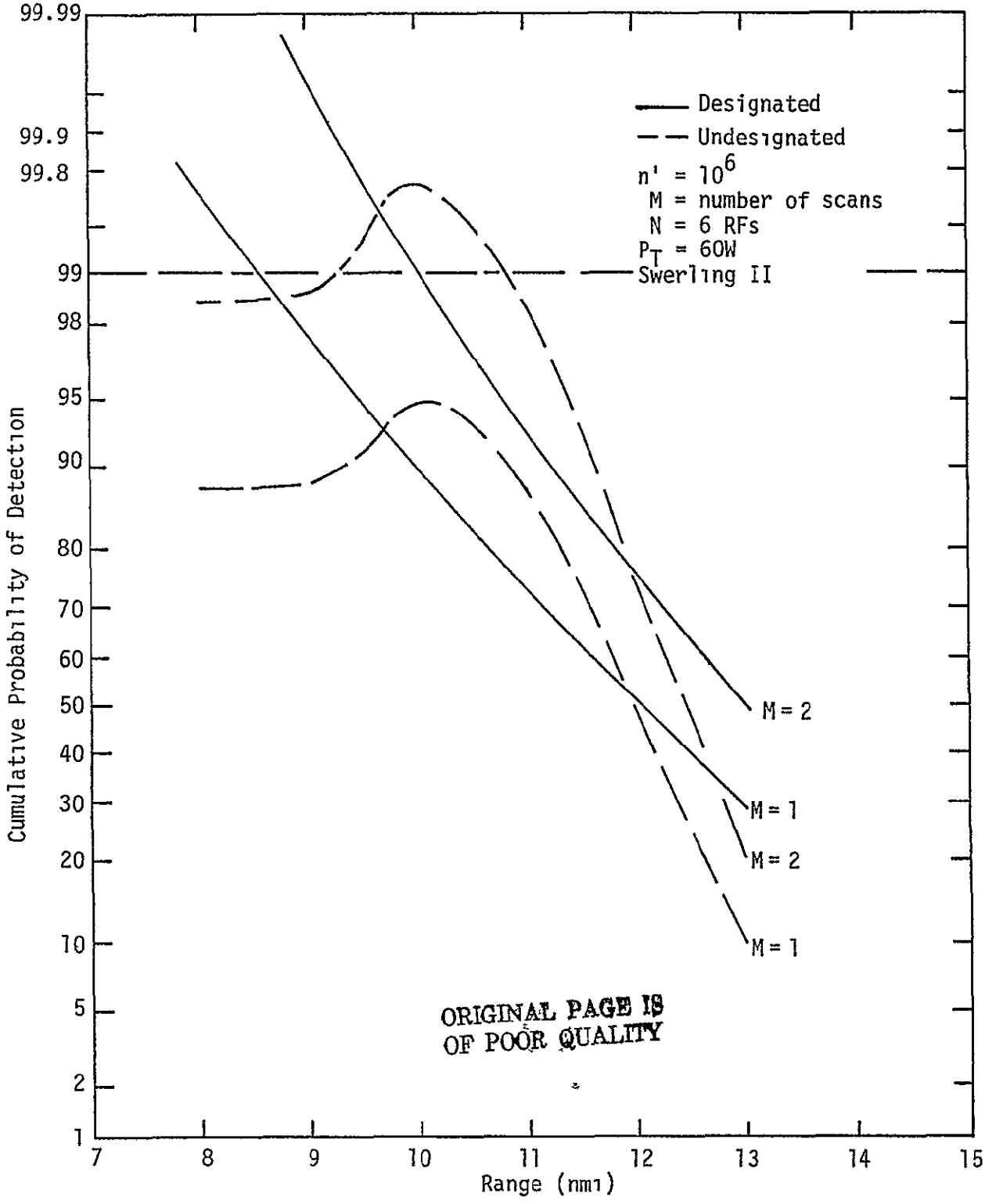


Figure 6. Cumulative Detection Probability Versus Range for Worst Case Losses in Table 1

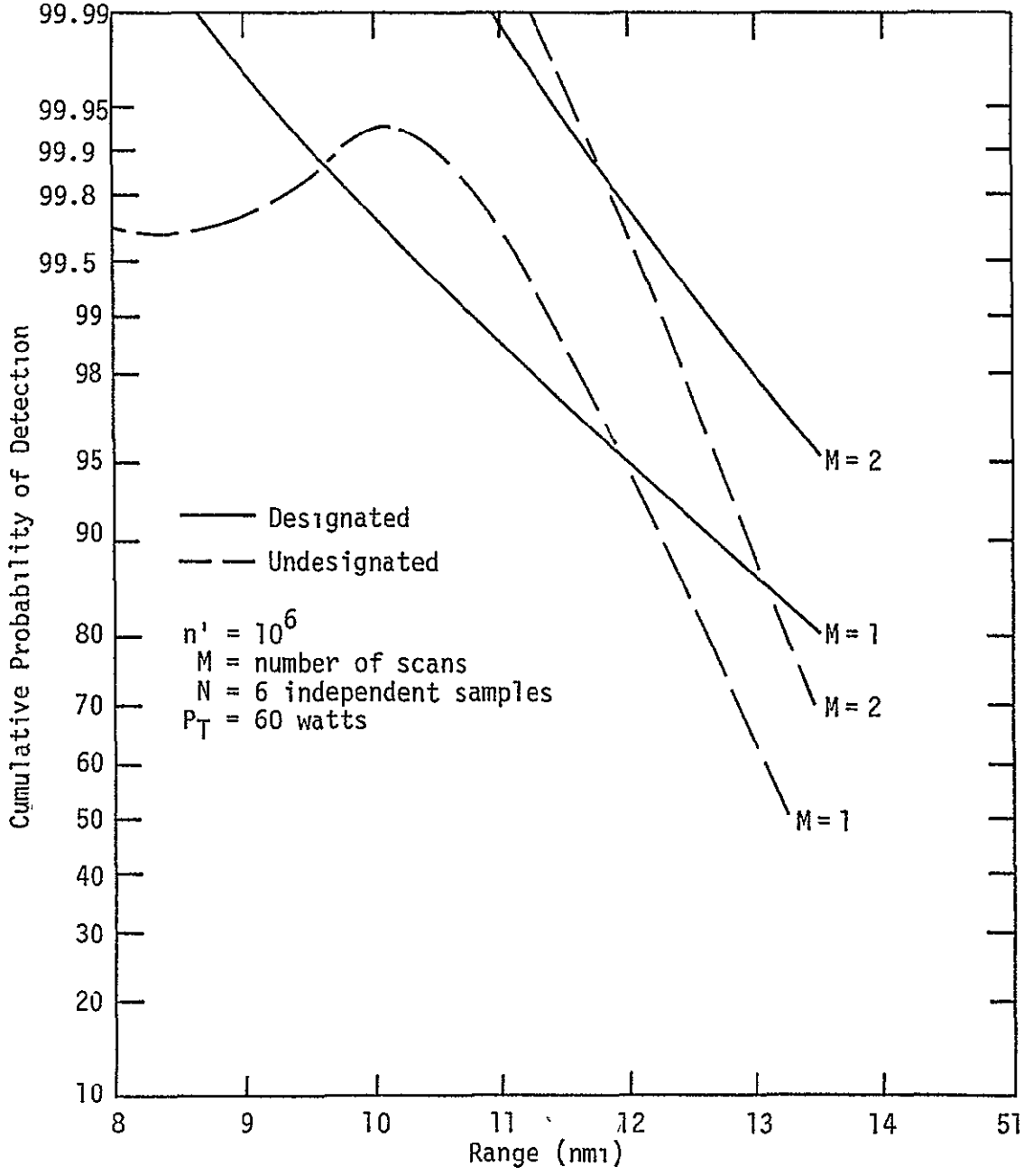


Figure 7. Cumulative Probability of Detection Versus Range for Average Losses in Table 1

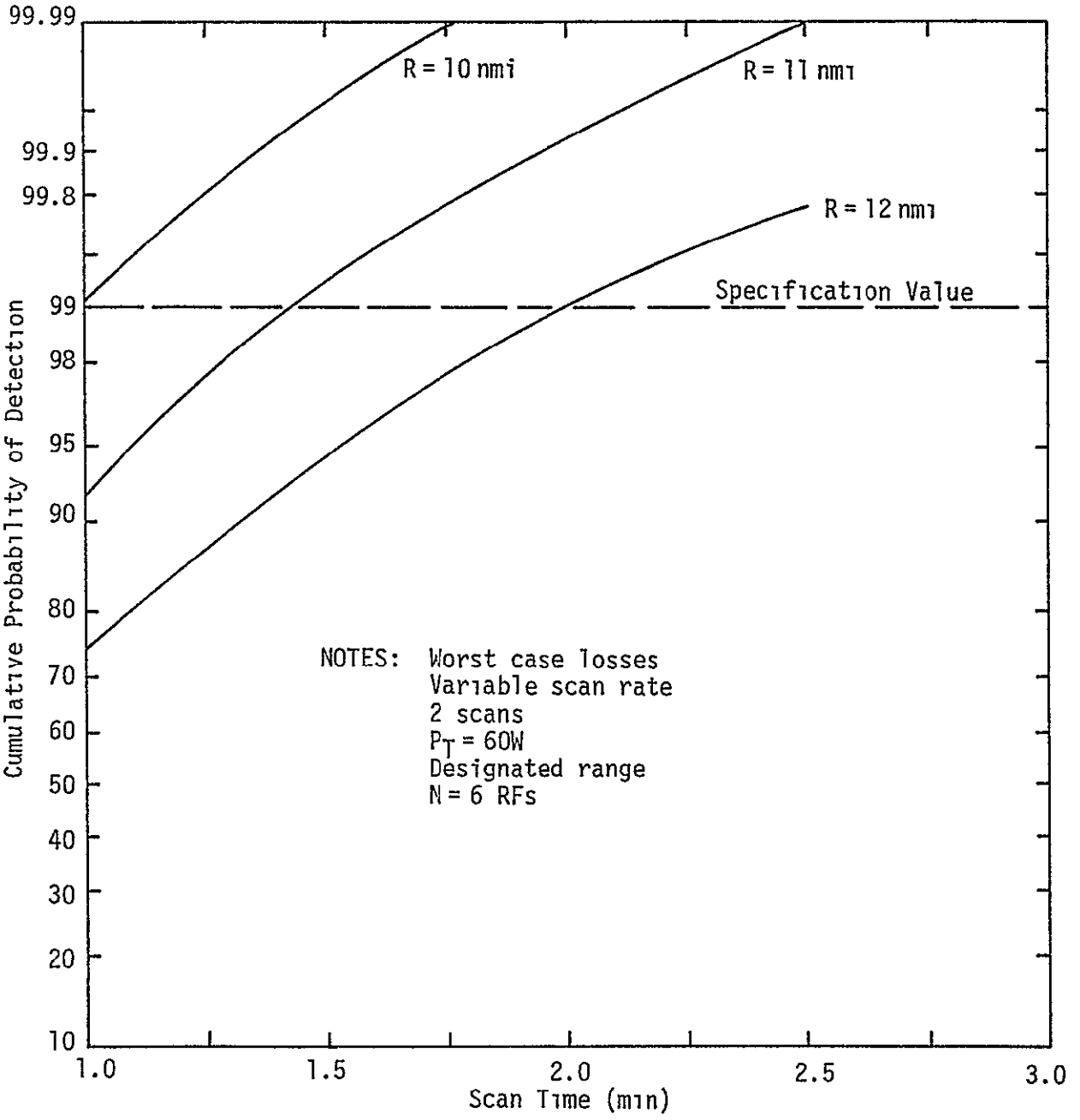


Figure 8. Cumulative Probability of Detection Versus Scan Time for Various Ranges

scan rate, it is seen in Figure 8 that there is dramatic improvement in the cumulative probability of detection. In particular, if the total scan time is increased to 2 minutes, then the cumulative detection probability at 12 nmi is 99% (the specification value). This is for the worst case losses and a designated range mode.

Unfortunately, increasing the coherent detection time in this manner by lowering the scan rate has major hardware implications. It does provide the best improvement in performance, however.

The scan rate is held fixed at two scans per minute in Figure 9, where the cumulative detection probability is plotted versus range. In this case, the improvement in performance is not as dramatic as when the scan rate is reduced. The gain is significant, however. At 11.3 nmi, for example, by increasing the total scan time from 1 minute to 2 minutes, the cumulative detection probability increases from 90% to 99%.

## 2.4 Alternatives and Recommendations

If the design philosophy of average losses is acceptable, then the design margin at 12 nmi is within a few tenths of 0 dB with a 50-watt TWT and approximately 0 dB with a 60-watt TWT.

If the design philosophy of worst case losses is preferred, the design margin is between -4 dB and -5.2 dB. In this section, various alternatives are listed, along with recommendations.

(a) Use a Slower Scan Rate. As described in the previous section, this provides the maximum improvement in performance for a given amount of increased time Since this alternative has major hardware implications, it is not recommended.

(b) Increase Post-Detection Integration (PDI). This can be accomplished by increasing the total number of RF frequencies used in frequency diversity This also has moderate hardware implications and is therefore also not recommended.

(c) Increase the Number of Scans at the Same Scan Rate As shown above, there is significant improvement in performance by maintaining the same scan rate and allowing the total search time to increase from 1 minute to 2 minutes. This increases the total number of scans from 2 to 4. This keeps the present radar configuration entirely intact and thereby has virtually no hardware implications. For worst case losses,

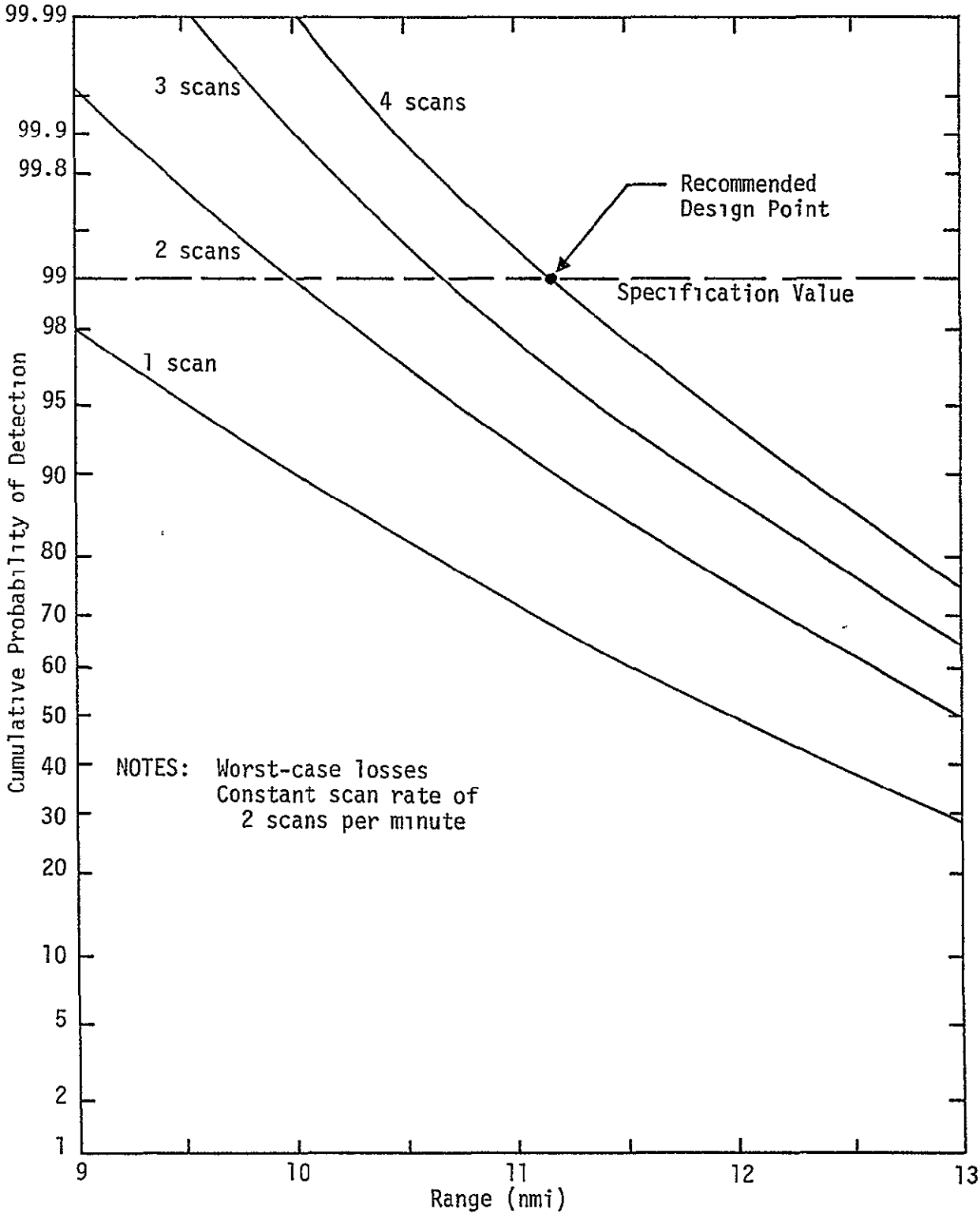


Figure 9. Cumulative Detection Probability Versus Range for Various Scans

a 0 dB design margin is obtained at a range of 11.3 nmi. We recommend this alternative, and this recommended design point is shown in Figure 9.

(d) A final alternative which applies to the range designate mode only is to narrow somewhat the two range gates during search. How much they can be narrowed is a function of the anticipated range designate accuracy. We do not have a recommendation on this alternative. It could be implemented in addition to the recommended third alternative above. If one has any doubt about the range designate accuracy, however, then this alternative does not appear satisfactory.

## 3.0 POINT TARGET TRACKING

The tracking performance of a point target of the Ku-band radar is presented. The performance is described twofold. First, the effects of thermal noise and target amplitude scintillation are given in section 3.1. In section 3.2, the tracking capability is given in the presence of relative accelerations along and perpendicular to the LOS. Emphasis is placed on the recovery time after an acceleration.

### 3.1 Thermal Noise and Target Scintillation Effects on Tracking Accuracies for Passive Point Targets

The purpose of this section is to present the numerical results associated with the analysis carried out in [1] for the Ku-band radar tracking accuracies due to thermal noise and target scintillation effects for a passive point target. The target effects which become a major concern at short ranges will be discussed in a subsequent section. No attempt will be made at this point to perform any additional analysis of the tracking loops.

The tracking accuracies of the four variables being tracked (range, range rate, angle and angle rate) are presented as functions of range and compared to the existing specifications [2]. It is to be noted that there are two factors affecting the results:

(1) Thermal noise and target scintillation which become the dominating factor at long ranges

(2) Quantization effects in the Ku-band radar [1] which uses 4 bits of quantization, resulting in a signal-to-noise ratio at the output of the A/D converter equal to

$$(SNR)_{out} = \left[\frac{1}{1 + (1 + (SNR)_{in})(0.0129)}\right] (SNR)_{in} , \qquad (6)$$

where $(SNR)_{in}$ is the signal-to-noise ratio at the input of the A/D converter. The signal at the output of the A/D converter is presumed with a resulting gain in signal-to-noise ratio equal to 16 (12.04 dB). Thus, the resulting SNR used in the calculations is

$$(SNR)_{dB} = ((SNR)_{out})_{dB} + 12.04 \text{ dB} . \qquad (7)$$

It is easy to see from (6) that, at high input signal-to-noise ratio (close range), the resulting SNR saturates at

$$\text{SNR} = 18.9 + 12.04 = 30.94 \text{ dB},$$

which makes the quantization effect the major contributing factor to the tracking accuracies. The combined effect of both factors is taken into account in all subsequent calculations.

There are many parameters in the various tracking loops that are varied with the designated range. The parameters used in these calculations are the latest available from Hughes Aircraft Company and are summarized in Table 3.

### 3.1.1 Angle and Angle Rate Tracking Accuracies

The angle and angle rate tracking accuracies are presented together because the angle rate estimation is carried out in the angle tracking loop. The ratio of angle rate root-mean-squared (RMS) error $\sigma_{\dot{\theta}}$ to the angle RMS error $\sigma_\theta$ is given as [1]:

$$\frac{\sigma_{\dot{\theta}}}{\sigma_\theta} = \sqrt{\frac{K}{K\tau^2 + 1}} \quad \text{sec}^{-1}, \tag{8}$$

where K is the equivalent angle loop gain and $\tau$ is its time constant. The variations of K and $\tau$ with range are shown in Table 3. The angle RMS error is given by

$$\sigma_\theta = \sqrt{\frac{(K\tau^2 + 1)\, T_s}{4\tau}} \; \frac{\theta_B}{4 \rho_\theta K_m} \; \sigma_{x\theta}(N, \text{SNR}), \tag{9}$$

where $T_s$ = time per sample of the equivalent discrete time noise (x) whose variance is $\sigma_{x\theta}$

$\theta_B$ = 1.6° = 3 dB bandwidth of the Ku-band antenna

$K_m$ = 1

N = number of independent samples used to obtain $\sigma_{x\theta}$ (N = 10 for angle tracking)

$\rho_\theta$ and $\sigma_{x\theta}$ are functions of SNR and are discussed in detail in [1] and in the simulation section of this report.

Figures 10 and 11 illustrate the variations of $3\sigma_\theta$ and $3\sigma_{\dot{\theta}}$ with range. It is obvious that both the angle and the angle rate accuracies

Table 3. Summary of Tracking Loop Parameters (Passive Target)

| Parameter | Range (nmi) | | | | | | Remarks |
|---|---|---|---|---|---|---|---|
| | > 9.5 | 9.5-3.8 | 3.8-1 9 | 1.9-0.95 | 0.95-0.42 | 0.42 | |
| $d_t$ | 0.099 | 0.116 | 0 058 | 0.029 | 0.0144 | 0.00085 | Duty factor |
| $\tau_E$ (msec) | 5.36 | 2.29 | 2.29 | 2.92 | 2.29 | 2.29 | $1/B_F$ |
| $\Delta$ (μsec) | 33.2 | 16.6 | 8.3 | 4.15 | 2.07 | 0.122 | Pulse width |
| $\alpha$ | 0.0566 | 0.1132 | 0.2263 | 0.2263 | 0.4526 | 0.4803 | |
| $\beta$ | 0.000884 | 0.00354 | 0.0283 | 0.0283 | 0.1132 | 0.1202 | |
| $B_F$ (Hz) | 186 | 437 | 437 | 437 | 437 | 437 | Doppler filter bandwidth |
| m | 2 | 4 | 4 | 4 | 4 | 4 | Number of averaged samples |
| $T_s$ (msec) | 107.2 | 45.9 | 45.9 | 45.9 | 45.9 | 45.9 | |
| $L_{\theta,\dot{\theta}}$ | 16.90 | 16.83 | 16.83 | 16.83 | 16.83 | 16.83 | Angle and angle rate losses |
| $L_{R,\dot{R}}$ | 9.49 | 9 42 | 9.42 | 9.42 | 9.42 | 9.42 | Range and range rate losses |
| K | 0.0288 | 0.0288 | 0.2221 | 0.5685 | 0.5685 | 0.5685 | Angle loop gain |
| $\tau$ (sec) | 12 | 12 | 4.25 | 2.7 | 2.7 | 2.7 | Angle loop time constant |
| PRF (Hz) | 2987 | 6970 | 6970 | 6970 | 6970 | 6970 | |

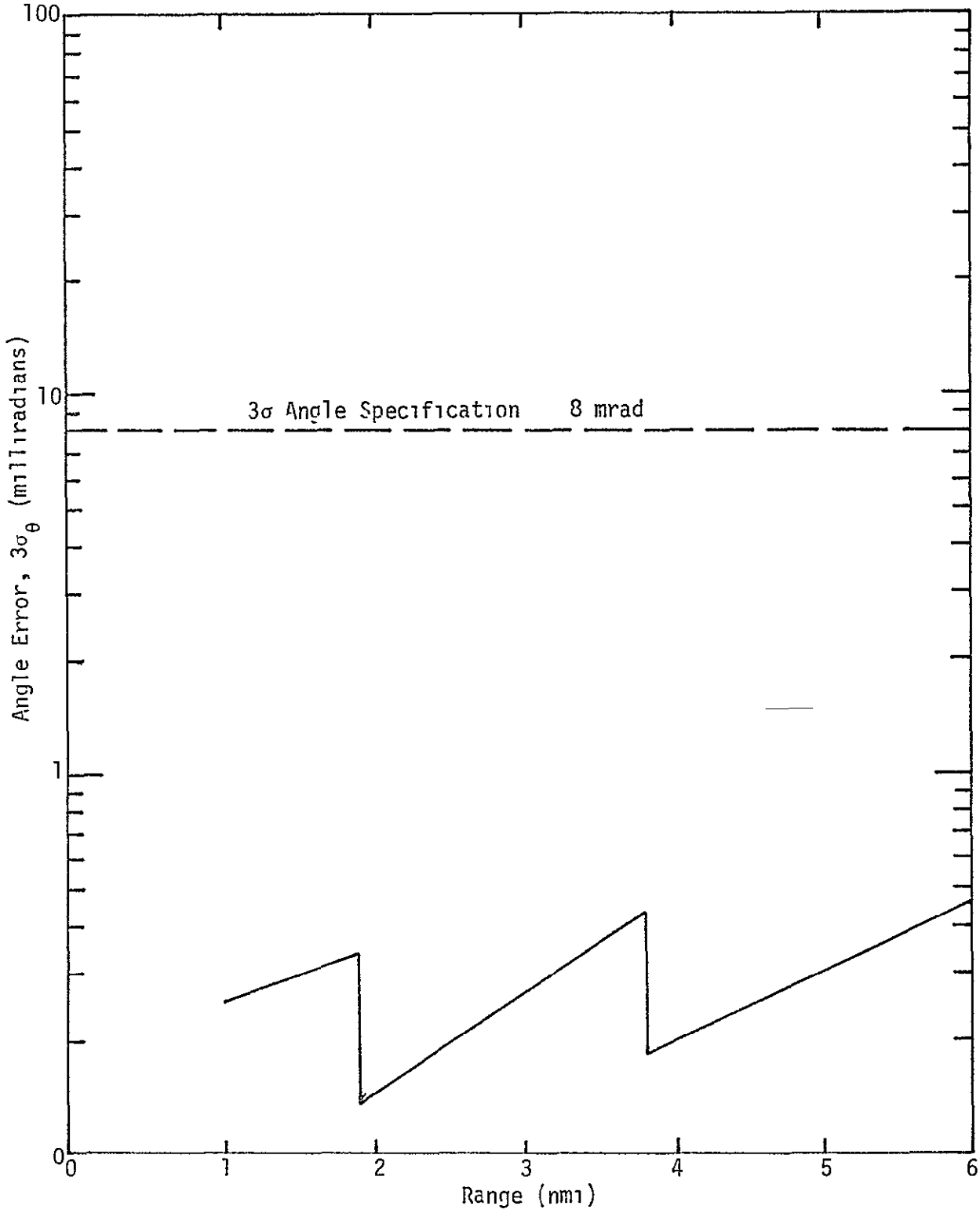


Figure 10. Angle Tracking Error of Passive Point Target Due to Thermal Noise and Target Scintillation Versus Range

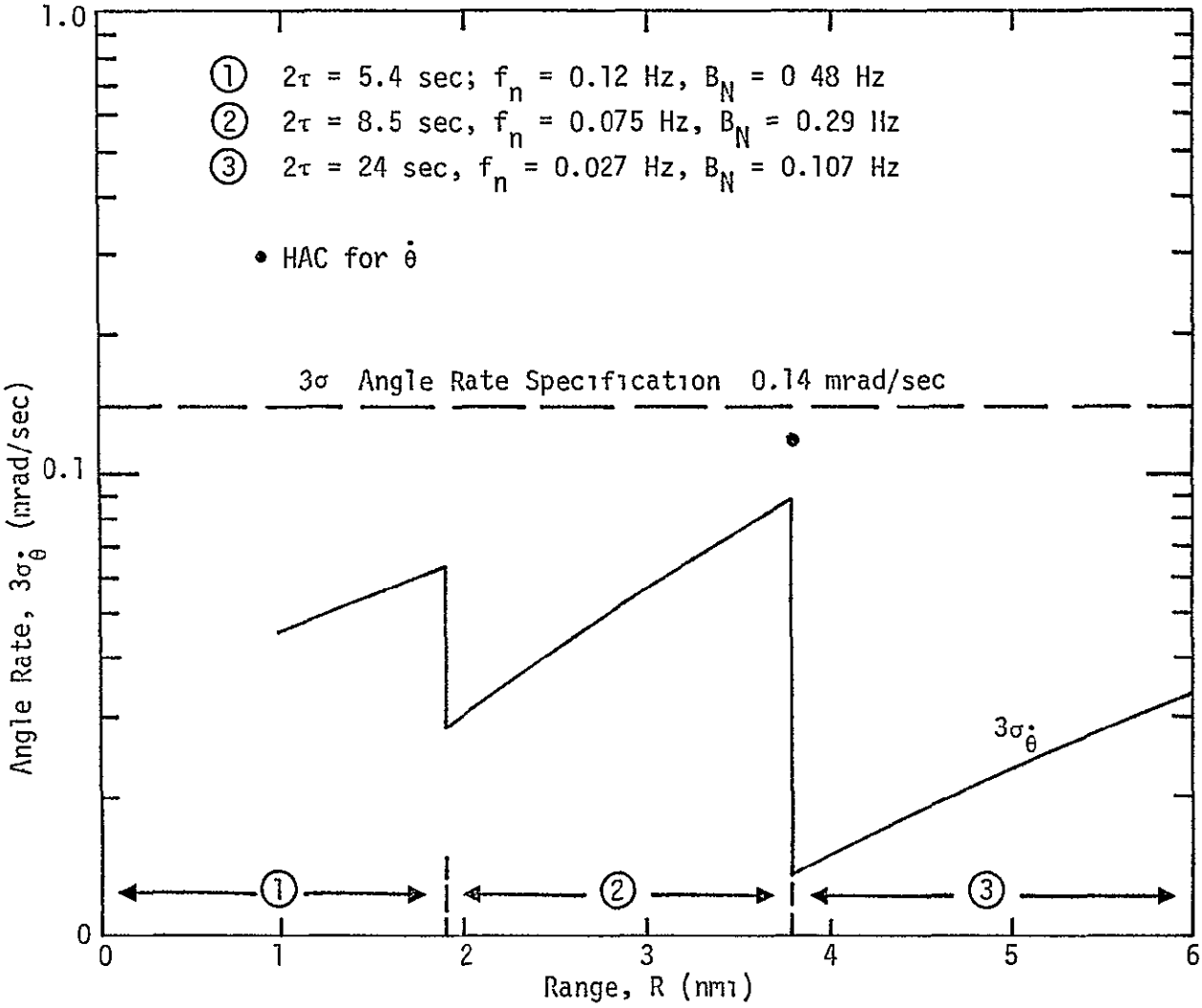


Figure 11. Angle Rate Estimation of a Passive Point Target Due to Thermal Noise and Target Scintillation Versus Range

meet the design specifications. The design margin in the angle rate tracking, however, is much less than that for the angle. This is due to the fact that the loop filter in the former has been widened to provide faster recovery from acceleration transients. It is believed that increasing the gain K slightly would improve the transient performance of the loop while maintaining the random error within or very close to the specifications.

3.1.2 Range Tracking Accuracies

The RMS of the range error $\sigma_R$ (timing error) is computed using the results of [2], namely,

$$\sigma_R = \frac{\Delta c}{4}\left(1 + \frac{4}{SNR}\right)^{1/2} (B_N T_s)^{1/2} \sigma_{xR}(N,SNR), \tag{10}$$

where $\Delta$ = pulse width of the transmitted signal (see Table 3)

$c$ = velocity of light in free space

$B_N$ = bandwidth of the range tracking loop which includes the $\alpha$-$\beta$ tracker as a loop filter

$$B_N = \frac{8(1 + 4/SNR)^{1/2}\alpha^2 + \beta}{4\alpha T_s} \tag{11}$$

$\sigma_{xR}$ = RMS of the equivalent noise of the system due to thermal noise

$N$ = number of independent samples used to obtain $\sigma_{xR}$ ($N = 20$ for range tracking.

Figure 12 illustrates the variation of the RMS range error versus range with the noise bandwidth as a parameter. The jump at 9.5 nmi is due mainly to the change in PRF at that range. It is observed that, since the values of $\alpha$ and $\beta$ used at longer ranges correspond to $B_N \simeq 1$ Hz, the range RMS error due to thermal noise meets the specifications up to 9.5 nmi. The specifications are illustrated in Figure 13 for convenience

Figure 14 illustrates the variations of the range error at closer ranges ($R < 6$ nmi) with the latest values of $\alpha$ and $\beta$ as parameters. The figure also shows the latest performance curve presented by Hughes for comparison purposes. There are four points to observe.

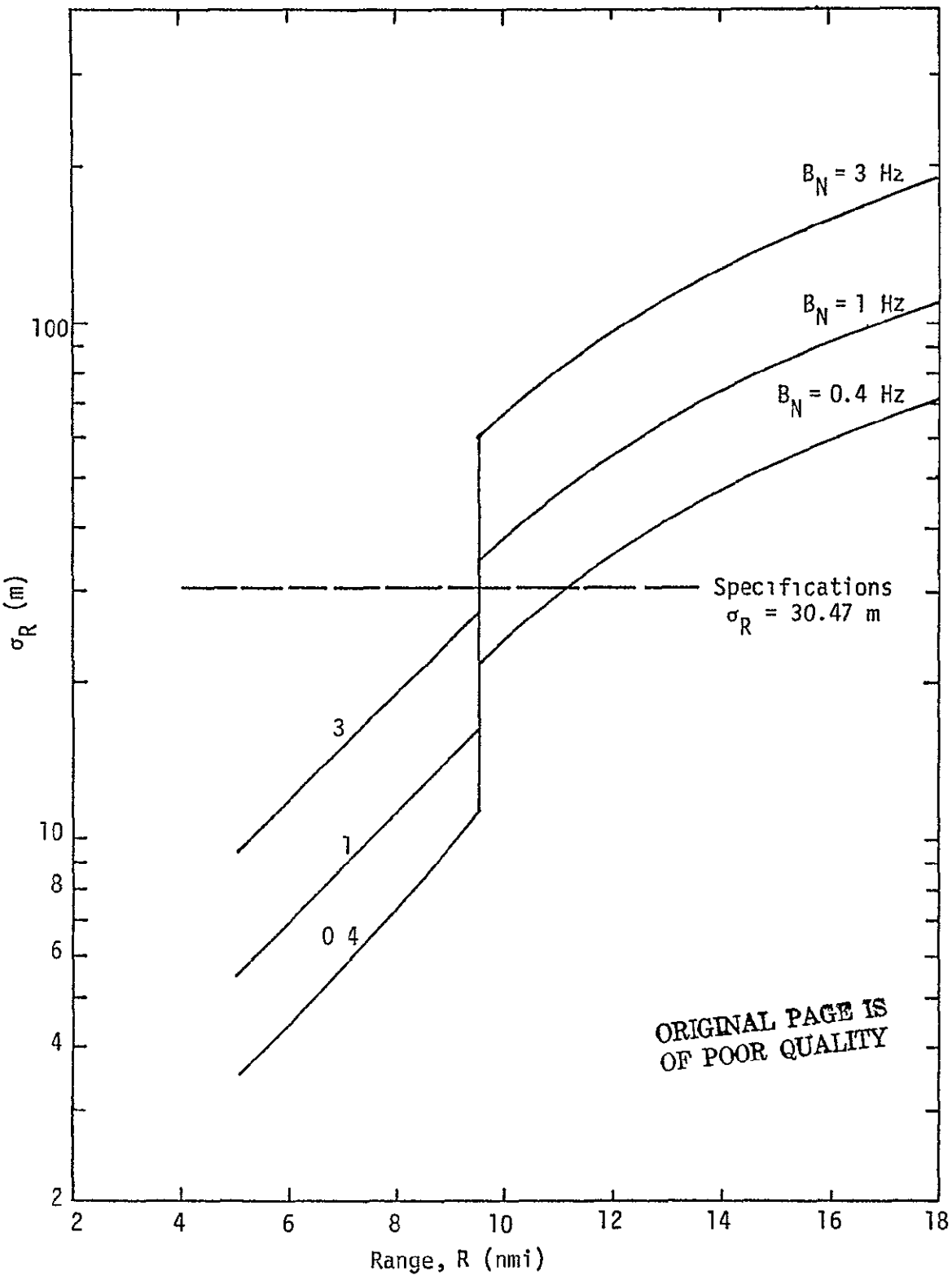


Figure 12 RMS Range Tracking Error of Point Passive Targets Versus Range

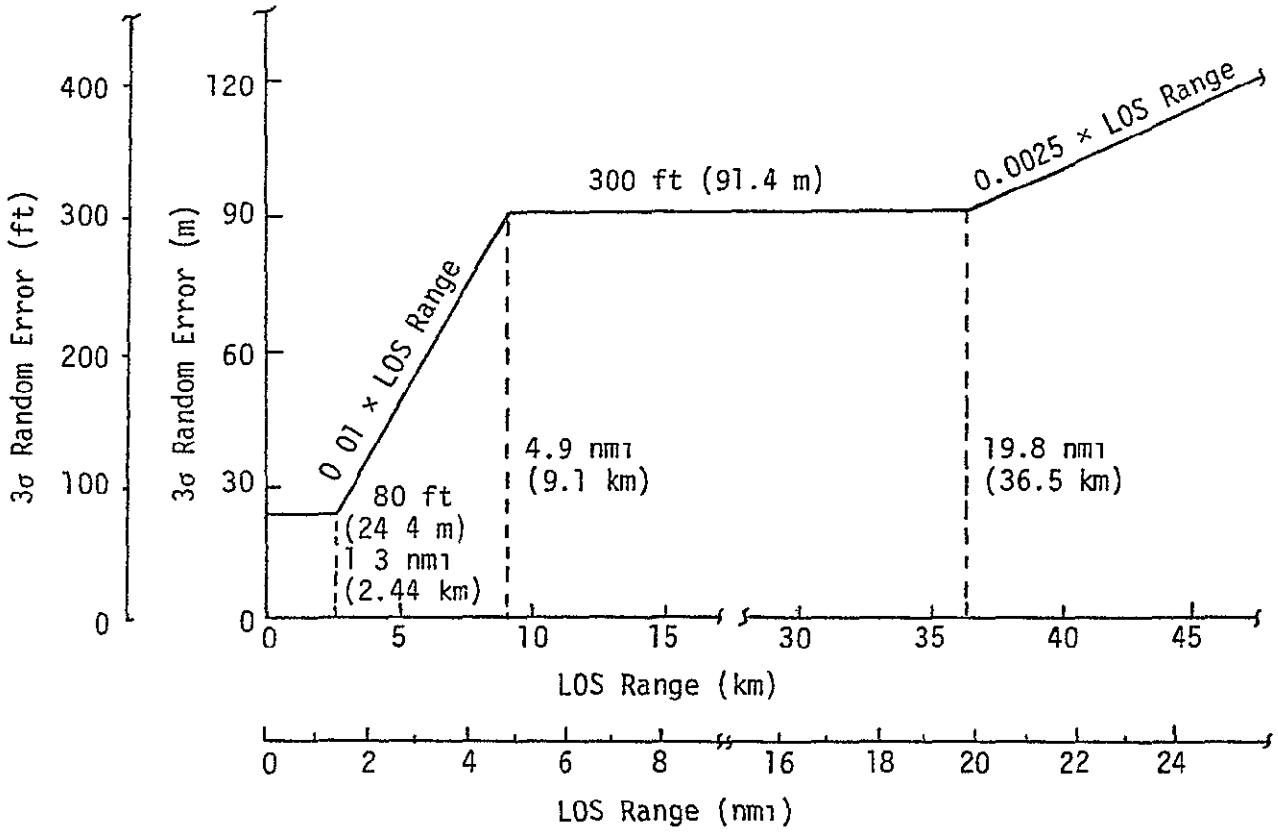


Figure 13. Specification for Three-Sigma Random Range Error Versus LOS Range

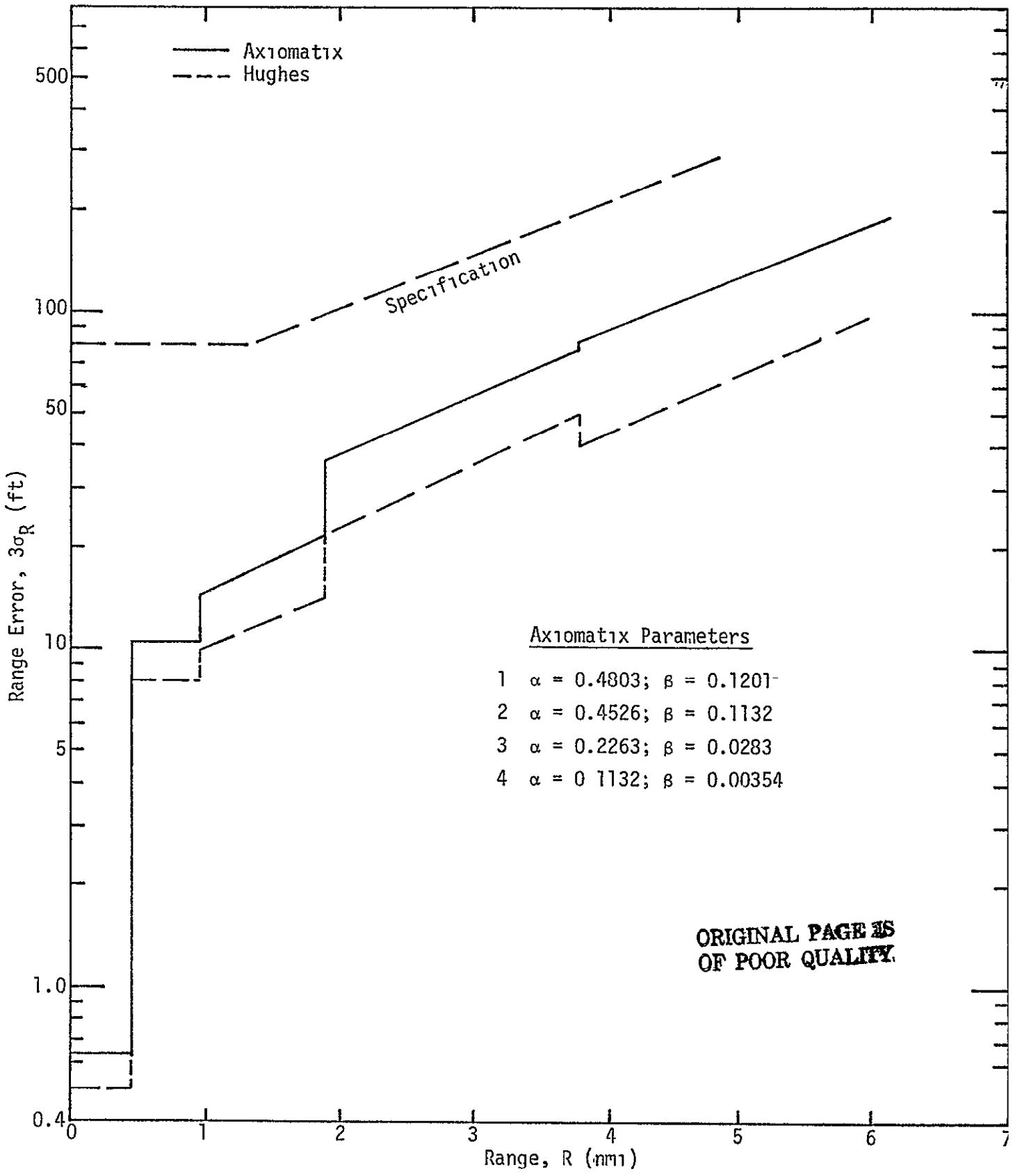


Figure 14. RMS Range Tracking Error of Passive Point Targets at Close Range Versus Range

(1) The range tracking performance of a passive point target due to thermal noise and target scintillation is well below the specifications, especially at close range.

(2) The flat portions of the curve at ranges R < 1 nmi are due to quantization limiting effect.

(3) The difference between the Axiomatix and Hughes performance curves is believed to be due to the automatic gain control (AGC) which has not been taken into account in the analysis.

(4) Although the accuracies at close range drop below 10 feet, it is believed that 10 feet is the best achievable accuracy because of the sensitivity of the meters.

3.1.3 Range Rate Tracking Accuracy

The range rate RMS error due to thermal noise and target scintillation has been found in [2] to be

$$\sigma_{\dot{R}} = \left(\frac{c\,B_F}{16\,f_c}\right)\left(1+\frac{\pi^2}{SNR}\right)^{1/2}\left(\frac{1}{m}\right)^{1/2}\sigma_{x\dot{R}}(N,SNR)\,, \qquad (12)$$

where $B_F$ = doppler filter single-sided noise bandwidth

$f_c$ = RF carrier frequency. The middle RF frequency $f_c = 13.885$ GHz in the frequency diversity system is used in the computations.

m = number of samples being averaged to give a single $\dot{R}$ reading. m = 2 for R > 9.5 nmi and m = 4 for R < 9.5 nmi.

$\sigma_{x\dot{R}}$ = RMS of the equivalent noise of the system due to thermal noise.

N = number of independent samples used to obtain $\sigma_{x\dot{R}}$ (N = 40 for range rate tracking).

The evaluation of $\sigma_{\dot{R}}$ for various ranges is shown in Figures 15 and 16. Figure 15 illustrates the range rate errors at long ranges and shows the effect of varying the number of averaged samples (m) at 9.5 nmi. As is obvious from the figure, the range rate accuracies meet the specifications for all ranges below the specified 10 nmi. The same thing is true for Figure 16, which illustrates the variations of $\sigma_{\dot{R}}$ at short ranges.

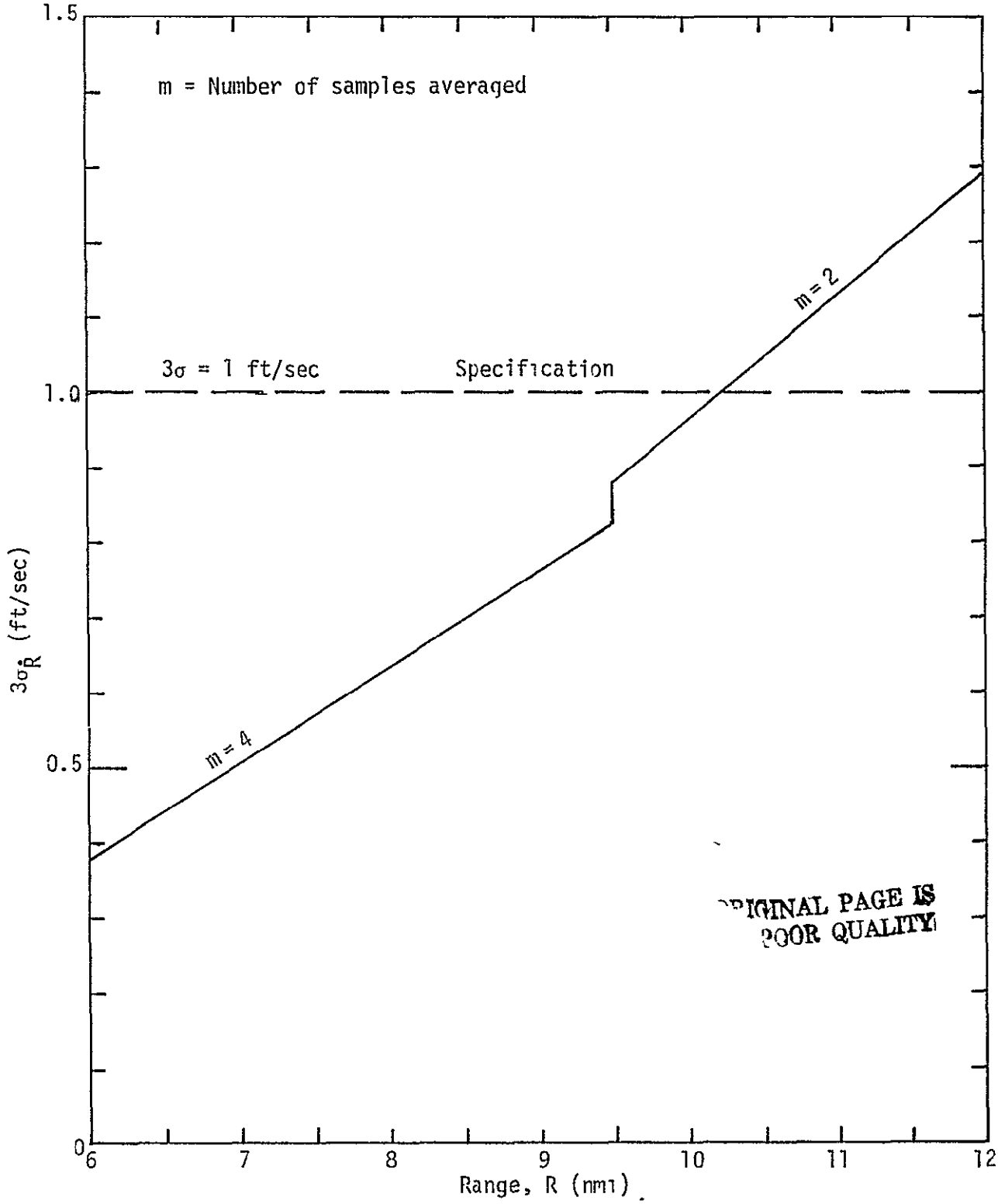




Figure 15. RMS Range Rate Tracking Error Due to Thermal Noise and Target Scintillation of Passive Point Targets Versus Range (Long Ranges)

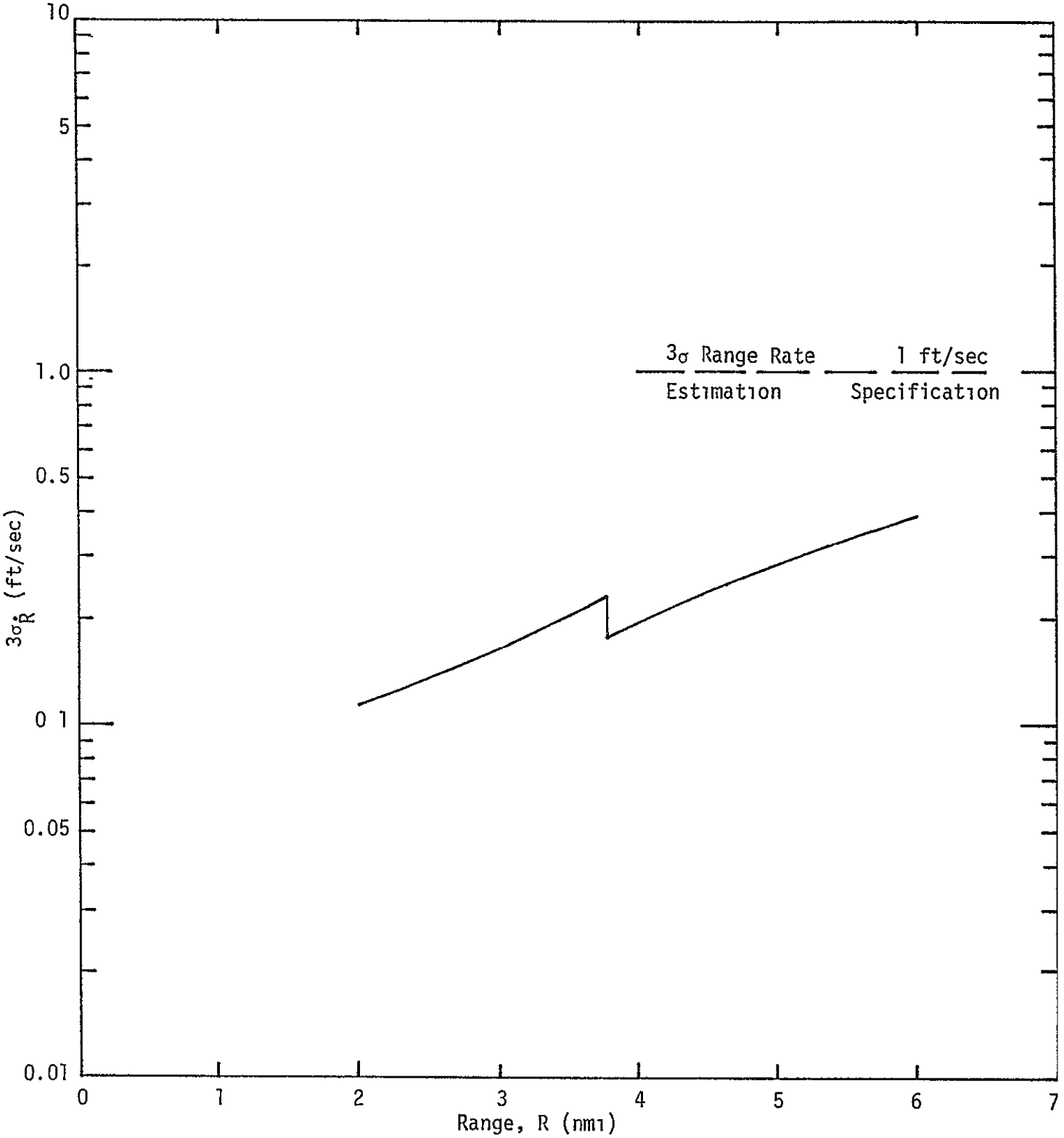


Figure 16. RMS Range Rate Tracking Error Due to Thermal Noise and Target Scintillation of Passive Point Targets Versus Range (Short Ranges)

In order to avoid confusion, it should be pointed out that the numerical evaluations of the range rate accuracies in [1] were erroneous and the numbers presented in Figures 15 and 16 represent the correct calculations.

## 3.2 Effects of Point Target Accelerations

### 3.2.1 Introduction

This section investigates the performance of the Ku-band radar system in the tracking mode when a constant acceleration takes place. Two extreme cases can be distinguished. The first will be referred to as radial acceleration, which is achieved by firing retro rockets in the direction of the line-of-sight (LOS). This causes the range to vary as a quadratic function of time rather than a linear function of time, which occurs in the case of a constant approaching velocity (range rate). The second case will be referred to as tangential acceleration, which is an acceleration in a direction perpendicular to the LOS, causing a quadratic variation in the target angle being tracked. Since both the azimuth and the elevation angles are tracked similarly [1], this section will not distinguish between the two angles. The radial and tangential acceleration cases are illustrated in Figure 17.

The analysis of the tracking loops in the presence of acceleration is performed in this section for a deterministic input. This is a realistic assumption for the range of interest, namely, close range when the signal-to-noise ratio is high. It is believed that the transient behavior of the tracking loops with noisy inputs can only be determined via simulation of these loops, which is discussed in Section 4.0 of this report.

### 3.2.2 Radial Accelerations

A constant radial acceleration, as shown in Figure 17, causes the range to change as a quadratic function of time without affecting the angle measurements. The range tracking loop is discussed in [1] and is shown in Figure 18 for the deterministic case of interest (SNR$\to\infty$ implies $\rho = 1$ and no noise). The parameters in the figure are:

T = actual time delay between transmission and reception of a given pulse. For a passive target at range R, $T = 2R/c$, where c is the velocity of light in free space.

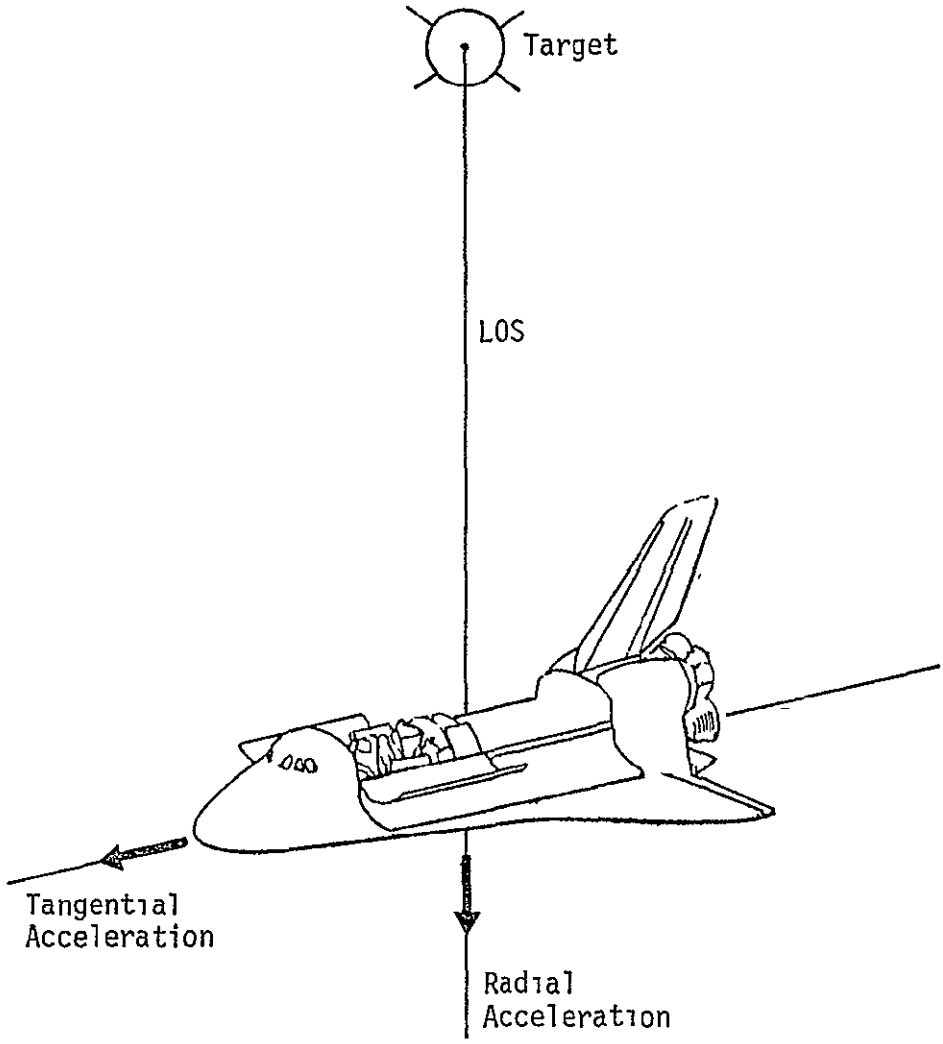


Figure 17. Radial and Tangential Accelerations

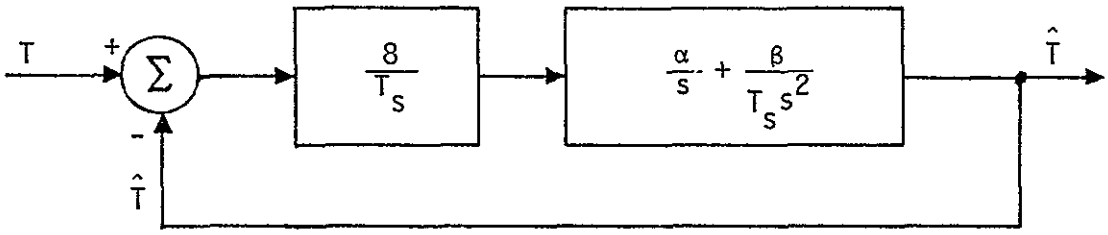


Figure 18. Deterministic Range Tracking Loop

$\hat{T}$ = loop estimate of the actual delay T.

$\Delta_T = T - \hat{T}$ = the timing error.

$T_s$ = computation time per sample = 107.2 msec when R > 9.5 nmi
= 45 9 msec when R < 9.5 nmi.

$\alpha, \beta$ = $\alpha$-$\beta$ tracker parameters which vary with the designated range as shown in Table 4.

Table 4. $\alpha$-$\beta$ Tracker Parameters

| | Range (nmi) | | | | |
|---|---|---|---|---|---|
| | <0.42 | <0.95 | <3 8 | <9.5 | <13.2 |
| $\alpha$ | 0.4809 | 0.4526 | 0.2263 | 0.1132 | 0.0566 |
| $\beta$ | 0.1202 | 0.1132 | 0.0283 | 0.00354 | 0.000884 |

Simple derivation results in

$$\Delta T(s) = \frac{s^2}{s^2 + 8\left(\frac{\alpha}{T_s}\right)s + \left(\frac{8\beta}{T_s^2}\right)} T(s) ,$$



which, when converted to range measurements, yields

$$\Delta R(s) = \frac{s^2}{s^2 + \alpha' s + \frac{\beta'}{T_s}} R(s) , \qquad (13)$$

where $R(s)$ = Laplace transform of the actual range $R(t)$

$\Delta R(s)$ = Laplace transform of the range error $\Delta R(t)$

$\alpha'$ and $\beta'$ are defined as $\alpha' \triangleq \frac{8\alpha}{T_s}$ and $\beta' \triangleq \frac{8\beta}{T_s}$.

Since the actual acceleration (A) is a rocket burn for a period of time T, it can be represented as

$$a(t) = A[u(t) - u(t-T)], \tag{14}$$

where $u(t)$ is the unit step function. Taking the Laplace transform of (14) and using the fact that the acceleration is the second derivative of range, the range transform can be written as [3]:

$$R(s) = \frac{A}{s^3}(1 - e^{-sT}) \tag{15}$$

which, when substituted in (14), results in:

$$\Delta R(s) = \frac{A(1 - e^{-sT})}{s\left[s^2 + \alpha' s + \frac{\beta'}{T_s}\right]}. \tag{16}$$

The denominator has a positive discriminant for all the values of $\alpha$ and $\beta$ listed in Table 4 and hence can be factored as $s(s+a_1)(s+a_2)$, where

$$a_1 = \frac{4}{T_s}\left(\alpha - \sqrt{\alpha^2 - \beta/2}\right)$$

$$a_2 = \frac{4}{T_s}\left(\alpha + \sqrt{\alpha^2 - \beta/2}\right)$$

Taking the inverse Laplace transform of (16) yields

$$\Delta R(t) = A\left[\left(\frac{1}{a_1 a_2} + \frac{a_2 e^{-a_1 t} - a_1 e^{-a_2 t}}{a_1 a_2 (a_1 - a_2)}\right)u(t) - \left(\frac{1}{a_1 a_2} + \frac{a_2 e^{-a_1(t-T)} - a_1 e^{-a_2(t-T)}}{a_1 a_2 (a_1 - a_2)}\right)u(t-T)\right]. \tag{17}$$

Figure 19 illustrates the values of $\Delta R$ as a function of time at a range of 10 nmi with an acceleration A = 0.1g (g = 32 ft/sec$^2$) and a burn time T = 10 sec, while Figure 20 shows the variations of $\Delta R$ for A = 0.1g and T = 10 sec at a range of 2 nmi. It can be easily seen that the error due to 0.1g acceleration is well below the $1\sigma$ specifications for the range error ($1\sigma$ = 40 ft and 100 ft at 2 nmi and 10 nmi, respectively). Since it is believed that the value of the acceleration (A) will actually be of the same order of magnitude as 0.1g or less, no problems are anticipated in tracking radial accelerations during target approach.

### 3.2.3 Tangential Acceleration

While it was shown that the radial acceleration affects the range measurements, the tangential acceleration has a direct effect on the angle and angle rate measurements. The deterministic angle and angle rate tracking loop [1] is shown in Figure 21. In the figure,

$\theta_T$ = actual target angle

$\theta_A$ = antenna angle

$\Delta_\varepsilon = \theta_T - \theta_A$ = angular error

$\hat{\dot{\theta}}_T$ = estimate of the angle rate

K = effective loop gain

$\tau$ = time constant

K and $\tau$ are given in [4] as a function of range and are listed in Table 5.

Table 5. Angle Tracking Loop Parameters

| | Range (nmi) | | |
|---|---|---|---|
| | <1.9 | 1.9 - 3.8 | >3.8 |
| K | 0.5685 | 0.2221 | 0.0288 |
| $\tau$ | 2.7 | 4.25 | 12 |

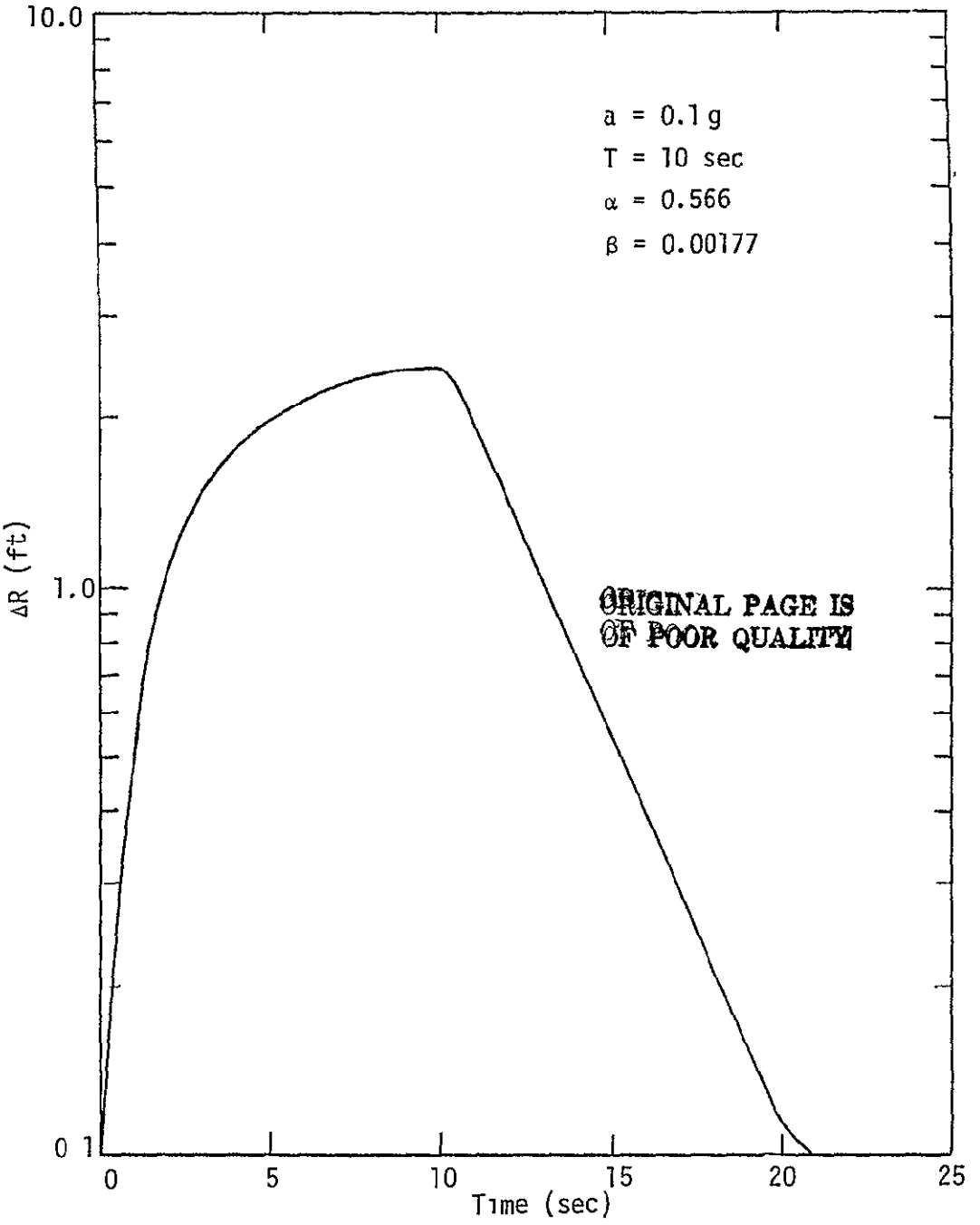


Figure 19. Range Error Due to Constant Acceleration Lasting T Seconds (R = 10 nmi)

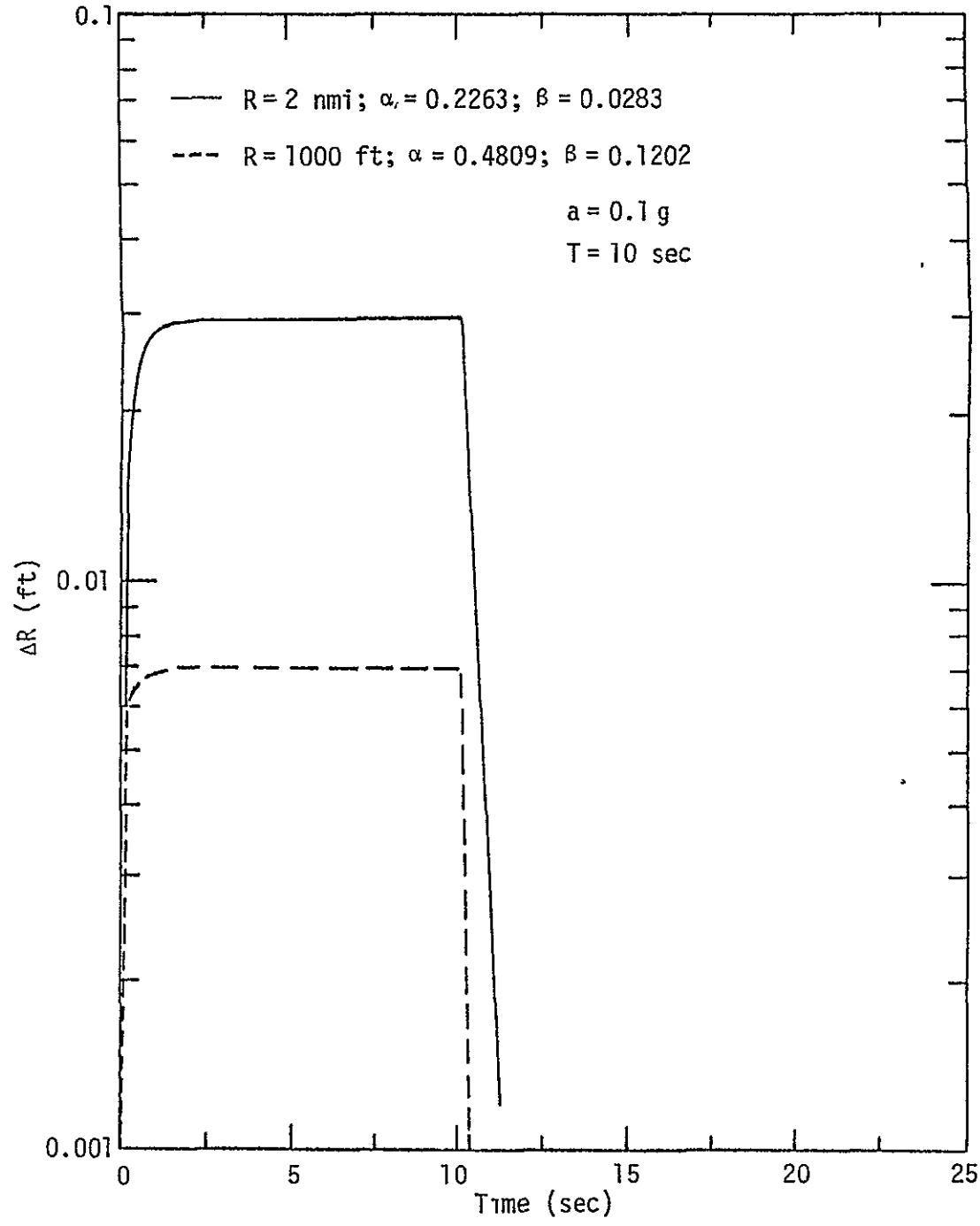


Figure 20. Range Error Due to Constant Acceleration Lasting T Seconds (R = 2 nmi)

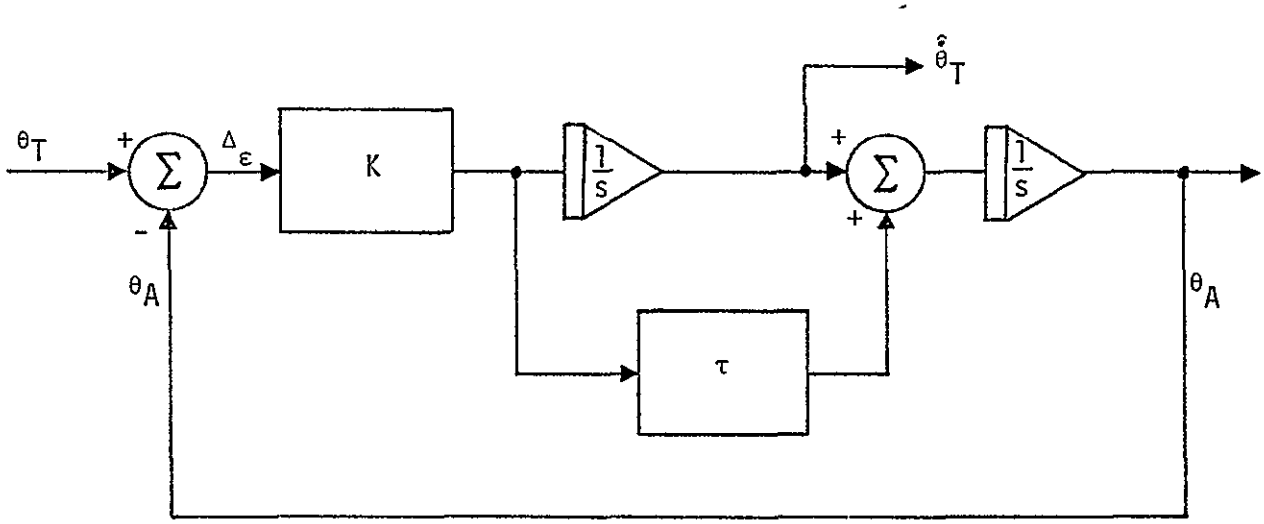


Figure 21. Deterministic Angle Tracking Loop

Using Figure 21, it can be written that

$$\Delta_\varepsilon(s) = \frac{s^2}{s^2 + K(s\tau + 1)}\,\theta_T(s) \tag{18a}$$

$$\hat{\dot{\theta}}_T(s) = \frac{Ks}{s^2 + K(s\tau + 1)}\,\theta_T(s)\,. \tag{18b}$$

However, assuming that the retro rockets will cause a constant tangential acceleration A for T sec, the target angle transform can be written as

$$\theta_T(s) = \frac{A}{Rs^2}\left[\frac{1}{s}(1 - e^{-sT})\right], \tag{19}$$

where the range R is assumed much larger than the tangential displacement that takes place in T sec.

Combining (18) and (19) and taking the inverse Laplace transform yields the following results for the angle error and the angle rate error.

$$\Delta\varepsilon(t) = \begin{cases} \dfrac{A}{R}\left[\dfrac{1}{a_1 a_2} + \dfrac{a_2 e^{-a_1 t} - a_1 e^{-a_2 t}}{a_1 a_2 (a_1 - a_2)}\right]; & t < T \\ \dfrac{A}{R a_1 a_2 (a_1 - a_2)}\left[a_2 e^{-a_1 t}(1 - e^{a_1 T}) - a_1 e^{-a_2 t}(1 - e^{a_2 T})\right]; & t \geq T \end{cases} \tag{20}$$

$$\Delta\dot{\varepsilon}(t) = \begin{cases} \dfrac{KA}{R a_1 a_2 (a_1 - a_2)}\left[t(a_1 - a_2) + \dfrac{a_2}{a_1}(1 - e^{-a_1 t}) - \dfrac{a_1}{a_2}(1 - e^{-a_2 t})\right] - \dfrac{A}{R} t; & t < T \\ \dfrac{AK}{R a_1 a_2 (a_1 - a_2)}\left[T(a_1 - a_2) + \dfrac{a_1}{a_2} e^{-a_2 t}(1 - e^{a_2 T}) - \dfrac{a_2}{a_1} e^{-a_1 T}(1 - e^{a_1 T})\right] & \\ \quad - \dfrac{A}{R}; & t \geq T \end{cases} \tag{21}$$

where

$$a_1 = \frac{1}{2}\left(K\tau - \sqrt{K^2\tau^2 - 4K}\right)$$

$$a_2 = \frac{1}{2}\left(K\tau + \sqrt{K^2\tau^2 - 4K}\right).$$

As is the case in the range tracking loop, the system is slightly overdamped for all values of K and $\tau$ given in Table 5. (The discriminant of the denominator of (18) is positive.)

Figure 22 illustrates the behavior of the angle error for a burn time T = 10 sec and an acceleration A = 0.1g for various ranges, while Figure 23 illustrates the angle error at a range R = 1000 ft for a number of burn times. Comparing the obtained results with the angle random error specifications, it can easily be seen that the error due to acceleration is always less than $3\sigma$ and is less than $1\sigma$ for all the cases considered except for ranges less than 1000 ft and burn times larger than 2 sec. In the latter two cases, the recovery time, which can be defined as the time required after the burn to reside below the specifications ($1\sigma$), is equal to 4 sec. Since the actual magnitudes

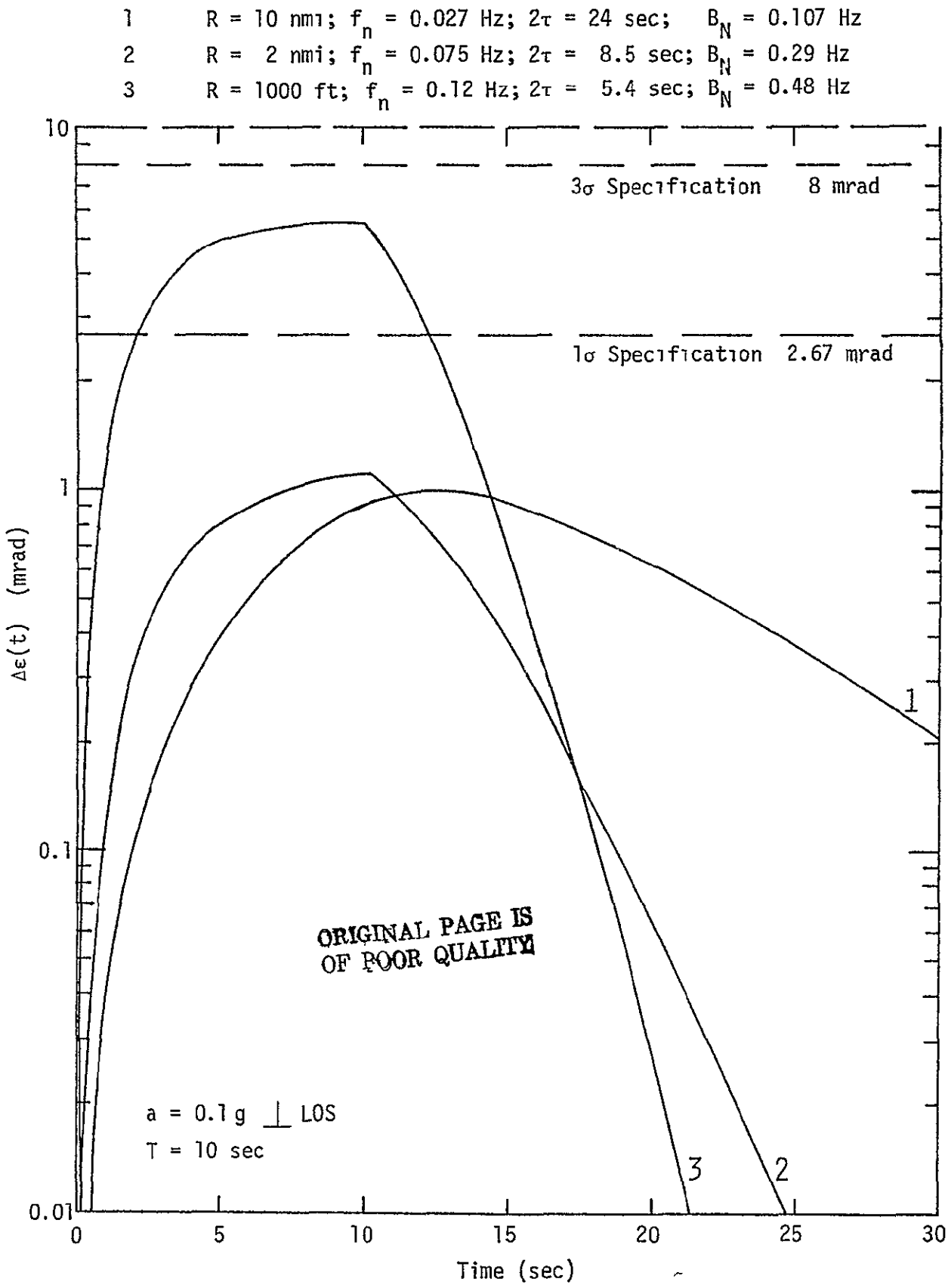


Figure 22. Angle Error Due to Tangential Acceleration With Range as a Parameter

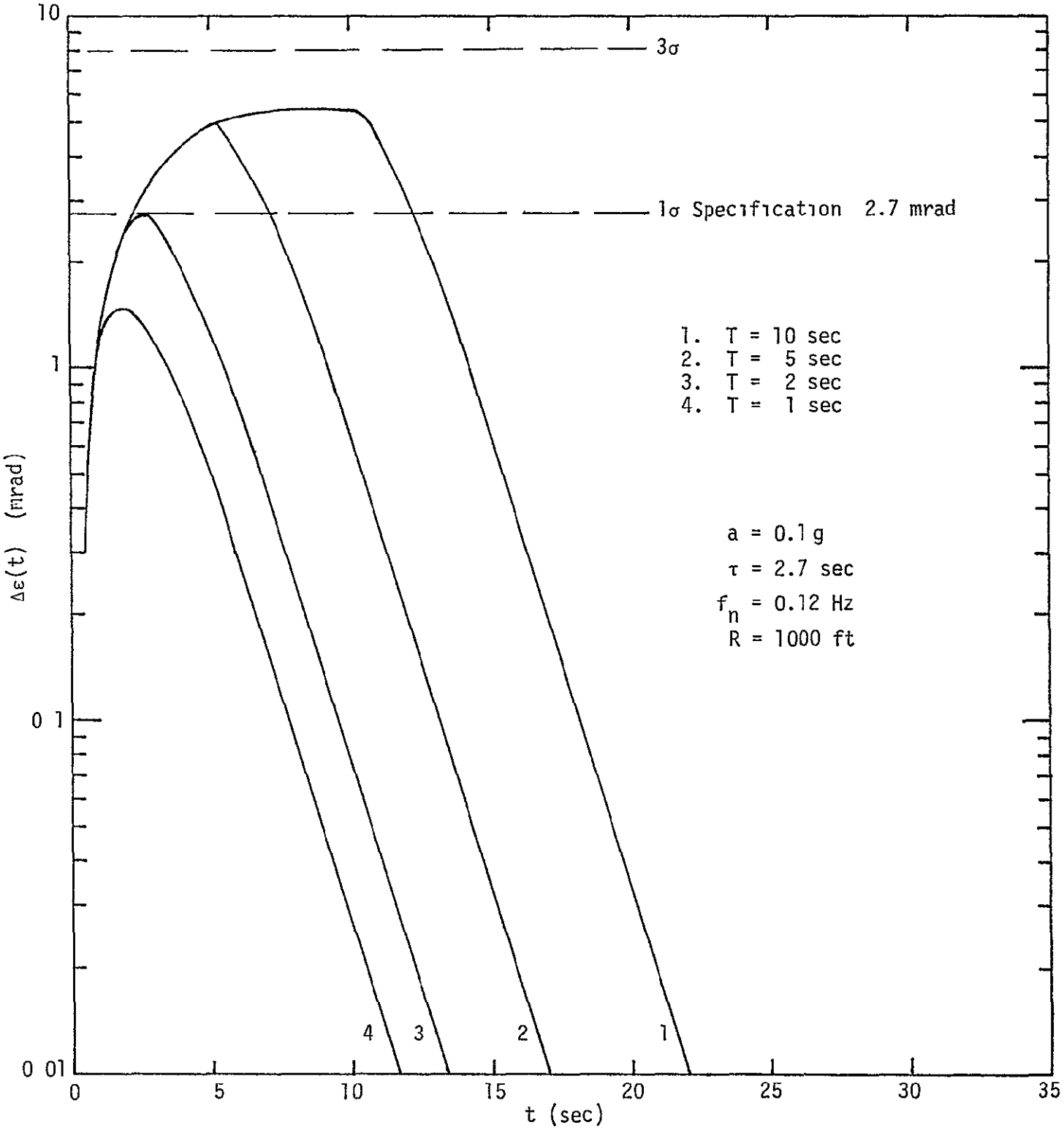


Figure 23 Angle Error Due to Acceleration With Burn Time as a Parameter

of acceleration are believed to be in the range of 0.1g or less, the angle errors due to tangential accelerations are not believed to constitute a major problem for angle tracking.

Similar to the angle error variations, the angle rate error variations are illustrated in Figures 24 and 25 for the same parameters as used in Figures 22 and 23, respectively. It is evident that the angle rate errors due to acceleration exceed the $3\sigma$ angle rate specifications for all cases studied. For the close range of 1000 ft, the recovery times to reside within $1\sigma$ of the angle rate specifications are 8, 8.75, 9.25 and 9.30 sec for burn times of 1, 2, 5 and 10 sec, respectively. All of these recovery times exceed the desired 2 sec recovery time. In order to reduce the angle rate acceleration errors to the desired levels, the equivalent noise bandwidth of the angle tracking loop has to be widened considerably, which would result in an appreciable increase in the angle and angle rate errors due to thermal noise. It is believed that, short of major design changes, any attempt to reduce the angle rate recovery times to within the desired value of 2 sec is unrealistic. It is therefore recommended that no design changes be considered due to the fact that angle rate estimation does not meet specification values within 2 sec after a burn.

Responses from other values of accelerations for any of the cases in this section can be obtained simply by scaling the desired value with respect to that shown on the appropriate figure. This is due to the fact that, at high values of SNR and the small accelerations considered, the systems are nearly linear. The same scaling cannot be carried out in the time dimension, however.

### 3.2 4 Angular Acceleration Testing

One of the radar testing procedures proposed by NASA is to fly a target (airplane) at an altitude R in a circular path of radius r and an angular velocity of $\omega$ radians/sec, as shown in Figure 26.

The angular acceleration being tracked by the radar is then

$$\ddot{\theta}_T(t) = \frac{r\omega^2}{R} \cos \omega t . \qquad (22)$$

1 R = 10 nmi; $f_n$ = 0.027 Hz; $2\tau$ = 24 sec; $B_N$ = 0.107 Hz
2 R = 2 nmi; $f_n$ = 0.075 Hz; $2\tau$ = 8.5 sec; $B_N$ = 0.29 Hz
3 R = 1000 ft; $f_n$ = 0.12 Hz; $2\tau$ = 5.4 sec; $B_N$ = 0.48 Hz

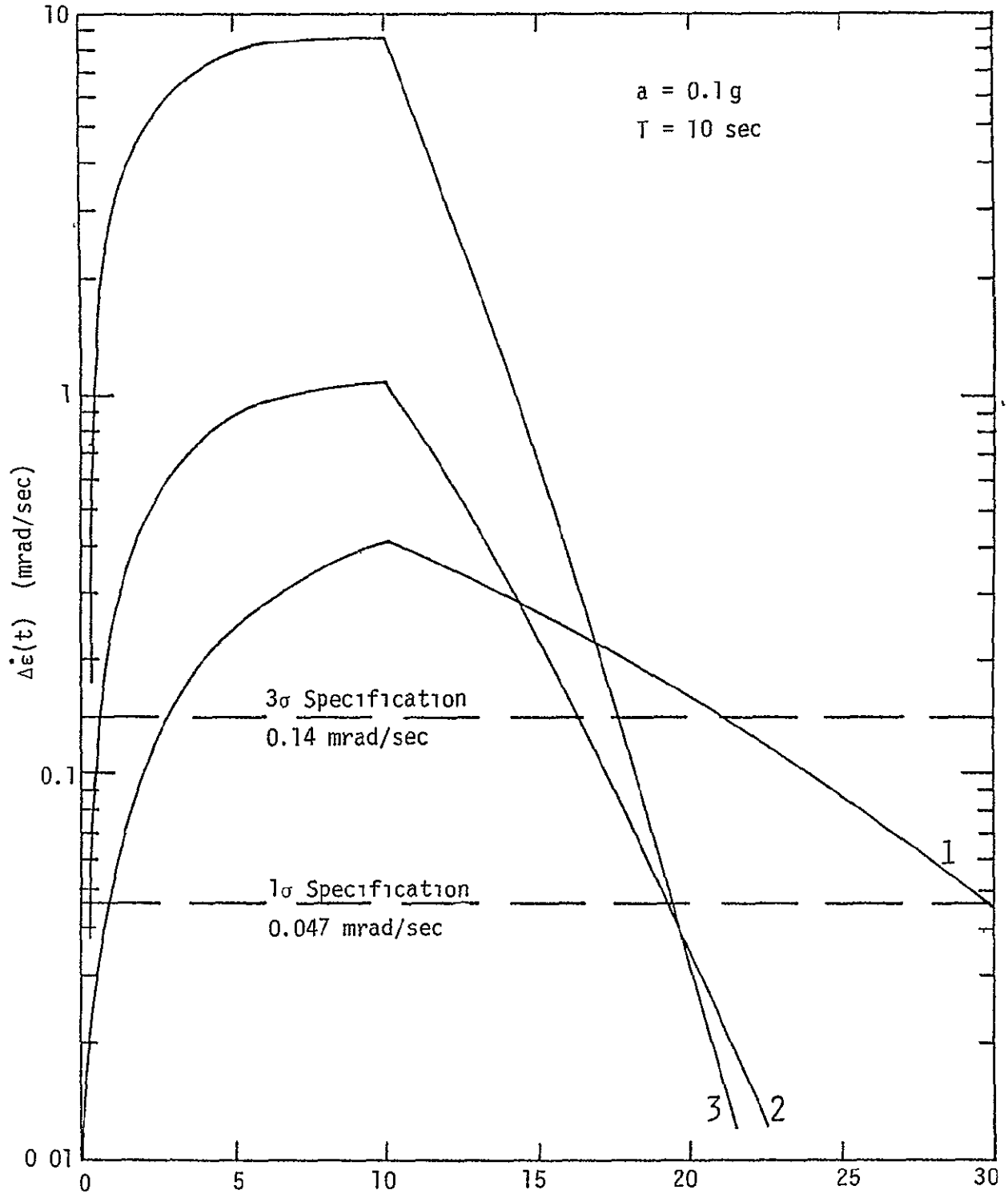


Figure 24. Angle Rate Error Due to Acceleration With Range as a Parameter

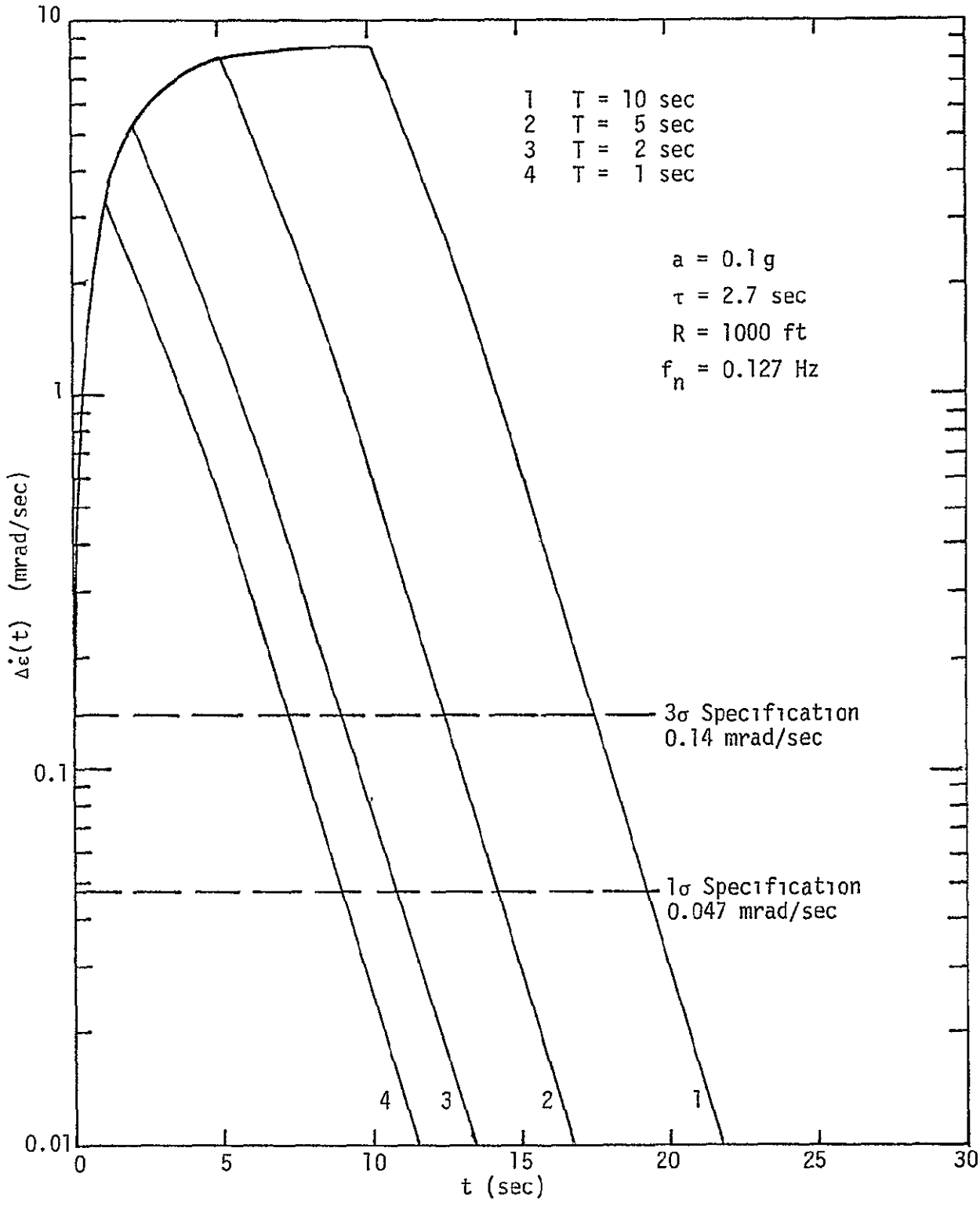


Figure 25. Angle Rate Error Due to Acceleration With Burn Time as a Parameter

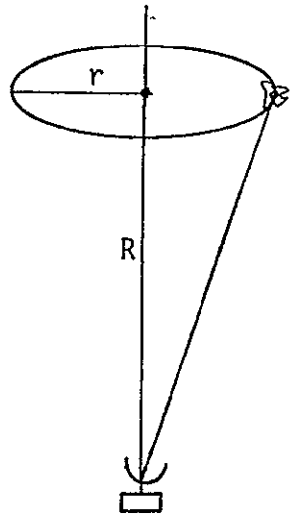


Figure 26. Radar Angle Tracking Testing

The Laplace transform of the angle being tracked can be simply shown to be [3]:

$$\theta_T(s) = \frac{r\omega^2}{Rs(s^2+\omega^2)} . \tag{23}$$

Substituting (23) in (18) results in

$$\Delta_\varepsilon(s) = \frac{r\omega^2 s}{R(s^2+\omega^2)(s^2+K(\tau s+1))} \tag{24a}$$

and

$$\hat{\theta}_T(s) = \frac{r\omega^2 K}{R(s^2+\omega^2)(s^2+K(\tau s+1))} . \tag{24b}$$

Taking the inverse Laplace transform of (24a), and after considerable algebraic manipulation, the angle and angle rate errors are found to be

$$\Delta_\varepsilon(t) = \frac{r\omega^2}{R}\left[\frac{\gamma e^{-\gamma t}}{(\gamma-\delta)(\gamma^2+\omega^2)} + \frac{\delta e^{-\delta t}}{(\delta-\gamma)(\delta^2+\omega^2)} - \sqrt{\frac{1}{(\gamma^2+\omega^2)(\delta^2+\omega^2)}}\cos(\omega t+\psi)\right] .$$

The first two terms represent the transient behavior; hence, they can be dropped in the steady-state response calculations, which results in

$$\Delta_{\varepsilon_{ss}}(t) = -\frac{r\omega^2}{R}(\gamma^2+\omega^2)^{-1/2}(\delta^2+\omega^2)^{-1/2}\cos(\omega t+\psi), \qquad (25)$$

where

$$\psi = \frac{\pi}{2} + \tan^{-1}\left(\frac{\delta}{\omega}\right) - \tan^{-1}\left(\frac{\omega}{\gamma}\right)$$

$$\delta = \frac{1}{2}\left[K\tau - \sqrt{K^2\tau^2 - 4K}\right]$$

$$\gamma = \frac{1}{2}\left[K\tau + \sqrt{K^2\tau^2 - 4K}\right]$$

As expected, the steady-state response is a sinusoidal function of time, as is the input with a different amplitude and phase shift.

The steady state of the angle rate response can be derived similarly, yielding

$$\Delta_{\dot{\varepsilon}_{ss}}(t) = -\frac{A}{\omega}\sqrt{\frac{(\gamma\delta-\omega^2-K)^2+\omega^2(\delta+\gamma)^2}{(\delta^2+\omega^2)(\omega^2+\gamma^2)}}\cos(\omega t+\phi), \qquad (26)$$

where

$$\phi = \tan^{-1}\left[\frac{\omega(\delta+\gamma)}{\gamma\delta-\omega^2-K}\right] + \tan^{-1}\left(\frac{\delta}{\omega}\right) - \tan^{-1}\left(\frac{\omega}{\gamma}\right).$$

Equations (25) and (26) provide the required expressions for the theoretical evaluation of the angle and angle rate performance in the proposed testing and thus establish the basis for comparing the experimental results with the theoretical analysis.

## 4.0 SIMULATION AT SHORT RANGE

The results of the previous sections, target effects and other effects are combined in this section to develop an overall model of the Ku-band radar at short ranges (less than a few thousand feet). The extension of the model to longer ranges does not involve extensive modification. This model is developed so that it can be programmed directly into a digital computer simulation.

There are various simulations at NASA JSC of the Orbiter and, in particular, of the proximity and docking operations. Some have a man in the loop and others do not. Some operate real-time and others do not. The simulation model presented here is developed so that it is essentially modular. That is, with minor interfacing, the simulation model can be used in any of the simulations presently operating at NASA JSC.

The simulation model will interface with the existing simulations as shown in Figure 27. The existing Orbiter simulations continuously provide a "trajectory information vector" to the radar simulation. Among the components of the trajectory information vector, T(t), are

$$T(t) \triangleq \begin{bmatrix} R(t) \\ \dot{R}(t) \\ \ddot{R}(t) \\ \theta_{AZ}(t) \\ \dot{\theta}_{AZ}(t) \\ \ddot{\theta}_{AZ}(t) \\ \theta_{EL}(t) \\ \dot{\theta}_{EL}(t) \\ \ddot{\theta}_{EL}(t) \\ L_R(t) \\ L_\theta(t) \end{bmatrix} \quad \begin{array}{l} \text{Range along LOS} \\ \text{Velocity along LOS} \\ \text{Acceleration along LOS} \\ \text{Azimuth angle} \\ \text{Azimuth angular rate} \\ \text{Azimuth angular acceleration} \\ \text{Elevation angle} \\ \text{Elevation angular rate} \\ \text{Elevation angular acceleration} \\ \text{Effective target length along LOS} \\ \text{Effective target length perpendicular to LOS} \end{array} \qquad (27)$$

The components of T(t) in (27) are not intended to be complete. The radar simulation assumes these components are available when necessary.

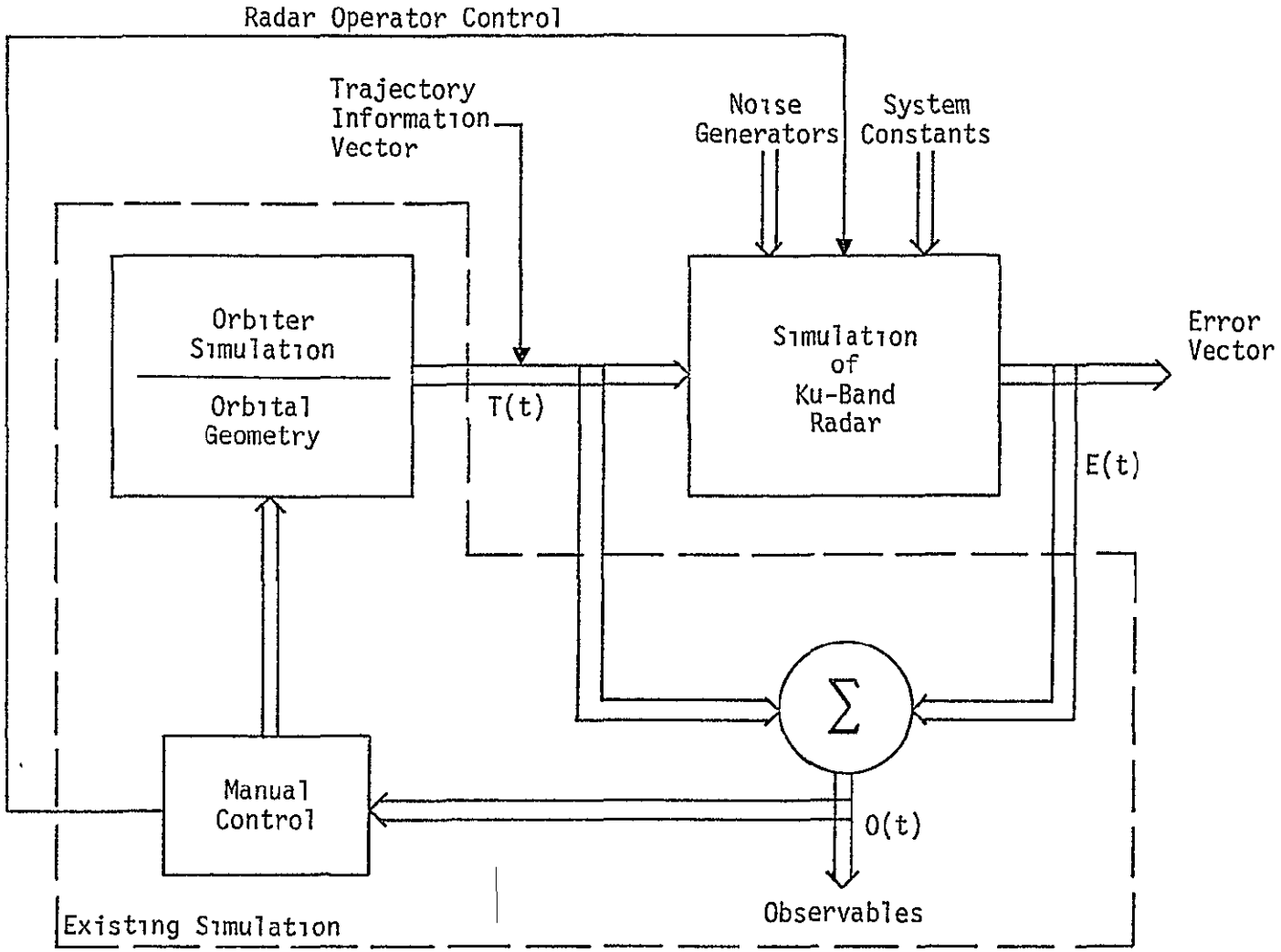


Figure 27. General Block Diagram of Orbital Simulation and the Simulation of the Ku-Band Radar

Other necessary inputs to the radar simulation are internal system constants, e.g., PRF, pulse width, and a set of mutually independent random noise generators. Both uniform and Gaussian random noise generators will be needed.

The radar simulation will output an error vector, each component of which will represent a tracking or an estimation error. Each of these errors will be the result of several error contributors. The effect of each contribution will also be available. The error vector is sent back to the existing simulator when some or all of the error components are added to the components of T(t). The measured or observed variables are then given by

$$\theta(t) = T(t) + E(t) . \tag{28}$$

In the succeeding parts of this section, the necessary components of the radar simulation are detailed. Finally, the overall description is examined again at the conclusion of this section.

## 4.1 Simulation of Thermal Noise and Target Scintillation Effects

In order to simulate the errors due to thermal noise and target scintillation on a digital computer, discrete models for the tracking loop operations must be developed. In the Ku-band radar, there are two primary closed tracking loops to track range and angle. The range rate is tracked via an open loop, and the angle rate is estimated in the angle tracking loop [1].

### 4.1.1 Tracking Error Simulation Due to Thermal Noise and Target Scintillation in Range, Angle, and Angle Rate Tracking

The range tracking loop is shown in Figure 28, while the angle tracking loop is shown in Figure 29. All the parameters are defined in [1, Appendices E and F] and will not be repeated here.

In the range tracking loop, the closed loop transfer function between the noise input $n_x$ and the estimated time of signal arrival (range) $\hat{T}$ is given by [1, Appendix F].

$$H_R(s) = \frac{\alpha' \left(s + \beta'/(\alpha' T_s)\right)}{s^2 + \alpha' s + \beta'/T_s} , \tag{29}$$

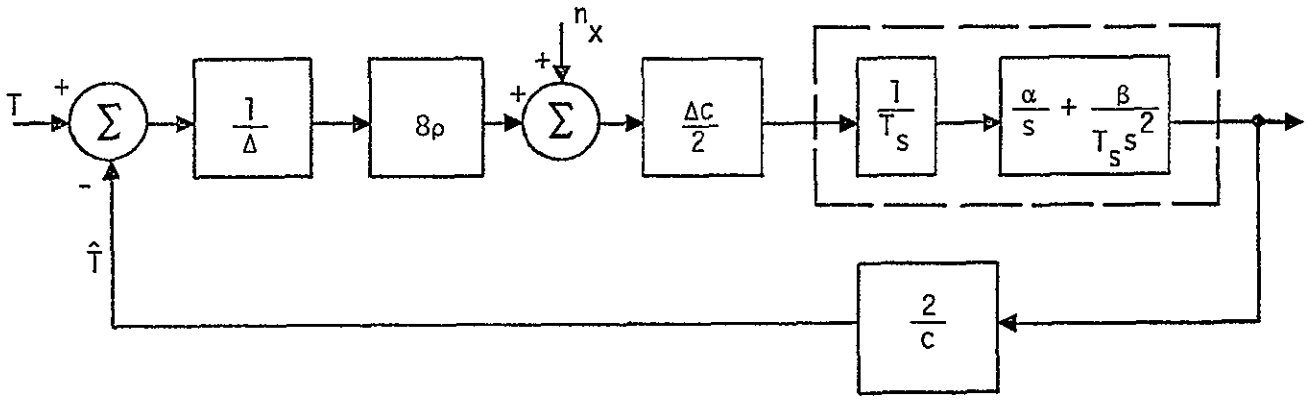


Figure 28. Range Tracking Loop Block Diagram [1, Appendix F]

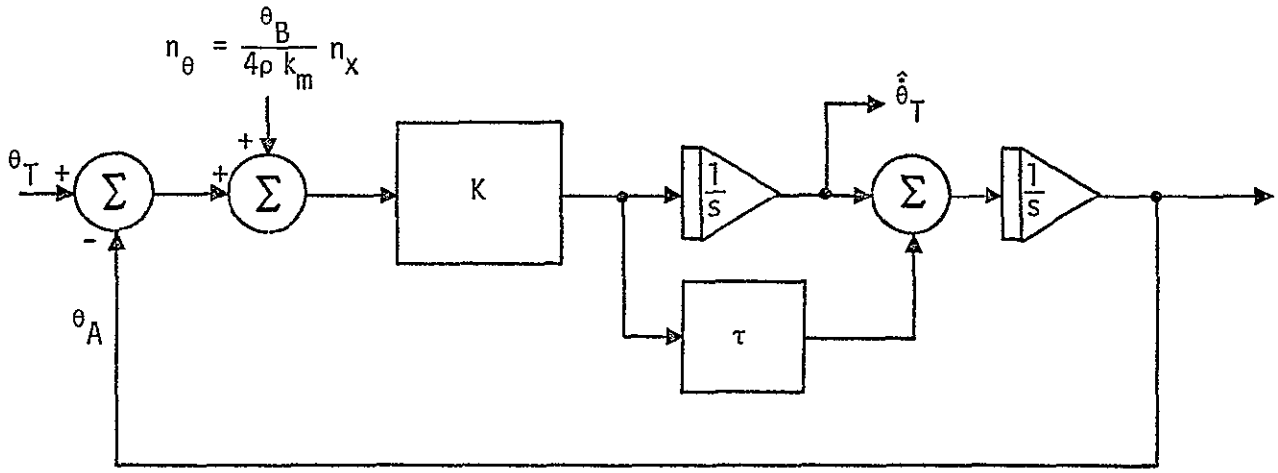


Figure 29. Angle Tracking Loop Block Diagram Showing Angle Rate Estimator [1, Appendix D]

where $\alpha'$ and $\beta'$ are related to the $\alpha$-$\beta$ tracker parameters via the equations:

$$\alpha' \triangleq \frac{8\rho_R \alpha}{T_s}$$

$$\beta' \triangleq \frac{8\rho_R \beta}{T_s} .$$

$T_s$ is the time per sample of the Gaussian random noise $n_x$ by the D/A converter whose mean is zero and whose variance is equal to $\sigma_{xR}^2$ [1]. This variance is a function of the signal-to-noise ratio and the number of independent samples (N) being post-integrated. For range tracking, N = 20.

Similarly, for the angle tracking loop, the closed loop transfer function between the input noise $n_\theta$ and the angle estimate $\theta_A$ is given by [1, Appendix D]

$$H_\theta(s) = \frac{K(\tau s + 1)}{s^2 + K(\tau s + 1)} , \tag{30}$$

whereas the associated transfer function for the angle rate is [1, Appendix D]:

$$H_{\dot\theta}(s) = \frac{Ks}{s^2 + K(\tau s + 1)} , \tag{31}$$

where K is the equivalent loop gain and $\tau$ is a time constant defined in [1].

The noise $n_\theta$ is Gaussian random noise with zero mean and variance equal to

$$\sigma_{n\theta}^2 = \left(\frac{\theta_B}{4\rho_\theta k_m}\right)^2 \sigma_{x\theta}^2 . \tag{32}$$

The variance $\sigma_{x\theta}^2$, as is the case in the range tracking loop, is a function of the signal-to-noise ratio and the number of independent samples (N) being post-integrated. For angle tracking, N = 10.

It is evident from (29) through (31) that the three transfer functions can be parameterized using the general formula

$$H(s) = \frac{a_4(s+a_3)}{(s+a_1)(s+a_2)} . \tag{33}$$

This is possible since for all the parameters under consideration the denominators of the transfer functions have positive discriminants. The latest values of $\alpha$, $\beta$, $\tau$, and K are summarized in Table 6, while the parameters $a_1$, $a_2$, $a_3$, and $a_4$ are defined for the three cases in Table 7. It is noted that $a_1$, $a_2$, $a_3$, and $a_4$ are all positive numbers and that $a_1 > a_2$.

4.1.2 Stochastic Process Modeling

The continuous stochastic process modeling of the continuous tracking loops can now be obtained as shown in Figure 30. The equations describing the processes are

$$\dot{x}_1(t) = -a_2 x_1(t) - (a_1 - a_3) x_2(t) + a_4 u(t)$$

$$\dot{x}_2(t) = -a_1 x_2(t) + a_4 u(t) ,$$

which can be written in a matrix form as

$$\dot{\underline{X}}(t) = \underline{A}\,\underline{X}(t) + \underline{B}\,u(t) , \tag{34}$$

where

$$\underline{X}(t) \triangleq \begin{bmatrix} x_1(t) \\ x_2(t) \end{bmatrix}, \quad \underline{A} \triangleq \begin{bmatrix} -a_2 & -(a_1-a_3) \\ 0 & -a_1 \end{bmatrix}, \quad \underline{B} \triangleq \begin{bmatrix} a_4 \\ a_4 \end{bmatrix} .$$

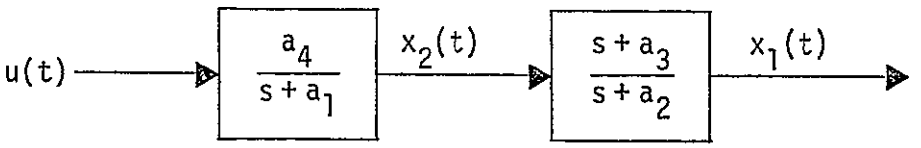


Figure 30. Continuous Stochastic Model

Table 6. Tracking Loop Parameters

| Parameter | Range (nmi) | | | | | |
|---|---|---|---|---|---|---|
| | <0.42 | 0.42-0 95 | 0.95-1.9 | 1.9-3.8 | 3.8-9.5 | >9 5 |
| $\alpha$ | 0.4809 | 0.4526 | 0.2263 | 0.2263 | 0.1132 | 0.0566 |
| $\beta$ | 0.1202 | 0.1132 | 0.0283 | 0.0283 | 0.00354 | 0.000884 |
| K $(rad)^2$ | 0.5685 | 0.5685 | 0.5685 | 0.2221 | 0.0288 | 0.0288 |
| $\tau$ (sec) | 2.7 | 2.7 | 2.7 | 4.25 | 12 | 12 |
| $T_s$ (msec) | 45.9 | 45.9 | 45.9 | 45 9 | 45.9 | 107.2 |

Table 7. General Transfer Function Parameters

$$H(s) = \frac{a_4(s+a_3)}{(s+a_1)(s+a_2)}$$

| Loop | $a_1$ | $a_2$ | $a_3$ | $a_4$ |
|---|---|---|---|---|
| Range | $\frac{\alpha' + \sqrt{\alpha'^2 - 4\beta'/T_s}}{2}$ | $\frac{\alpha' - \sqrt{\alpha'^2 - 4\beta'/T_s}}{2}$ | $\frac{\beta'}{\alpha' T_s}$ | $\alpha'$ |
| Angle | $\frac{K\tau + \sqrt{K^2\tau^2 - 4}}{2}$ | $\frac{K\tau - \sqrt{K^2\tau^2 - 4}}{2}$ | $\frac{1}{\tau}$ | $K\tau$ |
| Angle Rate | $\frac{K\tau + \sqrt{K^2\tau^2 - 4}}{2}$ | $\frac{K\tau - \sqrt{K^2\tau^2 - 4}}{2}$ | 0 | K |

In (34), the parameter being tracked is $x_1(t)$ [R, $\theta$ or $\dot{\theta}$]. Also, u(t) is white Gaussian noise with zero mean and a variance $\sigma_u^2$ equal to $\sigma_{xR}^2$ for the range tracking loop and equal to $\sigma_{n\theta}^2$ for the angle (angle rate) tracking loop.

The discrete time model of (34) can be written as

$$\underline{X}(k+1) = \underline{C}\,\underline{X}(k) + \underline{D}\,\underline{u}(k)\,. \tag{35}$$

In Appendix A of this report and in [5], matrices $\underline{C}$ and $\underline{D}$ are given by

$$\underline{C} = e^{\underline{A}T} \tag{36}$$

$$\underline{F} \triangleq \underline{D}[E\,\underline{u}(k)\,\underline{u}'(k)]\,\underline{D}' = \sigma_u^2 \int_0^T e^{\underline{A}x}\,\underline{B}\underline{B}'\,e^{\underline{A}x}dx\,, \tag{37}$$

where T is the computer update time.

There are numerous methods for finding $e^{\underline{A}T}$ [5-7]. One simple approach is

$$e^{\underline{A}T} = \mathscr{L}^{-1}\left\{[s\underline{I} - \underline{A}]^{-1}\right\}, \tag{38}$$

where $\mathscr{L}^{-1}$ is the inverse Laplace transform. Performing (38) yields

$$\underline{C} = e^{\underline{A}T} = \begin{bmatrix} e^{-a_2T} & \varepsilon\left(e^{-a_2T} - e^{-a_1T}\right) \\ 0 & e^{-a_1T} \end{bmatrix} \tag{39}$$

where

$$\varepsilon \triangleq \frac{a_3 - a_1}{a_1 - a_2}\,. \tag{40}$$

To calculate $\underline{D}$ and the covariance matrix of $\underline{u}(k)$, namely, $[E(\underline{u}(k)\,\underline{u}'(k))]$, the following integration has to be performed

$$\underline{F} = (a_4\sigma_u)^2 \int_0^T \begin{bmatrix} e^{-a_2x} & \varepsilon\left(e^{-a_2x} - e^{-a_1x}\right) \\ 0 & e^{-a_1x} \end{bmatrix} \begin{bmatrix} 1 & 1 \\ 1 & 1 \end{bmatrix} \begin{bmatrix} e^{-a_2x} & 0 \\ \varepsilon\left(e^{-a_2x} - e^{-a_1x}\right) & e^{-a_1x} \end{bmatrix} dx$$

which reduces to

$$\underline{F} = (a_4\sigma_u)^2 \times$$

$$\begin{bmatrix} \left( \frac{(1-e^{-a_2T})(1+\varepsilon)^2}{2a_2} - \frac{2\varepsilon(1+\varepsilon)(1-e^{-(a_1+a_2)T})}{a_1+a_2} + \frac{\varepsilon^2(1-e^{-2a_1T})}{2a_1} \right) & \frac{(1+\varepsilon)(1-e^{-(a_1+a_2)T})}{a_1+a_2} - \frac{\varepsilon(1-e^{-2a_1T})}{2a_1} \\ \frac{(1+\varepsilon)(1-e^{-(a_1+a_2)T})}{a_1+a_2} - \frac{\varepsilon(1-e^{-2a_1T})}{2a_1} & \frac{1-e^{-2a_1T}}{2a_1} \end{bmatrix}$$

(41)

Since $\underline{A}$ is in Jordan canonical form [7-8] and thus cannot be diagonalized, or since $x_1(t)$ and $x_2(t)$ are not independent, $\underline{u}(k)$ is a two-dimensional discrete process which implies that two Gaussian random generators are needed to realize this discrete process.

Assuming that the variance of $\underline{u}(k)$ is given by

$$E[\underline{u}(k)\ \underline{u}'(k)] = \begin{bmatrix} \sigma_1^2 & 0 \\ 0 & \sigma_2^2 \end{bmatrix},$$

which implies that the two components of u(k) are independent and expressing the matrix $\underline{D}$ as

$$\underline{D} = \begin{bmatrix} d_{11} & d_{12} \\ d_{21} & d_{22} \end{bmatrix},$$

then

$$\underline{F} \triangleq \underline{D}\ E(\underline{u}(k)\ \underline{u}'(k))\ \underline{D}' = \begin{bmatrix} d_{11}^2\sigma_1^2 + d_{12}^2\sigma_2^2 & d_{11}d_{21}\sigma_1^2 + d_{22}d_{12}\sigma_2^2 \\ d_{11}d_{21}\sigma_1^2 + d_{22}d_{12}\sigma_2^2 & d_{21}\sigma_1^2 + d_{22}^2\sigma_2^2 \end{bmatrix}$$

(42)

Equating (41) and (42) results in three equations to be solved for the entries of $\underline{D}$ and $E(\underline{u}(k)\,\underline{u}'(k))$. However, since there are six unknowns involved, three have to be chosen arbitrarily without violating the physical nature of the processes. Setting $\sigma_1^2 = 1$, $d_{11} = 1$, $d_{22} = 0$, and solving for the remaining entries results in:

$$d_{21} = \frac{\dfrac{1 - e^{-2a_1T}}{2a_1}}{\left(\dfrac{(1+\varepsilon)(1-e^{-(a_1+a_2)T})}{a_1+a_2}\right) - \left(\dfrac{\varepsilon(1-e^{-2a_1T})}{2a_1}\right)} \tag{43}$$

$$\sigma_2^2 = \frac{\left[\dfrac{(1+\varepsilon)(1-e^{-(a_1+a_2)T})}{a_1+a_2} - \dfrac{\varepsilon(1-e^{-2a_1T})}{2a_1}\right]^2}{\dfrac{1-e^{-2a_1T}}{2a_1}} (a_4\sigma_u)^2 \tag{44}$$

and

$$d_{12}^2 = \left[\frac{(1-e^{-2a_2T})(1+\varepsilon)^2}{2a_2} - \frac{2\varepsilon(1+\varepsilon)(1-e^{-(a_1+a_2)T})}{a_1+a_2} + \frac{\varepsilon^2(1-e^{-2a_1T})}{2a_1}\right](a_4\sigma_u)^2 - \sigma_2^2 . \tag{45}$$

A diagram of the discrete time model is shown in Figure 31, which results from (35) with $d_{11} = 1$, $d_{22} = 0$, and $\sigma_1^2 = 1$.

It is emphasized that, in order to simulate the thermal noise and amplitude scintillation effects for the range and angle tracking loops, <u>two</u> independent Gaussian noise generators are needed

### 4.1.3 <u>Software Implementation</u>

The actual implementation requires a software equivalent of Figure 31, where $\{a_i,\ i = 1,4\}$ can be calculated for a given range using Tables 6 and 7. The parameters $d_{21}$, $d_{12}$, and $\sigma^2$ are calculated using (43) through (45). In order to compute $d_{21}$, $d_{12}$, and $\sigma^2$, however, $\sigma_u^2$ (the variance of the input noise in the continuous model) has to be calculated. As stated previously, $\sigma_u^2$ is given by

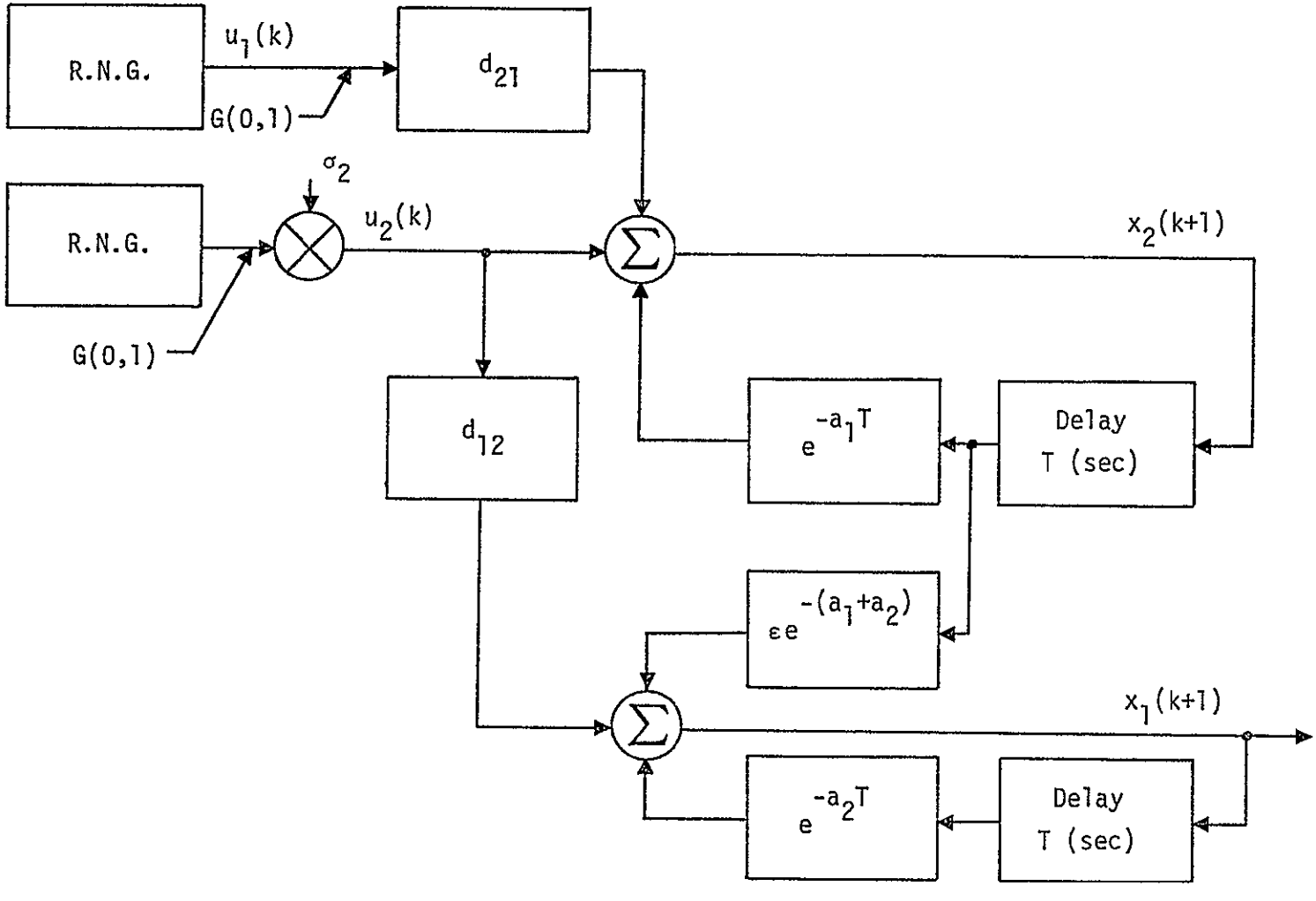


Figure 31. Diagram of Discrete Time Model for Range and Angle Tracking Loops

$$\sigma_{u_i}^2 = \begin{cases} \sigma_{xR}^2 & \text{for range tracking} \\ \left(\dfrac{\theta_B}{4\rho_\theta k_m}\right)^2 \sigma_{x\theta}^2 & \text{for angle and angle rate tracking} \end{cases} \tag{46}$$

where $\sigma_{x\theta}^2$ and $\sigma_{xR}^2$ have been calculated in [1] and are shown in Figure 32 as a function of signal-to-noise ratio (SNR) which is obtained from the radar equation. Figure 32 also shows $\sigma_{x\dot{R}}^2$, which is the variance of the input noise in range rate tracking, which will be discussed next. SNR is defined as the signal-to-noise ratio at the output of the doppler filters, SNR $\triangleq P_{avg\ r}/(N_0 B_F)$. For the Ku-band radar antenna, $\theta_B = 1.6°$ and $k_m = 1$. The only two additional parameters needed are the normalized correlation coefficients which are given as

$$\rho_R = \frac{1}{1 + \frac{4}{SNR}} \tag{47a}$$

for range, and

$$\rho_\theta = \frac{1}{1 + \frac{1}{SNR}} \tag{47b}$$

for angle and angle rate.

4.1.4 Tracking Errors Simulation Due to Thermal Noise and Target Scintillation in Range Rate Tracking

The simulation of the thermal noise and target scintillation errors in tracking range rate is simpler than the previous cases, due to the fact that range rate tracking is done via an open loop, where m successive readings are averaged to give the desired range rate estimate [1, Appendix G]. This is accomplished via a sliding window with m = 2 for R > 9.5 nmi and m = 4 for R < 9.5 nmi. Contrary to range tracking, the range rate estimate is not used to continuously update the locations of the 32 existing doppler filters but rather to select the doppler filter closest to the range rate reading [1]. To carry out the range rate simulation process, it is first necessary to compute the signal-to-noise ratio via the radar equation and then to compute the normalized correlation coefficient which is given by [1, Appendix G]:

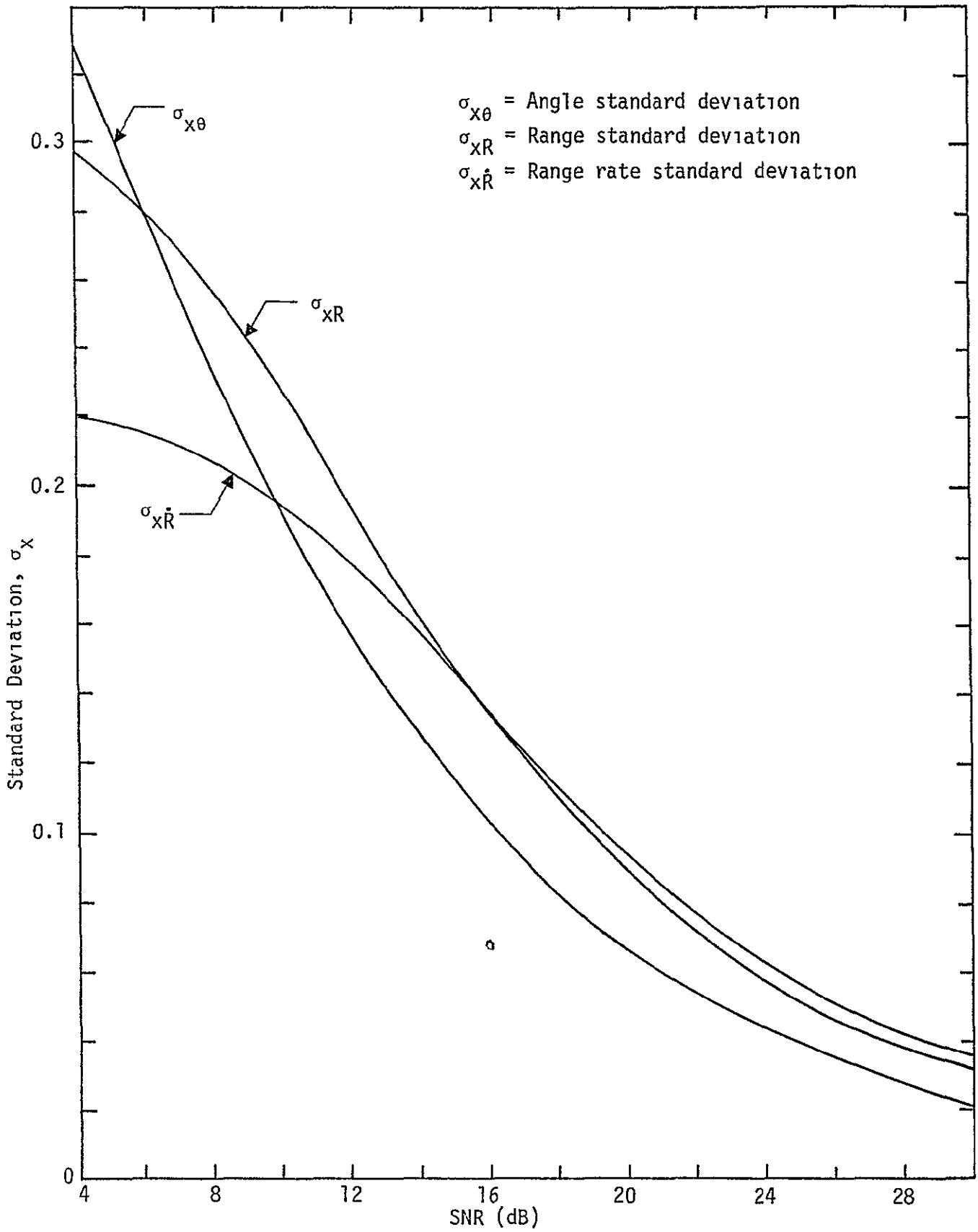


Figure 32. $\sigma_x$ Versus SNR for Range, Angle and Range Rate Tracking Loops [1]

$$\rho_{\dot{R}} = \frac{1}{1 + \frac{\pi^2}{SNR}} . \tag{48}$$

The variance $\sigma^2_{x\dot{R}}$ which is shown in Figure 32 is then computed, and the range rate mean square error per sample ($\sigma_{\dot{R}/s}$) is found using the following relation derived in [1, Appendix G]:

$$\sigma_{\dot{R}/s} = \left(\frac{c\, B_F}{16\, \rho_{\dot{R}}\, f_c}\right) \sigma_{x\dot{R}} , \tag{49}$$

where $B_F$ is the doppler filter single-sided noise bandwidth, c is the velocity of light in free space, and $f_c$ is the Ku-band RF frequency used. A white Gaussian noise generator is used with zero mean and a variance given by (49) to generate the required samples, and a sliding window averaging of the last m samples is used to give the range rate error, as illustrated in Figure 33.

The simulated errors in range, range rate, angle and angle rate tracking due to thermal noise and target scintillation are combined with the other types of error in each case of interest to produce the overall simulated tracking error.

## 4.2 Radar Simulation of Relative Accelerations

The responses of the various Ku-band radar tracking loops to accelerations orthogonal to and along the line-of-sight (LOS) have been analytically developed in section 3.2 of this report. The results of numerical computation are also presented in section 3.2. In this section, we present digital simulation models which allow for arbitrary accelerations. When simulated real time, this allows for evaluating acceleration effects when a human operator is in the loop.

### 4.2.1 Closed Loop Transfer Functions

In the absence of noise, the range tracking loop is shown in Figure 34. Using this figure, the closed loop transfer function between the range R and the range error is (in the complex frequency domain):

$$\Delta R(s) = \left[\frac{s^2}{s^2 + \left(\frac{8\alpha}{T_s}\right)s + \frac{8\beta}{T_s^2}}\right] R(s) . \tag{50}$$

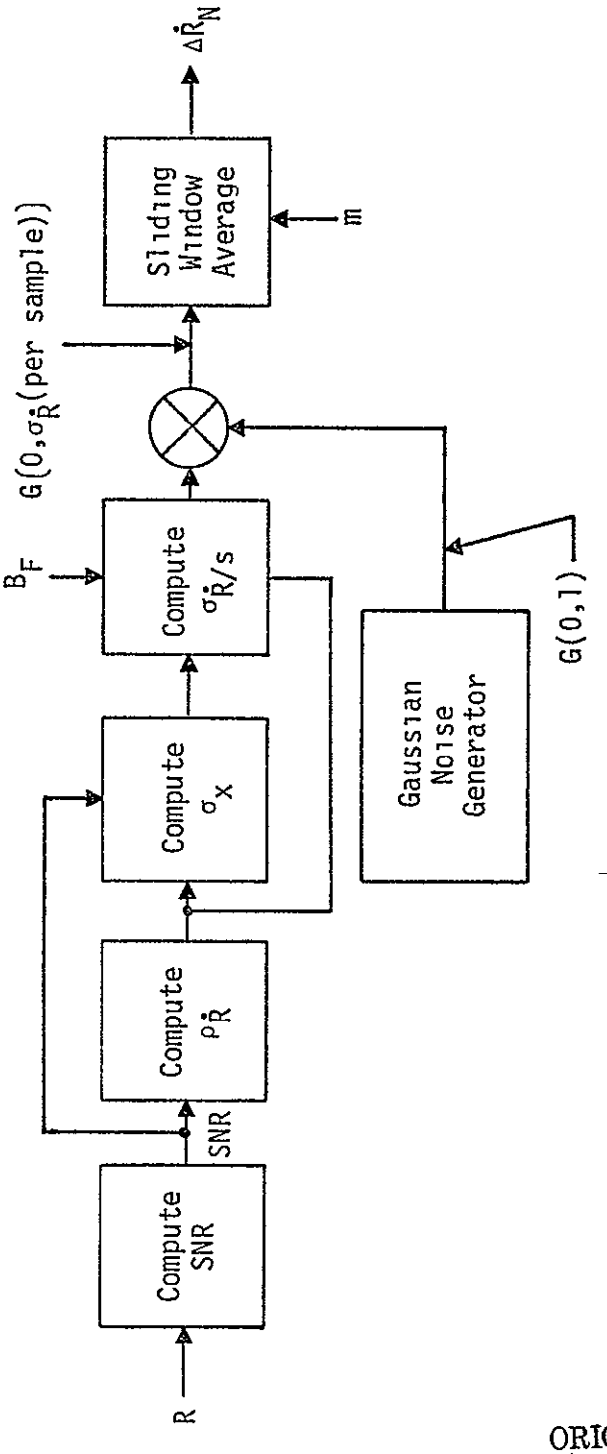


Figure 33. Simulation - Range Rate - Thermal Noise and Amplitude Scintillation Errors

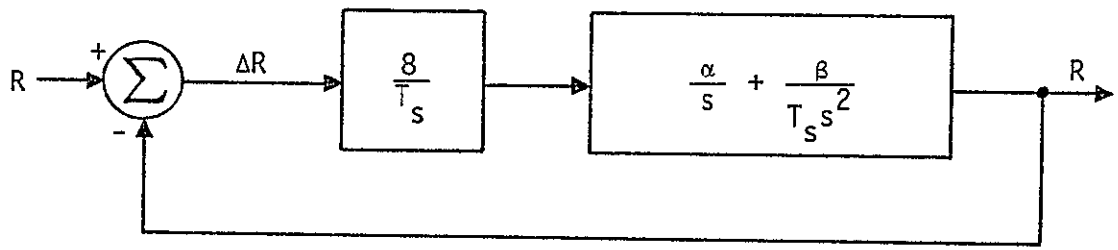


Figure 34. Range Tracking Loop Without Noise [1, Appendix F]

In terms of acceleration along the LOS, (50) becomes

$$\Delta R(s) = \left[\frac{1}{s^2 + \left(\frac{8\alpha}{T_s}\right)s + \frac{8\beta}{T_s^2}}\right] \ddot{R}(s) \tag{51}$$

We therefore define the transfer function between acceleration along the LOS and range error as

$$H_R(s) \triangleq \frac{1}{s^2 + \left(\frac{8\alpha}{T_s}\right)s + \frac{8\beta}{T_s^2}} . \tag{52}$$

For the angle tracking loop, in the absence of noise, the block diagram reduces to that in Figure 35. The relationship between the target angle $\theta_T$ and the angle error $\Delta\theta$ is

$$\Delta\theta(s) = \left[\frac{s^2}{s^2 + K(\tau s + 1)}\right] \theta_T(s) , \tag{53}$$

which, in terms of the angular acceleration, becomes

$$\Delta\theta(s) = \left[\frac{1}{s^2 + K(\tau s + 1)}\right] \ddot{\theta}_T(s) . \tag{54}$$

The closed-loop transfer function between angular error and angular acceleration ($\perp$ LOS) is defined as

$$H_\theta(s) = \frac{1}{s^2 + K(\tau s + 1)} . \tag{55}$$

Finally, also from Figure 35 for angle rate, the relationship between the angle rate estimate $\hat{\dot{\theta}}_T$ and the angle rate $\dot{\theta}_T$ is

$$\hat{\dot{\theta}}_T(s) = \frac{Ks}{s^2 + K(s\tau + 1)} \theta_T(s) = \frac{K}{s^2 + K(s\tau + 1)} \dot{\theta}_T(s) . \tag{56}$$

In terms of the error of the angular rate estimate, $\Delta\dot{\theta} \triangleq \dot{\theta}_T - \hat{\dot{\theta}}_T$, and angular acceleration, the relationship is

$$\Delta\dot{\theta}(s) = \frac{s + K\tau}{s^2 + K(s\tau + 1)} \ddot{\theta}_T(s) , \tag{57}$$

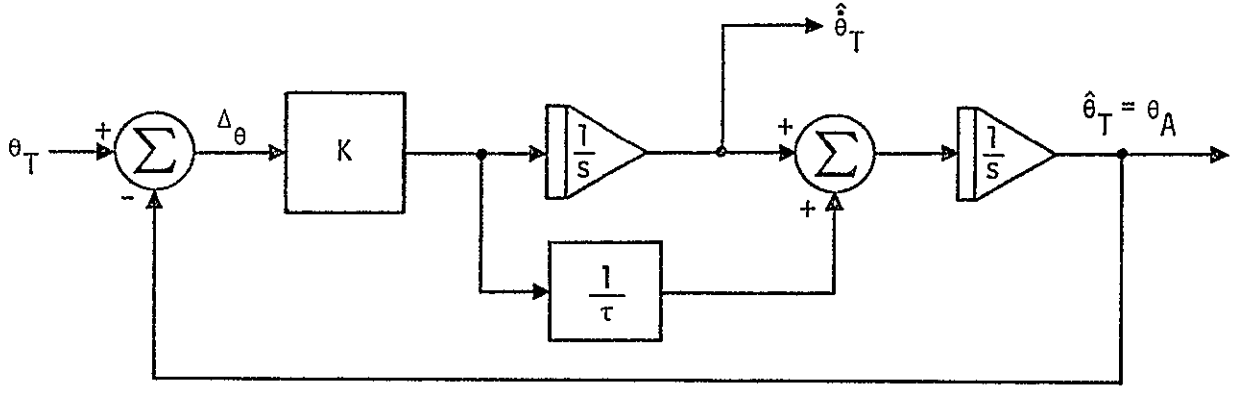


Figure 35. Angle Tracking Loop with Angle Rate Estimation Without Noise [1, Appendix D]

from which we define the transfer function relation angular acceleration and angle rate estimate error as

$$H_{\dot{\theta}}(s) = \frac{s + K\tau}{s^2 + K(s\tau + 1)} . \tag{58}$$

For acceleration, the three transfer functions of primary interest are given in (52), (55), and (58). We note that $H_R(s)$ and $H_\theta(s)$ are of the form

$$H_1(s) = \frac{1}{(s + a_1)(s + a_2)} \tag{59a}$$

and $H_{\dot{\theta}}(s)$ is of the form

$$H_2(s) = \frac{s + a_3}{(s + a_1)(s + a_2)} . \tag{59b}$$

The discriminants of the transfer functions are shown in Table 8, where it is observed that $a_1$ and $a_2$ are real and positive in all cases. Digital simulation algorithms will therefore be developed for $H_1(s)$ and $H_2(s)$ in (59) under the assumption that $a_1 > 0$ Also note that $a_1 > a_2$ in all cases.

Table 8. Discriminants for Acceleration Transfer Functions

| | Range | Angle | Angle Rate |
|---|---|---|---|
| $a_1$ | $\frac{4}{T_s}\left(\alpha + \sqrt{\alpha^2 - \beta/2}\right)$ | $\frac{1}{2}\left[K\tau + \sqrt{K^2\tau^2 - 4K}\right]$ | $\frac{1}{2}\left[K\tau + \sqrt{K^2\tau^2 - 4K}\right]$ |
| $a_2$ | $\frac{4}{T_s}\left(\alpha - \sqrt{\alpha^2 - \beta/2}\right)$ | $\frac{1}{2}\left[K\tau - \sqrt{K^2\tau^2 - 4K}\right]$ | $\frac{1}{2}\left[K\tau - \sqrt{K^2\tau^2 - 4K}\right]$ |
| $a_3$ | ----- | ----- | $K\tau$ |

4.2.2 Digital Simulation Algorithms for Acceleration

The inverse Laplace transforms of $H_1(s)$ and $H_2(s)$ are

$$h_1(t) = \left(\frac{1}{a_1 - a_2}\right)[\exp(-a_2 t) - \exp(-a_1 t)] \tag{60a}$$

$$h_2(t) = \left(\frac{1}{a_1 - a_2}\right)[(a_3 - a_2)\exp(-a_2 t) - (a_3 - a_1)\exp(-a_1 t)]. \tag{60b}$$

The z-transform of $h_i(t)$, $i = 1,2$, is given by [9-10]:

$$H_i(z) \triangleq \sum_{n=0}^{\infty} h_i(nT)\, z^{-n}, \qquad i = 1,2. \tag{61}$$

For $i = 1$, after some algebraic simplification, the z-transform can be written in closed form as

$$H_1(z) = \left(\frac{1}{a_1 - a_2}\right)\left[\frac{z^{-1}\left(e^{-a_2 T} - e^{-a_1 T}\right)}{z^{-2}\left(e^{-(a_1+a_2)T}\right) - z^{-1}\left(e^{-a_1 T} + e^{-a_2 T}\right) + 1}\right] \tag{62}$$

For $i = 2$, the closed form of the z-transform is

$$H_2(z) = \frac{z^{-1}\left(\varepsilon_1 e^{-a_2 T} - \varepsilon_2 e^{-a_1 T}\right) + (\varepsilon_2 - \varepsilon_1)}{z^{-2}\left(e^{-(a_2+a_1)T}\right) - z^{-1}\left(e^{-a_1 T} + e^{-a_2 T}\right) + 1}. \tag{63}$$

It is observed that $H_1(z)$ and $H_2(z)$ are of the same form, namely,

$$H(z) = \frac{A_0 + A_1 z^{-1}}{1 + B_1 z^{-1} + B_2 z^{-2}}. \tag{64}$$

This transform can be realized in several ways Assume the input sequence is $x(n)$ and the output sequence is $y(n)$, as shown in Figure 36. In the z-transform domain

$$y(z) = H(z)\,X(z) = \frac{A_0 + A_1 z^{-1}}{1 + B_1 z^{-1} + B_2 z^{-2}}\, x(z), \tag{65}$$

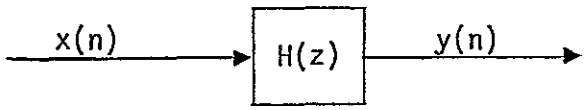


Figure 36. General Block Diagram of Digital Simulation for Acceleration

where, for causal filters, $z^{-1}$ represents a time delay of T seconds, T being the computer update time. In the time domain,

$$y(n) = -\left(B_1 y(n-1) + B_2 y(n-2)\right) + A_0 x(n) + A_1 x(n-1) . \qquad (66)$$

Three different realizations of this type of transfer function are shown in Figures 37 through 39. In Figure 37, the direct recursive realization is shown. The constants are those of H(z) in (64). The Canonic Realization is shown in Figure 38, where the constants are also those in (64). In both of these realizations, there is a severe accuracy limitation on the constants $\{A_1\}$ and $\{B_1\}$. As an alternative, the Parallel Canonic Realization is shown in Figure 39. This realization implements the representation

$$H(z) = \frac{\delta_1}{1 + \beta_1 z^{-1}} + \frac{\delta_2}{1 + \beta_2 z^{-1}} , \qquad (67)$$

which is a partial fraction expansion of H(z) in (64). This implementation is recommended since the accuracy on $\{\delta_i\}$ and $\{\beta_1\}$ in the Parallel Canonic Realization is not nearly as severe as the accuracies in the other two candidate realizations.

In this section, the similarities of the digital algorithms for simulating the effects of acceleration orthogonal to and along the LOS have been presented. The closed loop transfer functions between acceleration and the corresponding tracking error are given for all tracking loops in the Ku-band radar. Finally, specific implementation realizations are considered, and the recommended one is specified.

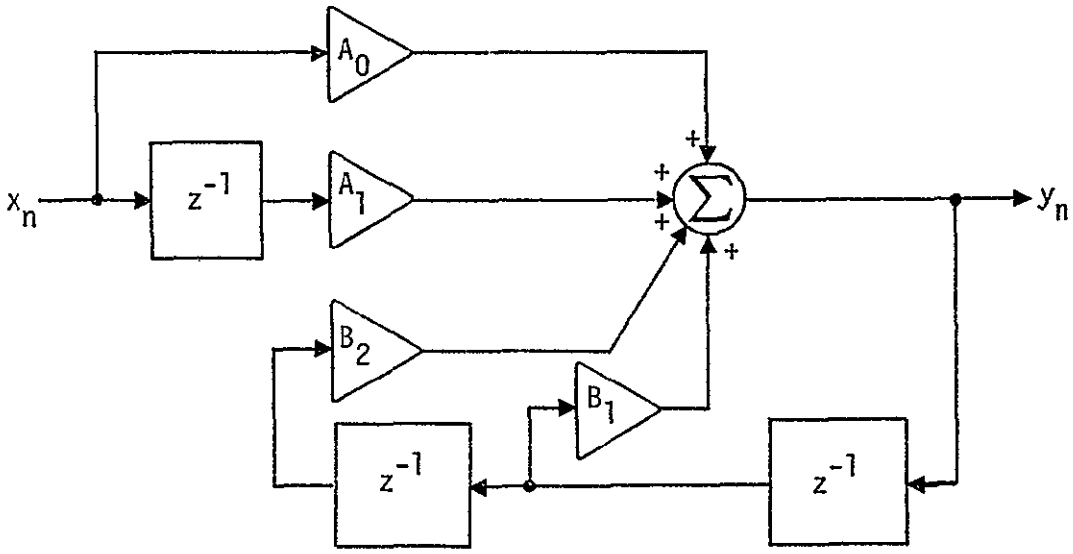


Figure 37. Direct Recursive Realization

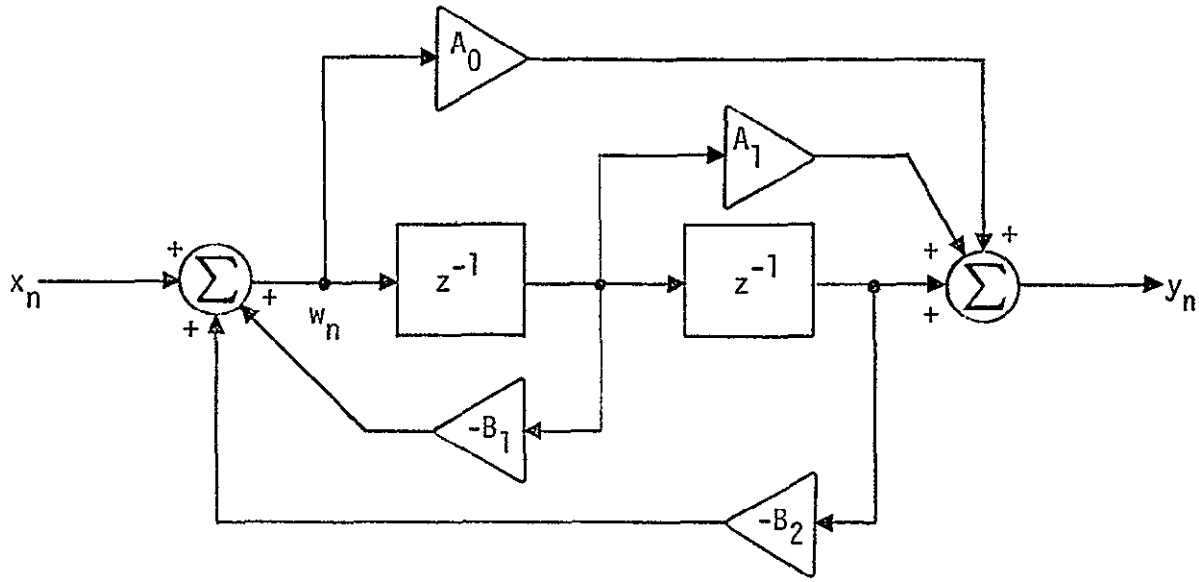


Figure 38. Canonic Realization

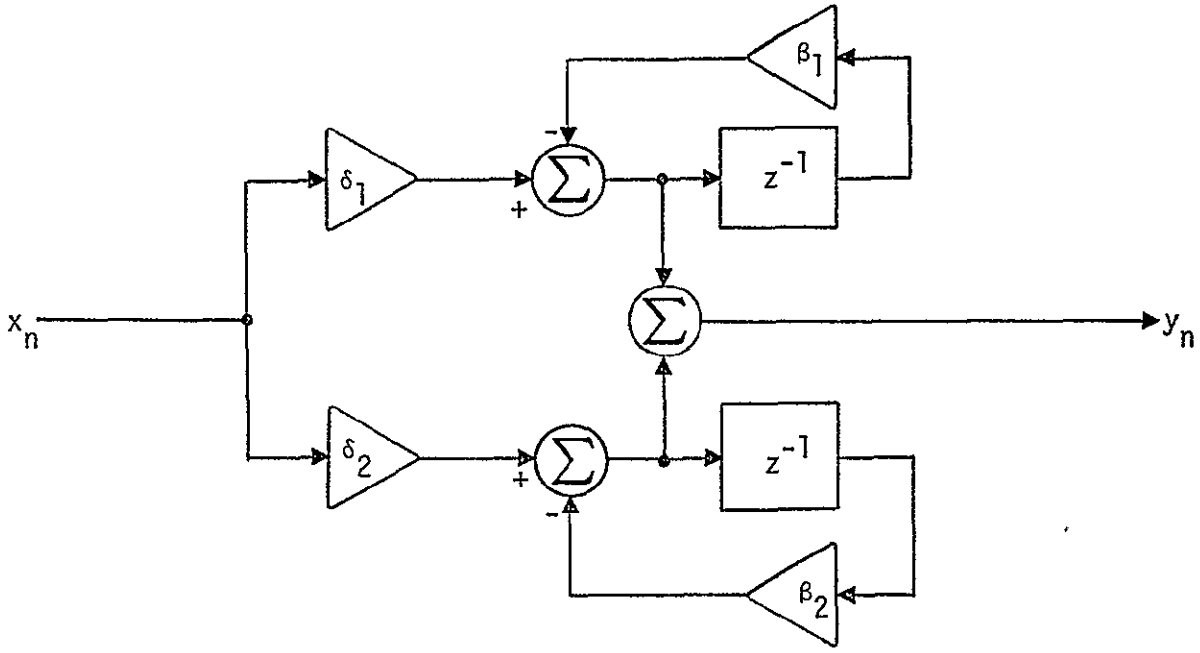


Figure 39. Parallel Canonic Realization

## 4.3 Range Rate Logarithmic Discriminant Error Simulation

In order to simulate the range rate logarithmic discriminant error, it is important to examine the nature of the problem. The range rate is estimated during track by using a set of 32 doppler filters and a log discriminant generator. The mean of the output of the log discriminant generator [E(z)] was found in [1, Appendix G] to be:

$$E(z) = \ln \left[ \frac{\dfrac{\cos^2(\pi\zeta)}{N^2 \sin^2\left[\frac{\pi}{32}(1-2\zeta)\right]} + \dfrac{4}{SNR}}{\dfrac{\cos^2(\pi\zeta)}{N^2 \sin^2\left[\frac{\pi}{32}(1+2\zeta)\right]} + \dfrac{4}{SNR}} \right], \tag{68}$$

where

$SNR \triangleq \dfrac{P_{avg\ r}}{N_0 B_F}$ = signal-to-noise ratio at the output of the doppler filter bank

$\zeta \triangleq \dfrac{\Delta f_d}{B_F}$ = ratio of the doppler offset from the center of two adjacent filters to the one-sided noise bandwidth of the filters ($B_F$)

N = number of pulses being added coherently (N = 16).

The value of $B_F$ is given by [2]:

$$B_F = \begin{cases} 186 \text{ Hz} & R \geq 9.5 \text{ nmi} \\ 437 \text{ Hz} & R < 9.5 \text{ nmi} \end{cases}$$

Figure 40 illustrates the variation of E(z) as a function of $\zeta$ with SNR as a parameter. Since the SNR is not known, a given value of E(z) does not result in a single value for $\zeta$ because the mapping is not one-to-one, which gives rise to the range rate logarithmic discriminant error. In any implementation, a given one-to-one mapping has to be established. The error can then be found as a function of the signal-to-noise ratio. The maximum error found in the expected range of operating signal-to-noise ratios can then be used as a bound for this error. Two methods will be presented here. The first is being implemented by Hughes Aircraft Corporation, and the second is included as an alternative. The simulation has two parts: The first is to find the value of $\Delta f_d$ given a certain range rate $v_d$, and the second is to find the error using a given method of implementation.

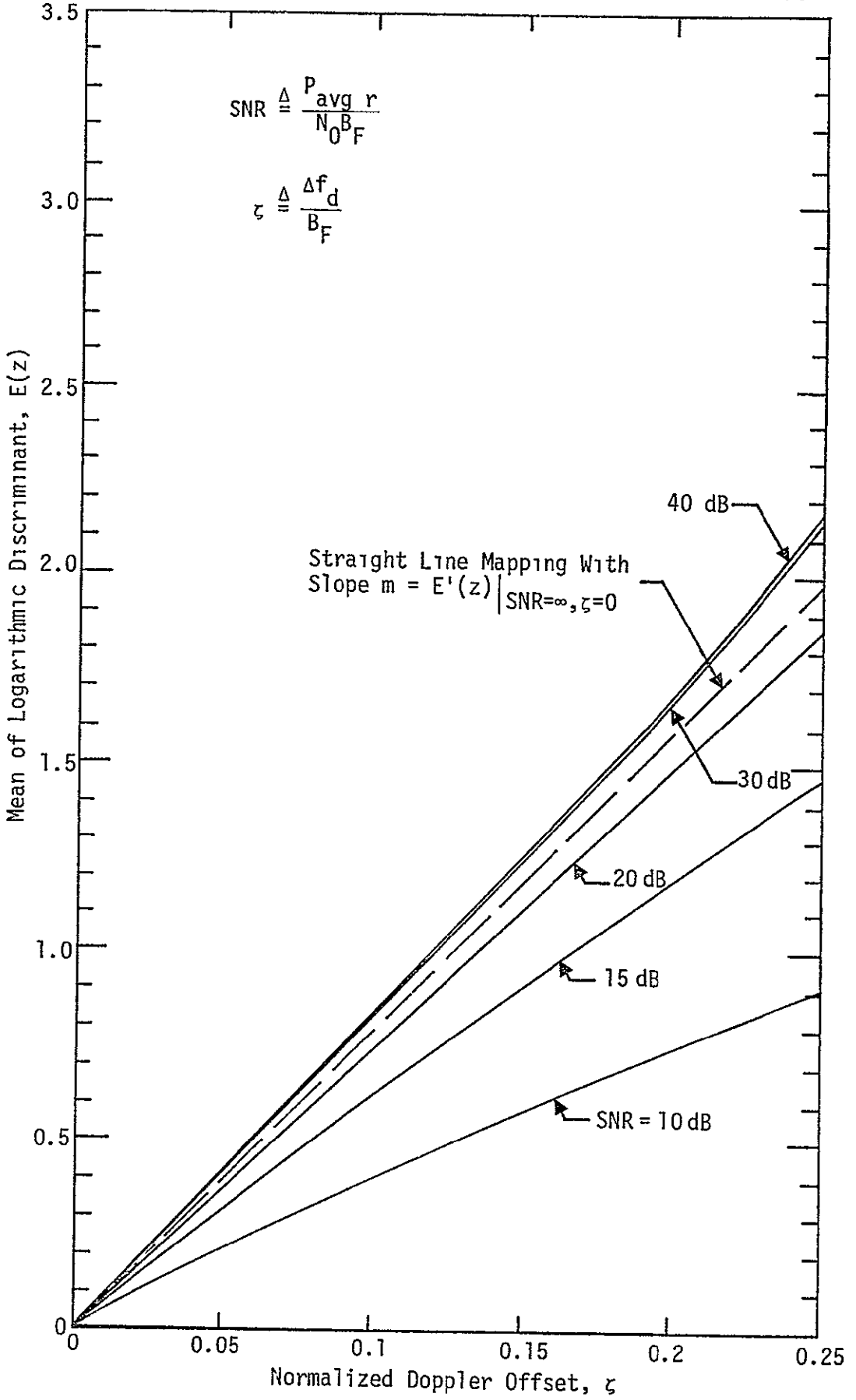


Figure 40. The Mean of the Logarithmic Discriminant Output Versus Normalized Doppler Offset

4.3 1 Finding the Doppler Offset $\Delta f_d$

Since the doppler filters remain fixed in the tracking mode with a spacing of $(B_F/2)$ Hz apart, the doppler reading is obtained using the filter whose center frequency is closest to the actual doppler. The two adjacent filter readings are used as inputs to the logarithmic discriminant. Figure 41 illustrates the location of the 32 filters. The number between two adjacent dotted lines represents the filter which is used for doppler measurement when the actual doppler lies between the two lines. To obtain the doppler offset $\Delta f_d$, we assume that the velocity (range rate) $\dot{R}$ is positive; the actual doppler is then equal to

$$f_d = \frac{2\dot{R}}{c} f_c \tag{69}$$

where $f_c$ is the RF frequency and c is the velocity of light in free space. For $\dot{R}$ in ft/sec,

$$f_d = \frac{2(13.885)\,10^9}{9.83569 \times 10^8} \dot{R} = 28.2\,\dot{R}\ (\text{Hz})$$



We select the filter n to be such that

$$\frac{(2n-1)\,B_F}{2} \le f_d \le \frac{(2n+1)\,B_F}{2}, \quad n = 1,32\ . \tag{70}$$

If $n_1$ is the particular n satisfying (70), then

$$\Delta f_d = \left| \frac{n_1 B_F}{2} - f_d \right| \tag{71}$$

This value of $\Delta f_d$ is used to calculate $\zeta = \Delta f_d / B_F$ There are several points to observe:

(1) $\zeta$ is a positive number which is less than 1/4.

(2) The absolute value used in (71) is due to the symmetry of the problem.

(3) For negative range rates, the absolute value of the velocity is used in the calculations resulting in the number $n_1$. Since the filters are arranged in a circular configuration, the filter $(32 - n_1)$ is used instead of $n_1$ to obtain $\Delta f_d$ in (71).

(4) The filter numbers 32 and 0 represent the same filter.

| R (nmi) | >9.5 | <9.5 |
|---|---|---|
| PRF (Hz) | 2987 | 6970 |
| $B_F$ (Hz) | 186 | 437 |

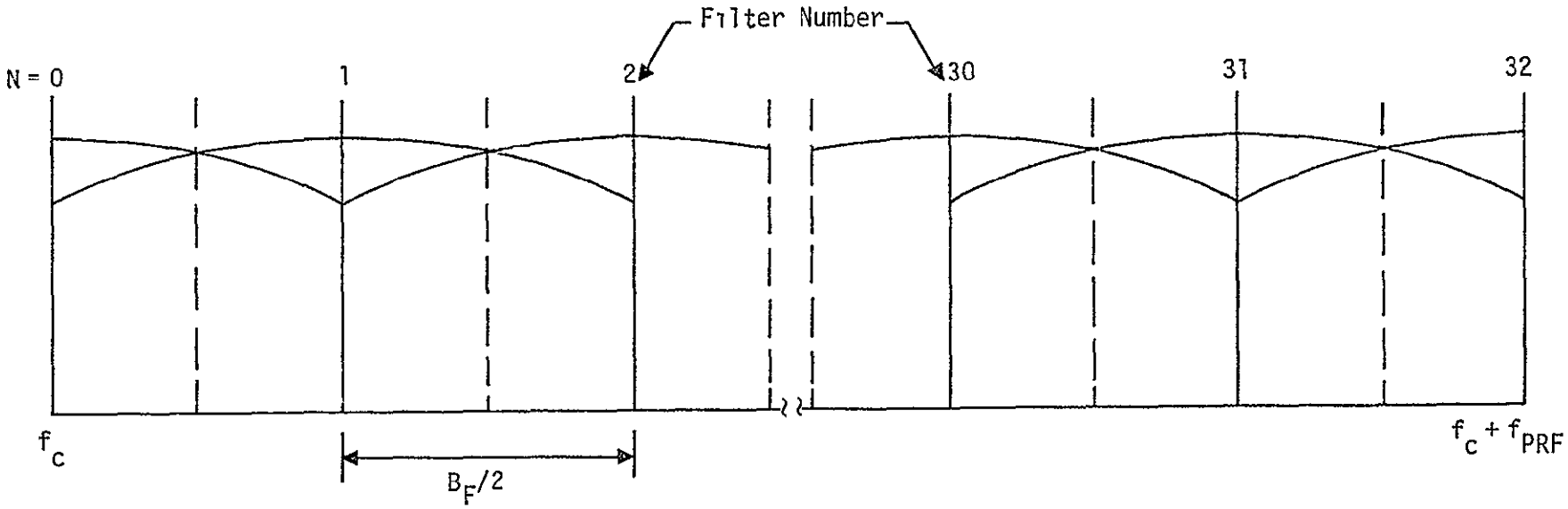


Figure 41. Doppler Filter Configuration in Track Mode

4.3.2 Methods for Finding the Error

Assuming that a one-to-one mapping between E(z) and $\zeta$ exists, then for a given reading E(z), a value $\zeta_1$ can be found using that mapping. The range rate logarithmic discriminant error then becomes

$$\Delta\dot{R}_{LD} = (\zeta - \zeta_1) B_F/28.2 \quad \text{ft/sec}. \tag{72}$$

Finding $\zeta_1$ depends on the particular mapping. Two such mappings are considered.

(1) HAC Mapping

This is the actual mapping being implemented by Hughes. A straight line with a slope equal to that of E(z) at $\zeta = 0$ with SNR = $\infty$ is used to obtain $\zeta_1$. This is the straight line mapping as shown in Figure 40 The slope (m) of the line can be found from (68) to be

$$m = \frac{\pi}{4} \cot\left(\frac{\pi}{32}\right). \tag{73}$$

The resulting range rate logarithmic discriminant error is shown in Figure 42 along with HAC values for comparison purposes.

(2) Infinite Signal-to-Noise Ratio Mapping

Since the ranges of primary interest are close ranges, E(z) at SNR = $\infty$ can be used as a reference (mapping). The value of $\zeta_1$ can be found from (68) by equating SNR to infinity, resulting in

$$\zeta_1 = \frac{1}{2}\left[\frac{2e^{E(z)/2}}{1 + e^{E(z)}} - 1\right]. \tag{74}$$

The actual error at a given SNR can be found using (72). More accurate methods can be suggested to minimize the range rate log discriminant error. All of these methods, however, require major design modifications, which are neither warranted nor recommended at this stage.

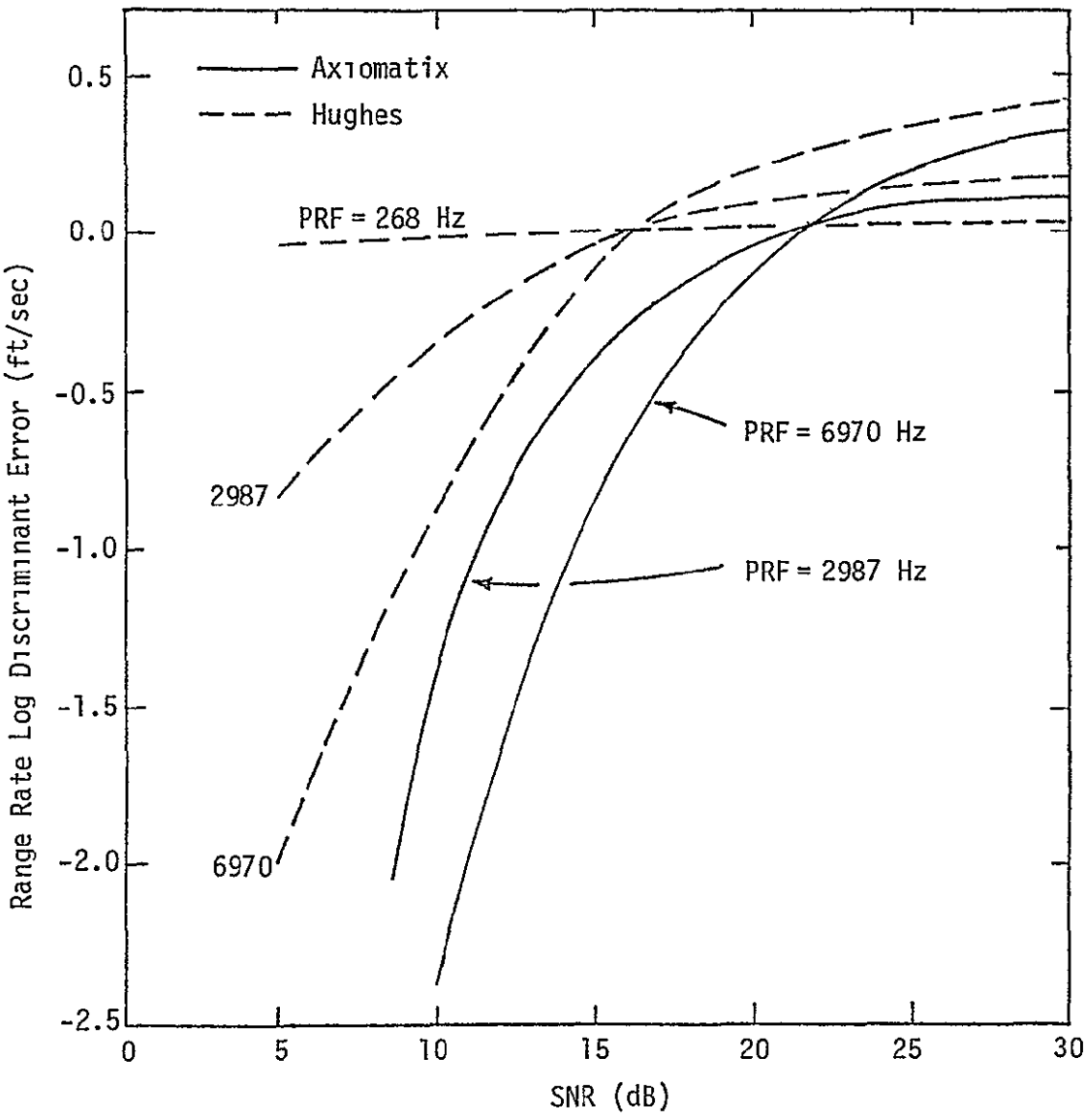


Figure 42. Range Rate Log Discriminant Error, Using HAC Method

## 4.4 Simulation of Target Effects

Models are given in this section to take into account the fact that a true radar target is not a point target. Various models have been prepared in the past, but the simplest and possibly the most effective are those described by Barton [11-12]. Variations of those models are described and recommended for the Ku-band radar simulation. The target effects on each of the tracking loops are considered individually. In each case, an analog computer model is given which involves broadband noise being passed through a first-order filter. The model using a digital recursive algorithm is presented in Appendix A of this report and applies directly to each case presented here.

### 4.4.1 Target Effects on Range Errors

A block diagram of the analog model which represents target effects on range errors is given in Figure 43. The output $\Delta R_T(t)$ is the range error induced by the target, causing time scintillation of the transmitted pulse. The total power or, equivalently, the standard deviation of this error is approximated as

$$\sigma_{\Delta R_T} = a_r L_r \tag{75}$$

where the units of $\sigma_{\Delta R_T}$ are the same as $L_r$ (feet or meters) and $a_r$ is a proportionality constant in the range

$$0.2 \leq a_r \leq 0.5 \ . \tag{76}$$

This says that the standard deviation of range errors due to target effects is 20% to 50% of $L_r$, where $L_r$ is the effective target dimension along the LOS. This is a value which must be approximated and can also be time varying.

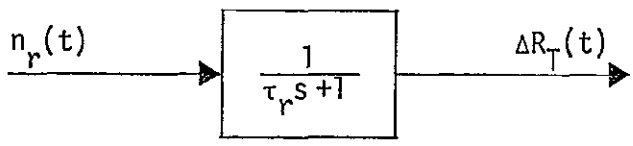


Figure 43 Analog Model of Target Effects on Range Errors

A simple and satisfactory model of the target (in a plane) is a rectangle with minimum dimension $L_{min}$ and maximum dimension $L_{max}$. We assume the target is rotating in the plane created by the LOS by an amount $\omega_r$ radians/sec. Then the effective target distances along and perpendicular to the LOS are

$$L_r(t) = L_0[1 + \gamma \cos(\omega_r t)] \tag{77a}$$

and

$$L_x(t) = L_0[1 + \gamma \sin(\omega_r t)] , \tag{77b}$$

respectively, where

$$L_0 \triangleq \frac{L_{max} + L_{min}}{2} \tag{78a}$$

and

$$\gamma \triangleq \frac{L_{max} - L_{min}}{L_{max} + L_{min}} . \tag{78b}$$

In this model (shown in Figure 44), it is assumed that the rotation is small compared to the reciprocal of the tracking loop bandwidths. This is certainly the case with any target for which there is expected rendezvous and docking. As a result, $L_r(t)$ and $L_x(t)$ need not be updated every T sec (computer update time) and could be updated every 10 T to 20 T.

The time constant $\tau_r$ of the target along the LOS in Figure 43 is given by

$$\tau_r = \frac{\lambda}{4\omega_r L_r} , \tag{79}$$

where $\lambda$ is the wavelength. If the target's relative rotation with respect to the LOS is identically zero, then this time constant goes to infinity, and the range error due to target effects is a constant bias error. For this time constant and the standard deviation in (75), the one-sided power spectral density (PSD), $W_r$, of the broadband noise $n_r(t)$ is given by

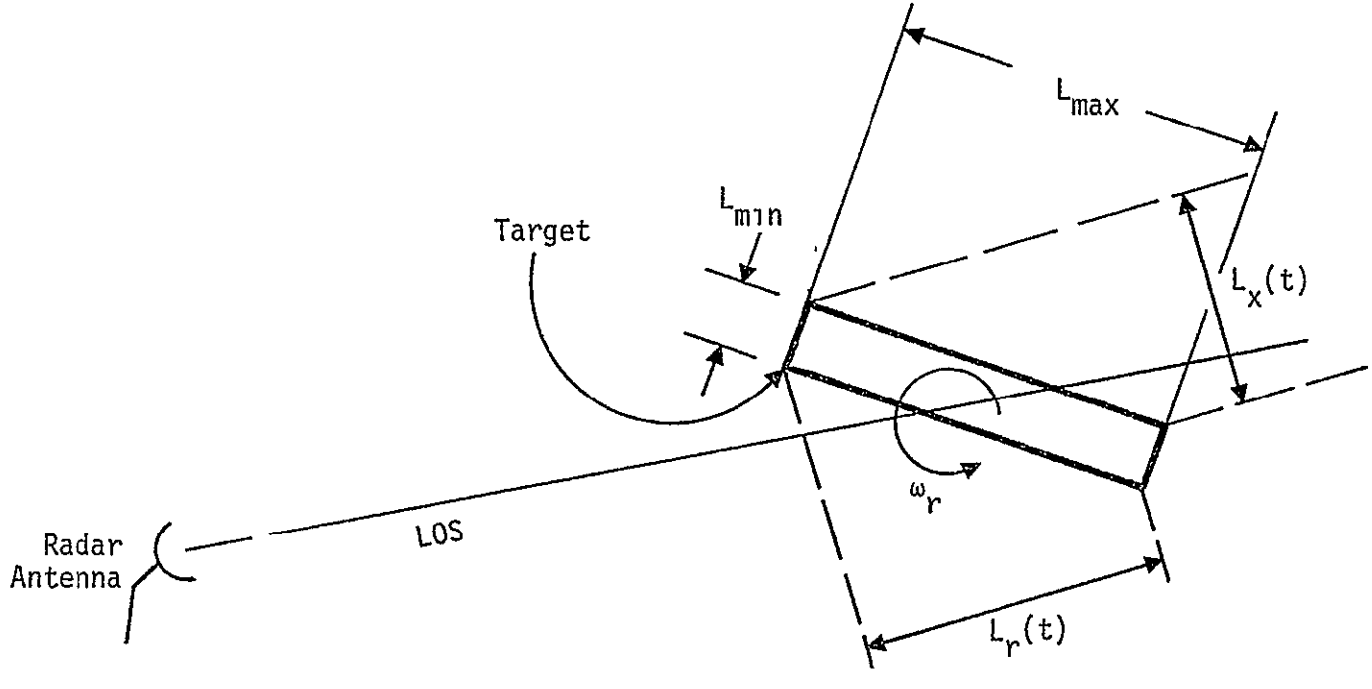


Figure 44. Description of Rotating Target Dimensions

$$W_r = \frac{a_r^2 L_r \lambda}{\omega_a} \text{ (units of distance)}^2 \text{ sec} . \quad (80)$$

A block diagram of the computations necessary for this simulation of target effects in range is shown in Figure 45 The stochastic differential equation for $\Delta R_T(t)$ is

$$\Delta \dot{R}_T(t) = \left(\frac{-1}{\tau_r}\right) \Delta R_T(t) + \left(\frac{1}{\tau_r}\right) n_r(t) . \quad (81)$$

To convert this to a discrete time digital simulation, follow the procedure at the end of Appendix A of this report. In Figure 45, the factor $1/\sqrt{5}$ accounts for the improvement on the target effect errors which results from frequency diversity.

4.4.2 Target Effects on Range Rate Errors

A block diagram of the model of target effects on range rate errors is shown in Figure 46. The standard deviation of the error is approximated by

$$\sigma_f = \frac{2 a_v L_x \omega_r}{\lambda} \text{ Hz} , \quad (82)$$

where $a_v$ is a proportionality constant which, for most targets, is within the interval

$$0.2 \leq a_v \leq 0.4 . \quad (83)$$

In terms of range rate, the standard deviation is

$$\sigma_v = a_v L_x \omega_r \text{ (units of distance)/sec} . \quad (84)$$

The time constant of the target effects on range rate, $\tau_v$, is approximately equal to

$$\tau_v = \frac{\lambda}{4 \omega_r L_x} \text{ sec} , \quad (85)$$

where $\omega_r$ is the same rotation rate of the previous section in rad/sec. If $\omega_r \equiv 0$, there are no target effects on range rate.

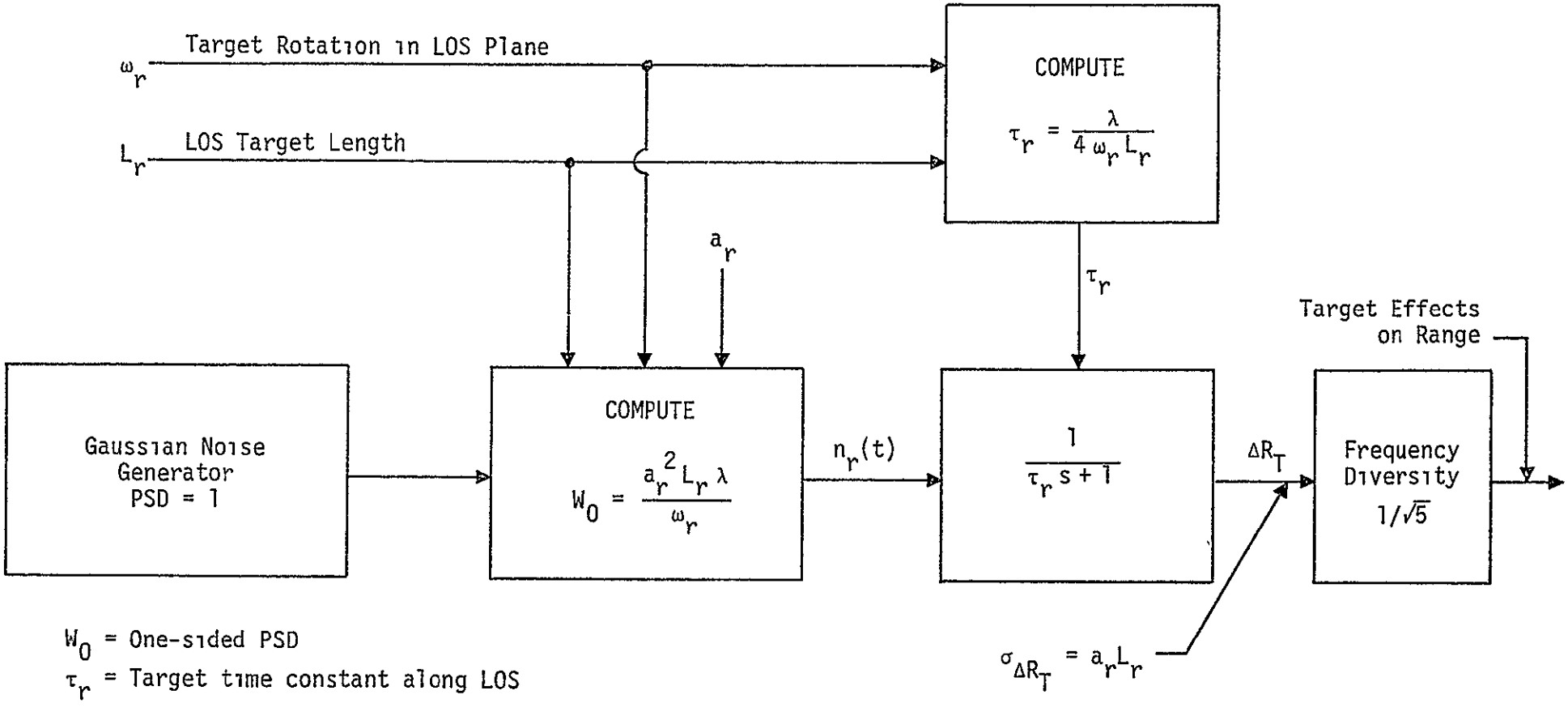


Figure 45. Simulation of Target Effects in Range

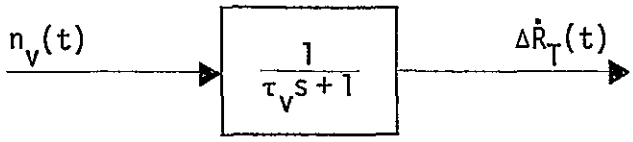


Figure 46. Analog Model of Target Effects on Range Rate Errors

For the standard deviation given in (84) and the time constant in (85), the one-sided PSD of the noise $n_v(t)$ is

$$W_v = a_v^2 L_x \lambda \omega_r \quad \text{(units of distance)}^2/\text{sec} . \tag{86}$$

The block diagram which depicts the computation necessary to simulate the target effects on range rate is given in Figure 47. The effect of frequency diversity (a factor of 5 improvement in variance) is also shown.

The stochastic differential equation for $\Delta\dot{R}_T(t)$ is

$$\frac{d(\Delta\dot{R}_T(t))}{dt} = \left(\frac{-1}{\tau_v}\right) \Delta\dot{R}_T(t) + \left(\frac{1}{\tau_v}\right) n_v(t) , \tag{87}$$

which can be simulated digitally via Appendix A.

An example calculation of the standard deviation is:

Example: $a_v = 0.35$

$L_x = 30$ ft

$\omega_r = 2$ deg/sec

$\sigma_{\Delta\dot{R}_T}$ { = 0.37 ft/sec (without frequency diversity)
= 0.17 ft/sec (with frequency diversity)

Note that the target effects on both range and range rate are independent of the true range. It will be seen that this is not the case with the angle and angle rate estimates.

### 4.4.3 Target Effects on the Angle Tracking Loop

The target effects on the angle tracking loop are similar to those of range and range rate presented above with the exception that the effect depends on the range to the target. The block diagram is shown in Figure 48. The standard deviation of the angle error due to

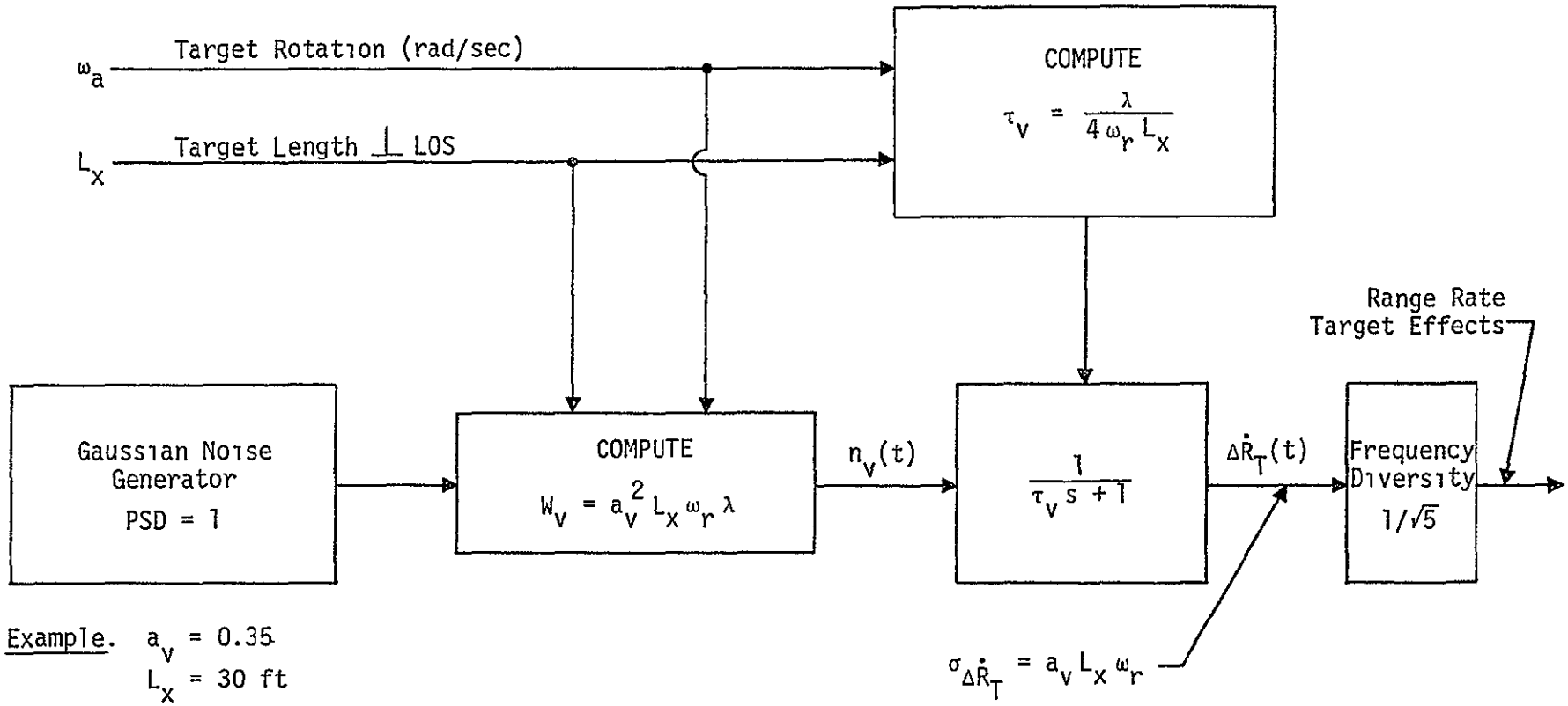


Example. $a_V = 0.35$
$L_X = 30$ ft
$\omega_r = 2$ deg/sec
$\sigma_{\Delta\dot{R}} = 0.37$ ft/sec (0.17 ft/sec with frequency diversity)

Figure 47. Simulation - Target Effects in Range Rate

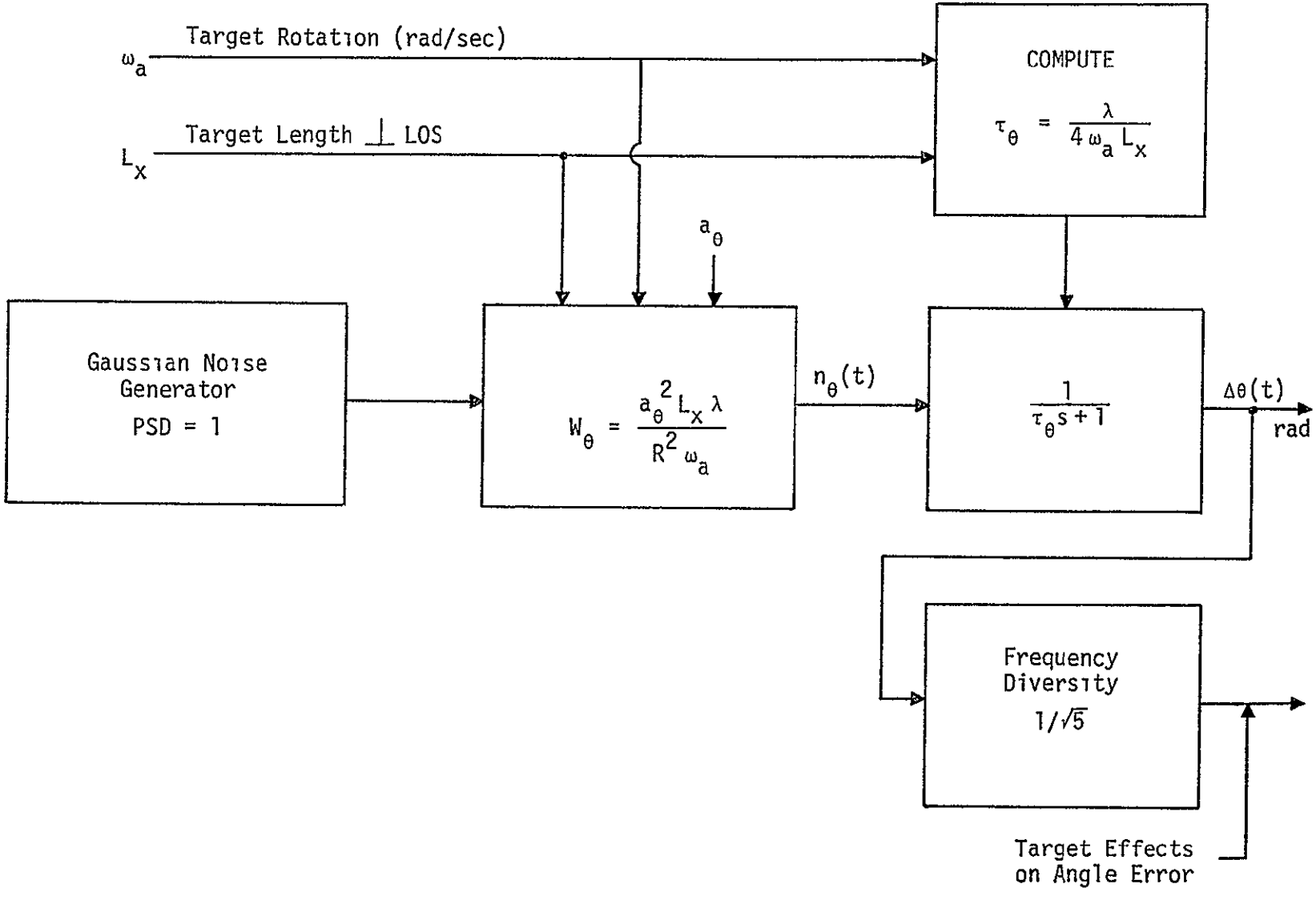


Figure 48. Angle Errors Due to Target Effects

target effects is approximated by

$$\sigma_{\Delta\theta} = \frac{a_\theta L_x}{R} \text{ radians}, \tag{88}$$

where the proportionally constant $a_\theta$ is also in the range

$$0.2 \leq a_\theta \leq 0.4 \tag{89}$$

and $L_x$ and R are in the same units. The time constant $\tau_\theta$ of the analog model is equal to

$$\tau_\theta = \frac{\lambda}{4\omega_a L_x} \text{ sec}, \tag{90}$$

where $\omega_a$ (in rad/sec) is angular rotation in the plane perpendicular to the LOS. The corresponding PSD, $W_\theta$, of the broadband noise $n_\theta(t)$ is

$$W_\theta = \frac{a_\theta^2 L_x \lambda}{R^2 \omega_a} \text{ sec}. \tag{91}$$

The necessary computations are shown in Figure 48. The stochastic differential equation for $\Delta\theta(t)$ is

$$\frac{d\Delta\theta(t)}{dt} = \left(\frac{-1}{\tau_\theta}\right) \Delta\theta(t) + \left(\frac{1}{\tau_\theta}\right) n_\theta(t), \tag{92}$$

which is simulated, as are the others, via Appendix A.

The standard deviation in (88) is plotted in Figure 49 for cases that are expected on the Orbiter. It is seen that the target effects can be expected to cause the angle error to be over the specification value at relatively large ranges For the values chosen, the range at which the antenna field of view is 10% and 100% filled is indicated on Figure 49 using the computation described in Figure 50.

The results indicate that reliable angle tracking information cannot be expected at ranges above several thousand feet when $L_x = 60$ ft. A rule of thumb is that, when the antenna beam is filled by more than 10%, angle tracking difficulties should be expected. In the case of the Orbiter, however, this percentage can be increased somewhat because of the slow rotation rates that are anticipated. The solution to this problem is described in the introduction of this report.

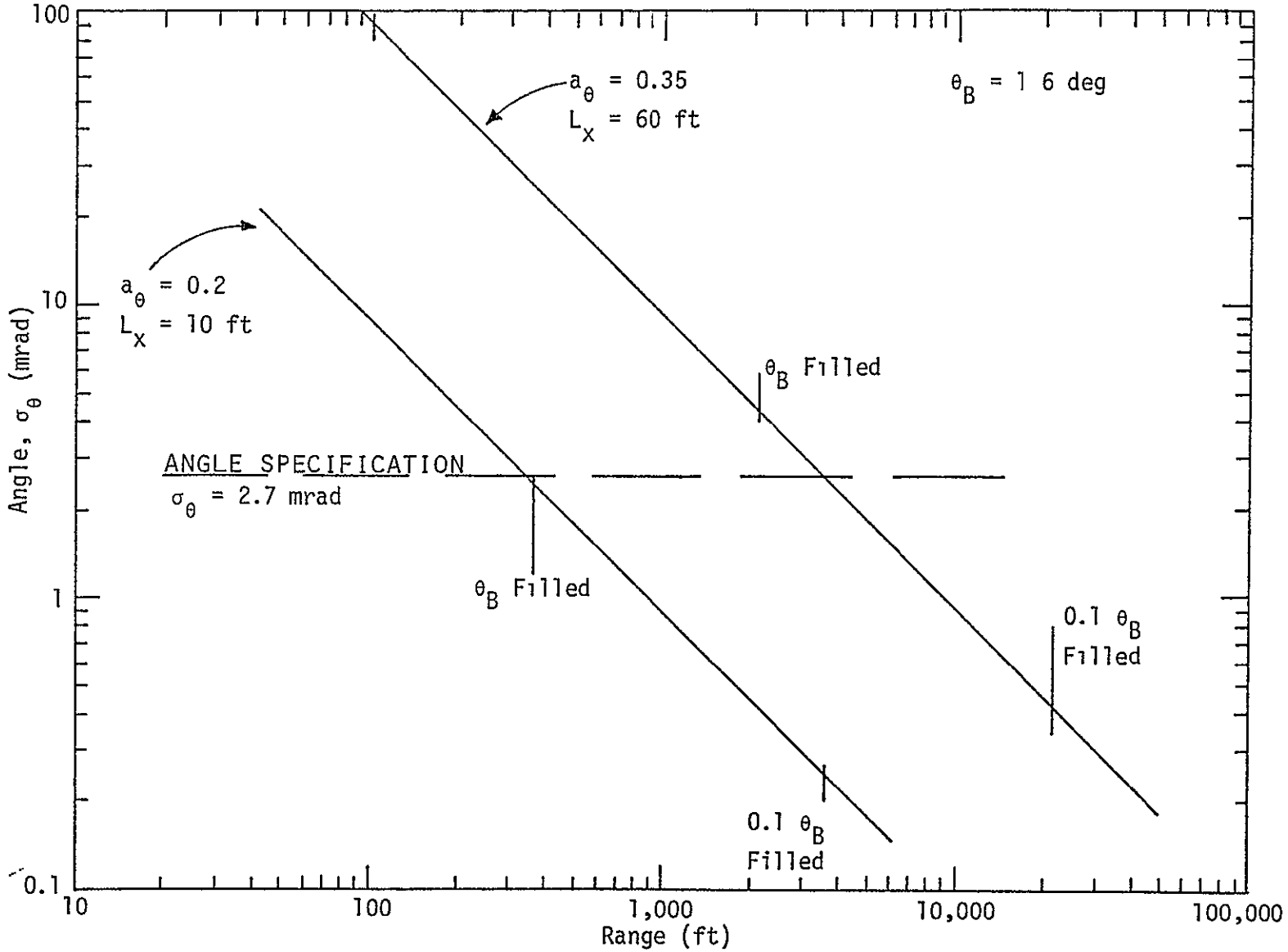


Figure 49. Angle Errors Due to Target Effects

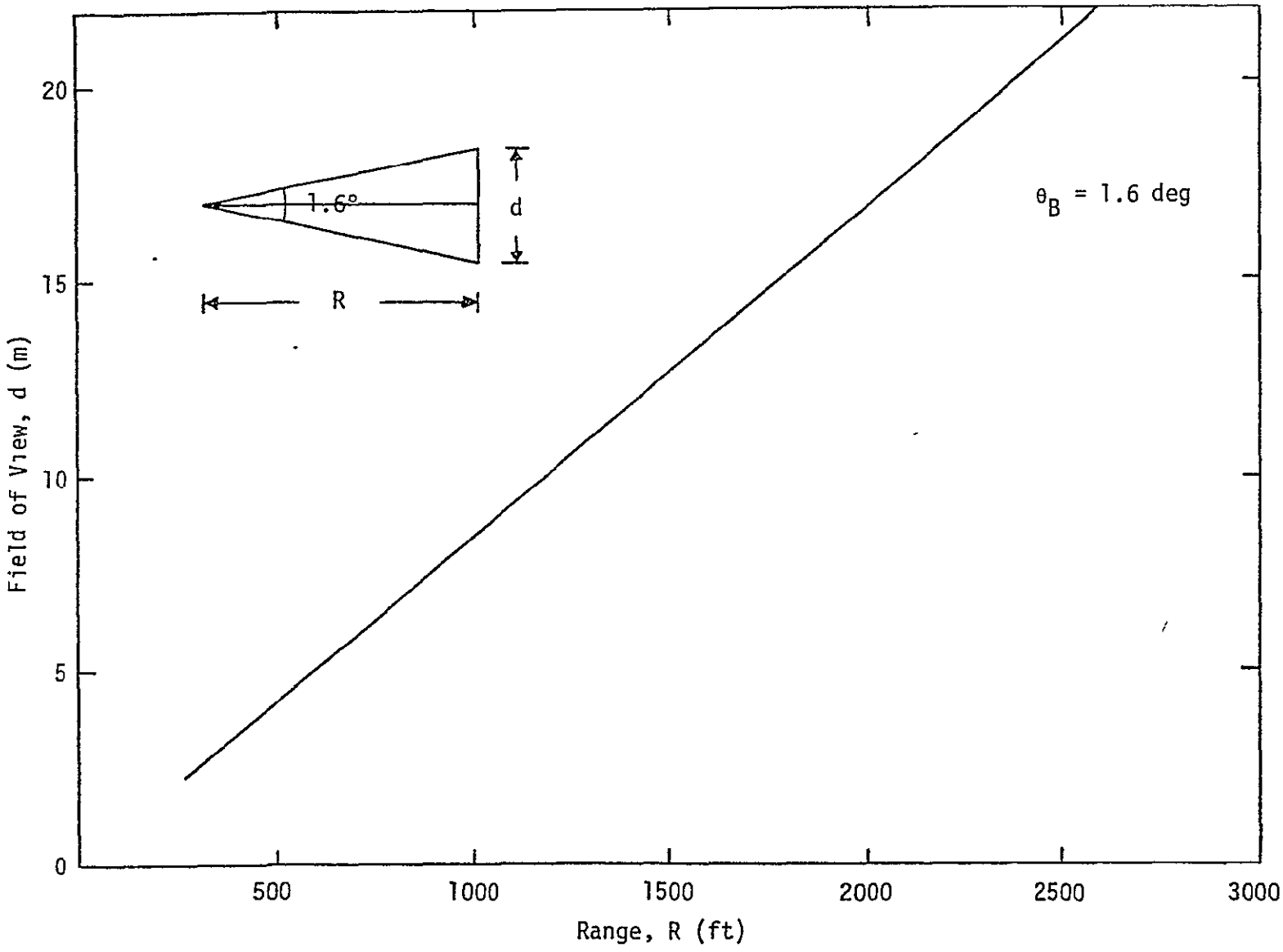


Figure 50. Range at Which the Antenna Field of View is Filled

### 4.4.4 Target Effects on Angle Rate Estimation

The angle rate error caused by target effects is best estimated from the development in [1, Appendix D], wherein the rates of the standard deviations are given by

$$\frac{\sigma_{\dot{\theta}}}{\sigma_{\theta}} = \frac{2\pi f_n}{\sqrt{4\zeta^2+1}} \ (\text{sec})^{-1}, \tag{93}$$

where $f_n$ = natural frequency of the angle tracking loop
$\zeta$ = damping factor of the angle tracking loop.

This can also be written as

$$\sigma_{\dot{\theta}} = \left[\frac{2\pi f_n}{\sqrt{(2\tau)^2(\pi f_n)^2+1}}\right]\sigma_{\theta}, \tag{94}$$

where $\tau$ is the time constant of the angle tracking loop. For R < 1.9 nmi, the present system parameters [2] are

$$\begin{aligned} 2\tau &= 5.4 \text{ sec} \\ f_n &= 0\ 12 \text{ Hz}, \end{aligned} \tag{95}$$

for which the term in brackets in (94) is equal to 0.332 $(\text{sec})^{-1}$.

Since the angle rate estimate is derived directly from the angle tracking loop (see [1, Appendix D] or section 4.1 of this report), the target effects for angle rate will have the same power and time constants as employed for the angle tracking loop. Angle rate errors can be determined directly from angle errors as shown in Figure 51.

Sample computations of the angle rate error are shown in Figure 52, where it is noted that the specification value on standard deviation is not attained below several thousand feet for most target sizes.

An alternative solution to this difficulty has been proposed and is described in the introduction of this report.

## 4.5 Overall Description of Ku-Band Radar Simulation

In the previous parts of this section, the necessary components of the Ku-band radar simulation were presented. In this section, the components are assembled and certain additional errors are taken into account.

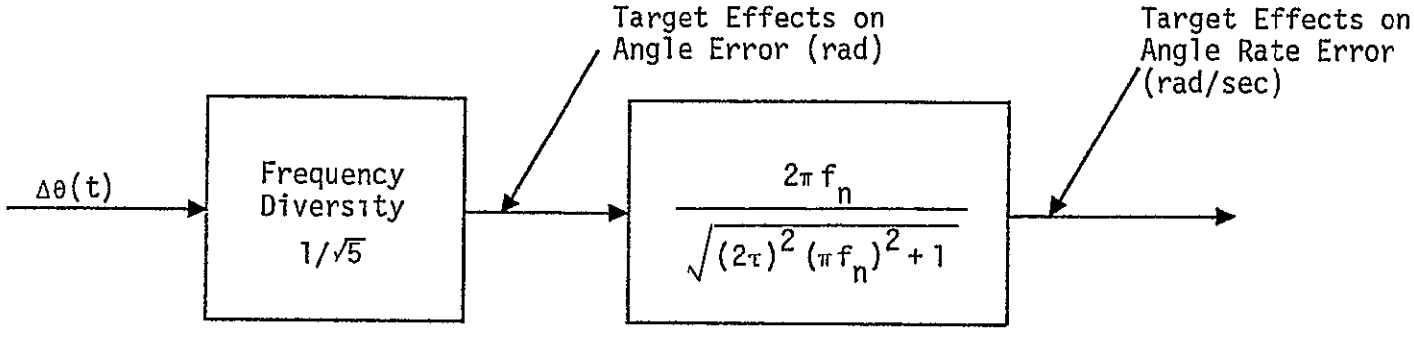


Figure 51. Angle Rate Errors From Angle Errors Due to Target Effects

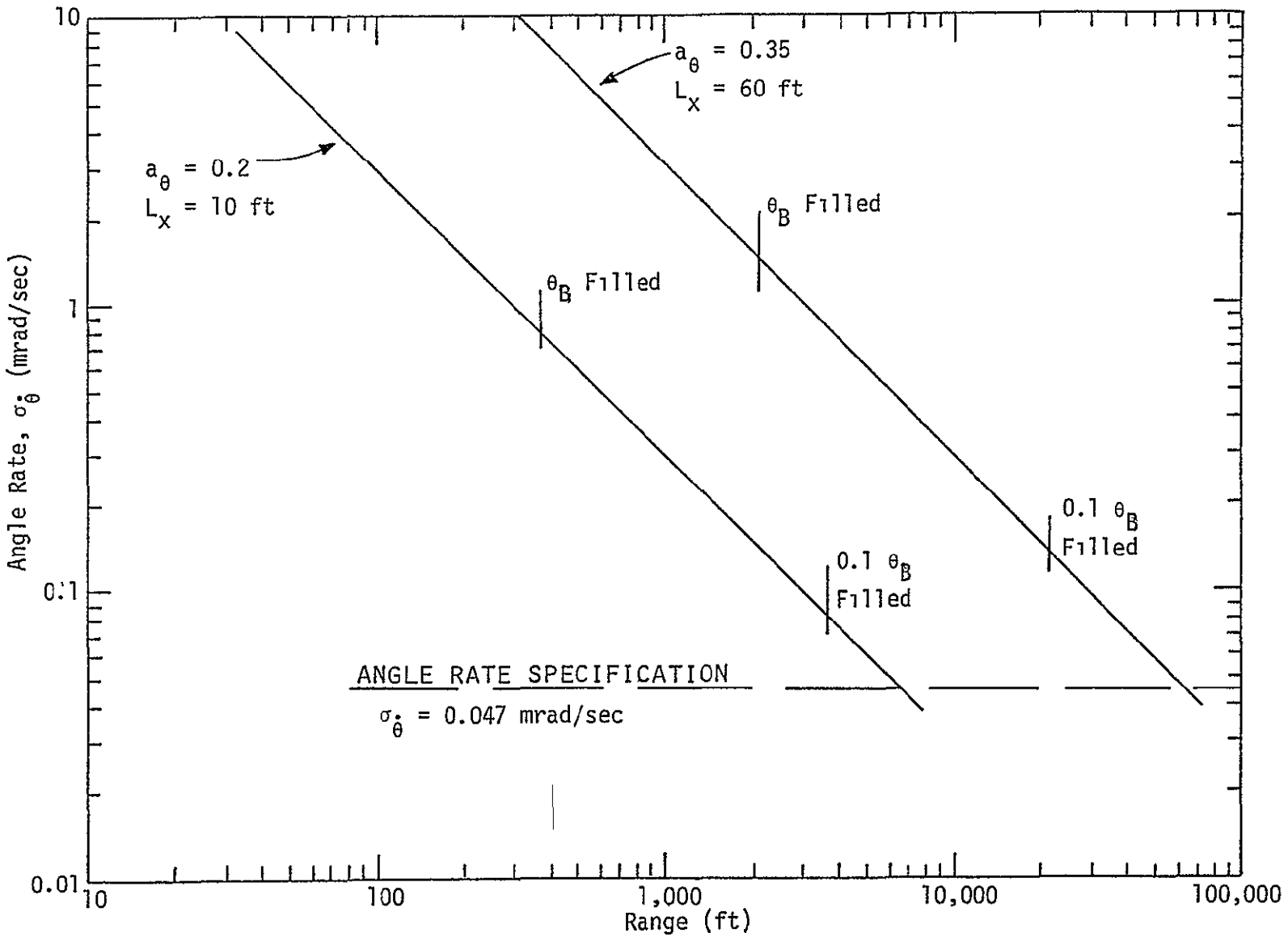


Figure 52. Angle Rate Errors Due to Target Effects

4.5.1 Range Error Simulation

The range error simulation block diagram is given in Figure 53. The target effects, thermal noise and amplitude scintillation errors, and acceleration errors have been previously diagrammed. The component bias is a range error which results from time delay variations of the RF signal through the various components in the front end of the radar. These variations are due to temperature, aging, and the like. The maximum value of these components [2] has been estimated as

$$L = |\pm 28'|_{\max} \quad \text{for} \quad R < 2500'$$

$$L = |\pm 77'|_{\max} \quad \text{for} \quad R > 2500'. \tag{96}$$

The variation is very slow. Therefore, we propose to model the component bias as a random variable, either Gaussian or uniform. In the Gaussian case, set $3\sigma = L$, with L given in (96). In the uniform case, the probability density function extends from (-L,L), and the variance is $\sigma = L/\sqrt{3}$.

A second additional error component of range error is due to data staleness. Using the update times of the computer involved with the Ku-band radar, a stochastic model can be developed similar to those used in the target effects simulation. A simpler alternative is to periodically use a sample of a Gaussian noise generator whose $3\sigma$ value is equal to 1/2 the maximum data staleness value and whose mean has the same value. This is depicted in Figure 54, where M corresponds to the maximum data staleness time.

A sample computation of range errors in the proximity operations region is shown in Table 9. It is seen that, at short ranges, the component bias and target effects constitute the major part of the range error. The acceleration effects are small, and the effects of data staleness were not taken into account in the computations of Table 9.

4 5.2 Range Rate Error Simulation

A general block diagram of the range rate error simulation is shown in Figure 55. All contributions to the range rate error have been presented in the previous sections A sample computation is shown in Table 10. The maximum range rate error due to the logarithmic discriminant error would occur only at lower signal-to-noise ratios. At

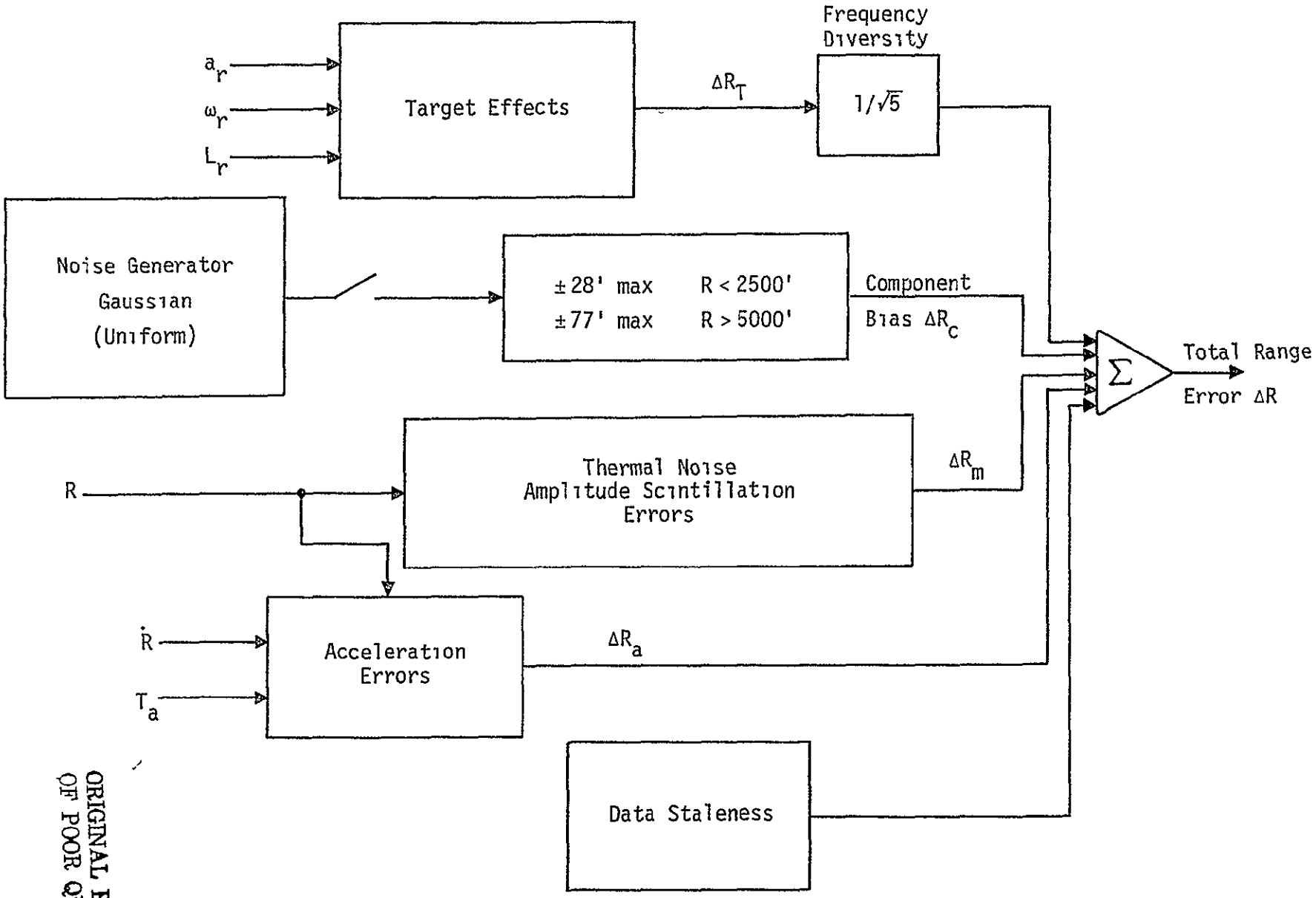


Figure 53. Range Error Simulation

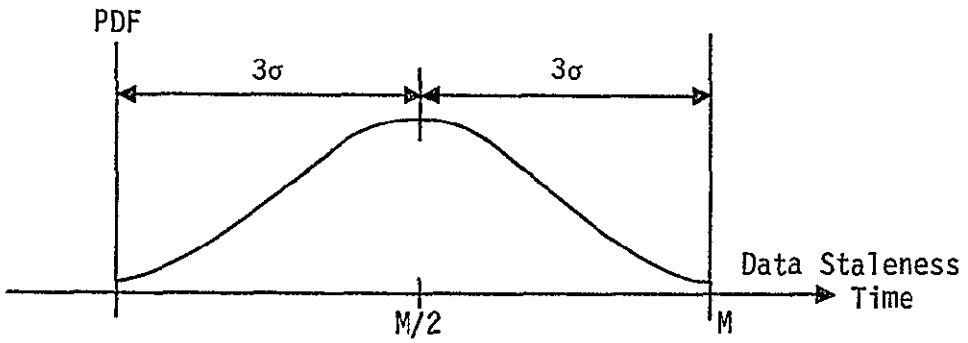


Figure 54. PDF for Data Staleness Model

Table 9. Typical Case of Proximity Operations Range Errors

| | | |
|---|---|---|
| 1. | Thermal Noise | $\sigma \approx 0.1$ ft |
| 2. | Target Effects | $\sigma = a_r L_r$ ft |
| 3. | Component Bias | $\sigma = 28/3$ ft (Gaussian)<br>$= 28/\sqrt{3}$ ft (Uniform) |
| 4. | Error from Acceleration $\dot{R}$ | Small |
| 5. | Data Staleness | Gaussian Random Variable |
| Example: | $a_r = 0.3$<br>$L_r = 30$ ft | $\sigma_{total} = 18.4$ ft (Gaussian<br>$= 25.3$ ft (Uniform) |

Table 10. Proximity Operations Range Rate Errors

| | | |
|---|---|---|
| 1. | Thermal Noise | $\sigma < 0.1$ ft/sec |
| 2. | Target Effects (Example in Section 4 5.2) | $\sigma \approx 0.17$ ft/sec |
| 3. | Ln Discriminant Error | Max 0.4 ft/sec |
| 4. | Acceleration Effects | Negligible |
| | | $\sigma_{total} \approx 0.5$ ft/sec |

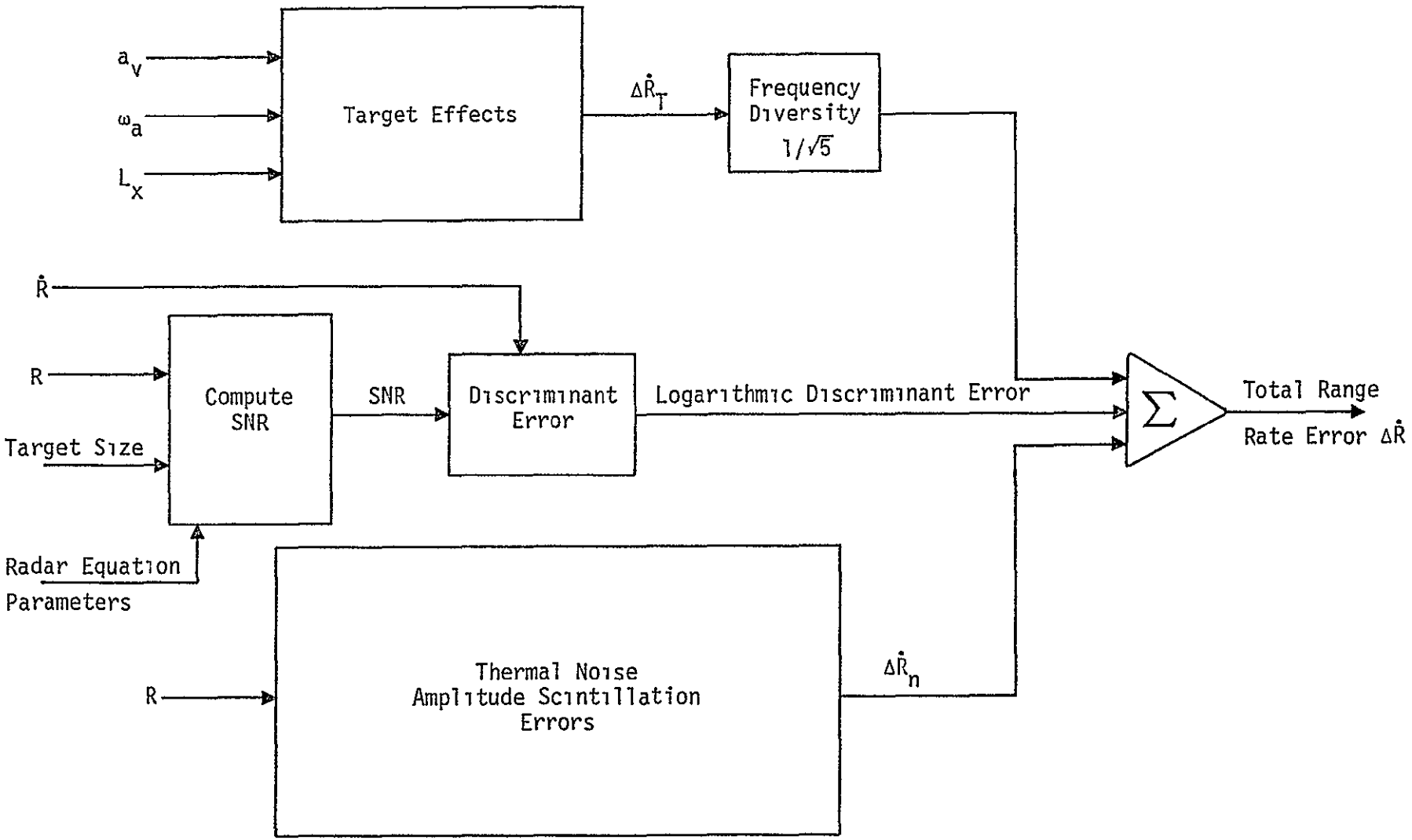


Figure 55. Range Rate Error Simulation

close ranges, the SNR will be quite high, so that the logarithmic discriminant error will be much less than the maximum indicated in Table 10. In the absence of significant target rotation, the Ku-band radar can be expected to provide satisfactory range rate data down to a few hundred feet.

4.5.3 Angle and Angle Rate Error Simulation

The general block diagram of the angle and angle rate error simulation appears in Figure 56. All contributions to these errors have been discussed in previous sections. The primary contribution at close ranges is the target effects, plots of which are presented in section 4.4.4.

4.5.4 Additional Comments

The acceleration effects and thermal noise effects took into account the transfer function of the Ku-band radar. When the target effects were taken into account, the effects of the transfer function were not included. This would need to be done if the power spectral density of the target effects were wider than those of the radar tracking loop. Since the target rotation is expected to be very small, the bandwidth of the signal will not be more than 0.1 Hz or less. Therefore, target effect errors will be direct errors, and radar filtering will not alter them.

As a final remark, it should be noted that no range gates are used at close range ($R < 0.42$ nmi). Instead of the straddling loss, there is a substantial signal loss due to the two-pole Butterworth filter when the range is short and the pulse width is 0.122 μsec. The response to such a pulse is shown in Figure 57. Since only one sample per pulse is taken at short ranges, the maximum possible power loss is found to be 6.5 dB. This loss should be included in the radar equation when computing the signal-to-noise ratio which is to be used in the simulation computations.

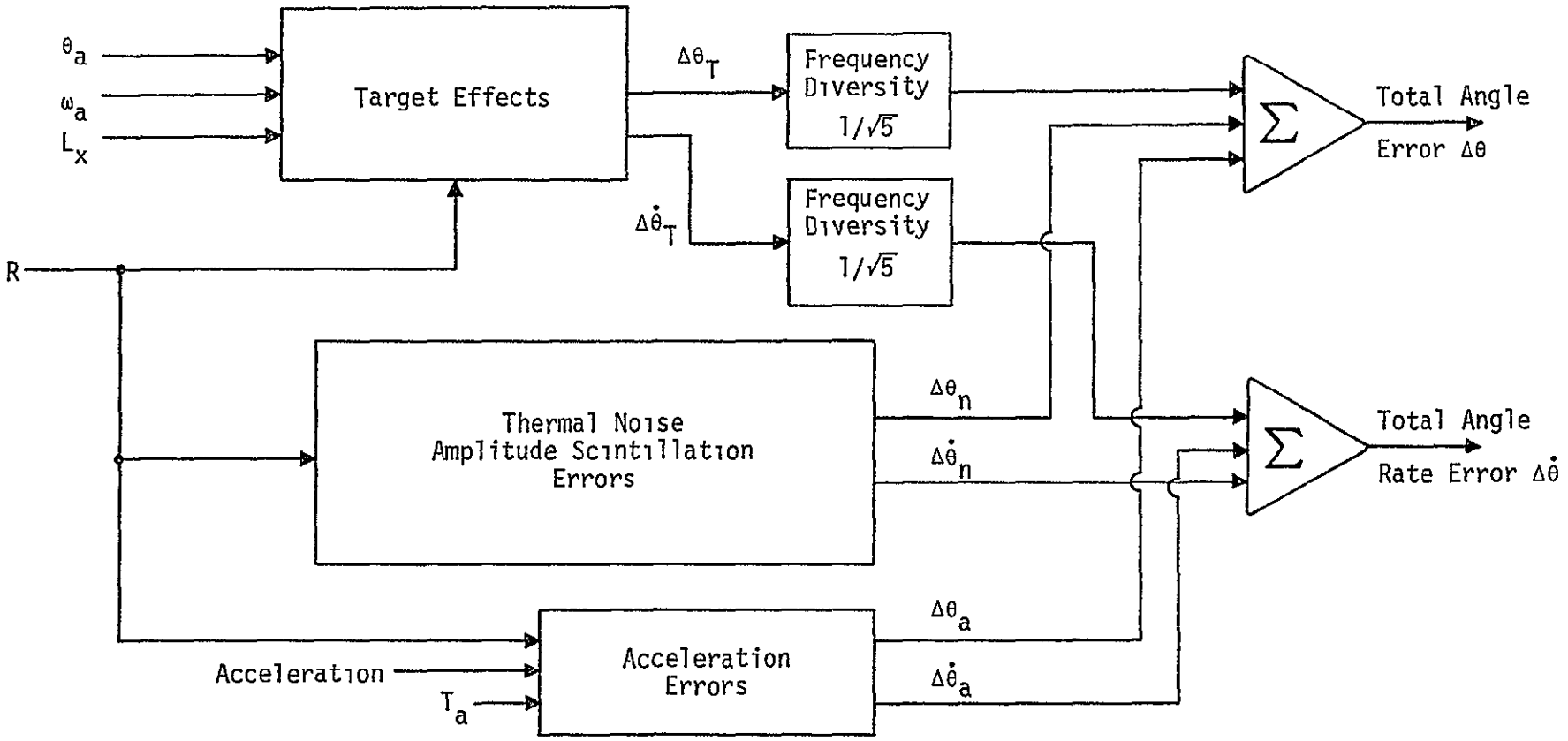


Figure 56. Angle and Angle Rate Error Simulation

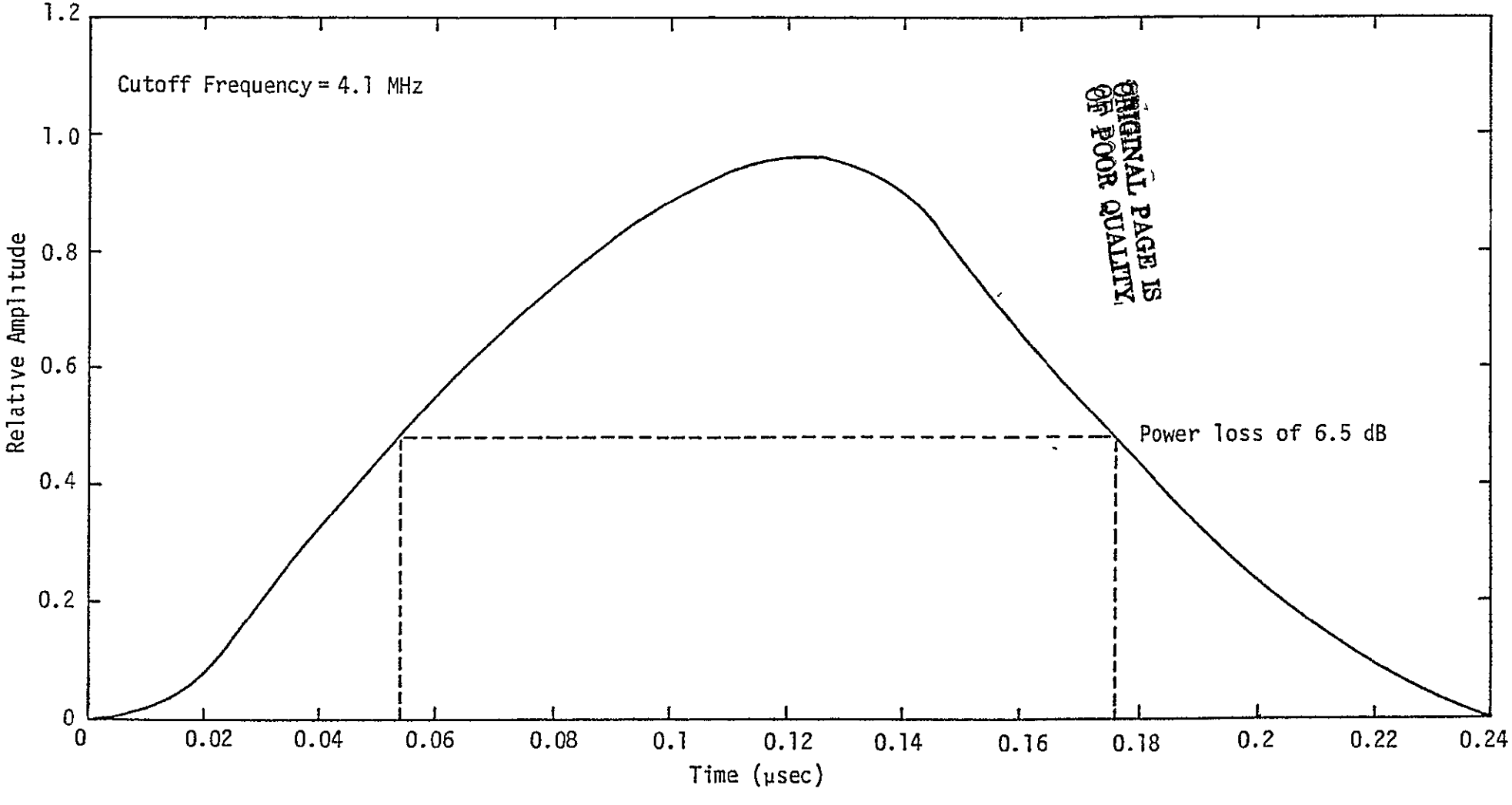




Figure 57. Two-Pole Butterworth Response to a Pulse of 0.122 μsec

## 5.0 ELECTRO-OPTICAL DOCKING TECHNIQUES

This section describes the results of a preliminary tradeoff analysis conducted to identify viable electro-optical (EO) docking techniques to supplement the Ku-band radar at short ranges from approximately 1000 ft down to 25 ft.

Section 5.1 presents an analysis of the geometrical relations involved in the co-planar case, including an error-sensitivity analysis, while Section 5.2 contains a description of the various EO system concepts considered for both cooperative and noncooperative satellites.

The primary device for implementation of these techniques is the laser. Further study and analysis of the proposed methods are needed to confirm the tentative conclusions given here.

### 5.1 Analysis of Ranging Techniques

In this section, the geometrical relationships used to compute the "perpendicular range" from the baseline of the docking station (Orbiter/Shuttle) to the satellite (target) are developed. Two basic methods are defined: (1) triangulation (angle measurement) and (2) range-only measurements. Possible combinations of these are also noted. Various electro-optical concepts utilizing these techniques are described in Section 5.2.

#### 5.1.1 Triangulation

The triangulation method requires two angle trackers situated at the extreme ends of the Shuttle baseline (to maximize range measurement accuracy). If the distance between them is accurately known and the appropriate line-of-sight (LOS) angles to the satellite are measured by the trackers, the perpendicular distance from the baseline to the satellite can be determined by trigonometry When the tracker angles are measured in a coordinate system that is fixed with respect to the Shuttle, the "range triangle" will not, in general, lie in the reference plane Although general, three-dimensional relationships would be employed in the real docking system (i.e., they would be programmed into the docking computer), only the much simpler co-planar case will be considered here, since it suffices for preliminary analysis.

The co-planar case is illustrated in Figure 58, where a and b are legs of the triangle, $\ell$ is the base (baseline), and the angles $\phi_1$ and $\phi_2$ are measured from the normal to the baseline (i e., from the y-axis) as shown. The dashed line R is the perpendicular distance to the satellite and uniquely defines its range from the station.

By straightforward trigonometry, it can be shown that

$$R = \frac{\ell \cos \phi_1 \cos \phi_2}{\sin (\phi_1 + \phi_2)},$$

which involves the two variables $\phi_1$ and $\phi_2$ in addition to the constant $\ell$. To avoid unnecessary complexity, we restrict further consideration to the special case when the satellite is equidistant from the two trackers and approaches along the perpendicular R. Then, $\phi_1 = \phi_2 = \phi$, and

$$R = \frac{\ell \cos^2 \phi}{\sin 2\phi} = \frac{\ell \cos^2 \phi}{2 \sin \phi \cos \phi}$$

$$R(\phi) = D \cot \phi, \tag{97}$$

where $D \triangleq \ell/2$. Equation (97) is seen to be correct by inspection of Figure 59. The notation $R(\phi)$ signifies that R is a function of the measured variable $\phi$.

Error Analysis for R

We are interested in the accuracy of the R determination in terms of the uncertainties in the measurements of $\phi$ and D. To this end, consider the variations $\delta R_\phi$ and $\delta R_D$ resulting from independent variations in $\phi$ and D (or $\ell$), respectively. Thus, from (97) and Figure 59,

$$\delta R_\phi = -D \csc^2 \phi \, \delta\phi = -\frac{D \, \delta\phi}{\sin^2 \phi}$$

$$\delta R_\phi = -\frac{R^2 + D^2}{D} \delta\phi$$

and

$$\delta R_D = \cot \phi \, \delta D$$

$$\delta R_D = \frac{1}{2} \frac{R}{D} \delta\ell.$$

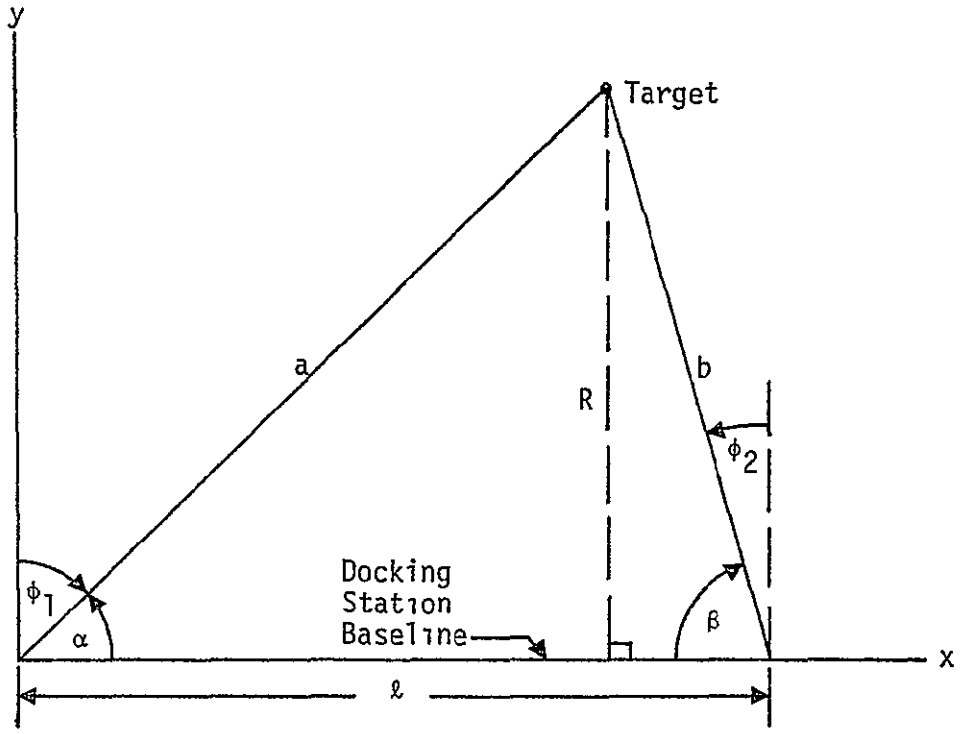


Figure 58. Co-Planar Case of Triangulation

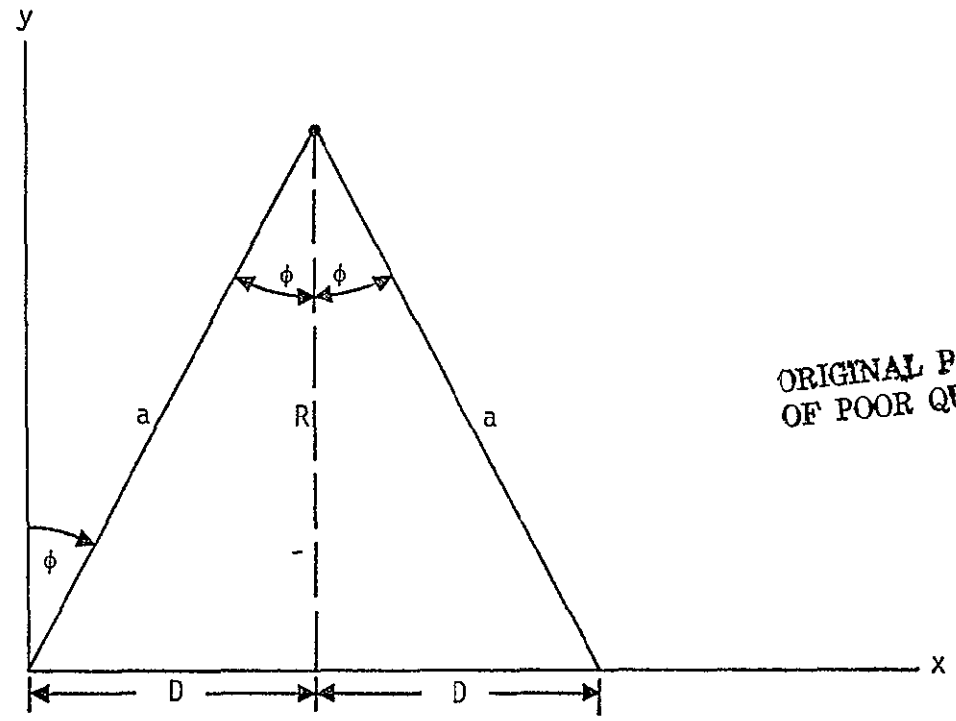




Figure 59. Special Case of Co-Planar Triangulation (b = a)

If $\delta\phi$ and $\delta D$ are regarded as independent random variables, then the rms variation in R is

$$\delta R_{rms} = \sqrt{(\delta R_{\phi})^2 + (\delta R_{\ell})^2}$$

$$\delta R_{rms} = \frac{1}{D}\sqrt{(R^2+D^2)^2(\delta\phi)^2 + R^2(\delta\ell/2)^2}\,. \qquad (98)$$

Hence, it follows that

$$\delta\phi = \frac{\sqrt{D^2(\delta R)_{rms}^2 - R^2(\delta D)^2}}{R^2+D^2}\,. \qquad (99)$$

Thus, $\delta\phi$(rad) is the angle accuracy required to achieve a range precision $(\delta R)_{rms} = 1$ ft at the range R.

Equation (99) is plotted as a function of R in Figure 60 for $D = 30$ ft ($\ell = 60$ ft), $\delta\ell = 0.1$ ft, and $\delta R_{rms} = 0.5$, 1, and 2 ft. These values are typical of those anticipated on the Orbiter. Since the range precision ($\delta R_{rms}$) is held fixed, the allowable angle error $\delta\phi$ decreases as the range increases and goes to zero at a range $R_m$, where from (99),

$$R_m \triangleq \frac{D(\delta R)_{rms}}{\delta D}\,.$$

When $R > R_m$, the range error exceeds $(\delta R)_{rms}$ even for $\delta\phi = 0$.

In practice, however, the allowable range error increases with the range and has its minimum value at minimum range. Taking the minimum range to be 25 ft, Figure 60 shows that the required angular precision to ensure $(\delta R)_{rms}$ values of 0.5, 1, and 2 ft at this distance is 9.8, 19 7, and 39 3 milliradians, respectively All of these values are achievable with closed-loop trackers, and at least the larger two are also compatible with manual trackers. If these $\delta\phi$ values are held fixed (as in a real system), then the range error increases with R as shown in Figure 61. Although the error is quite large beyond 100 ft or so, it should be tolerable at such distances, provided the satellite is not closing too rapidly. Also, these values can be reduced by

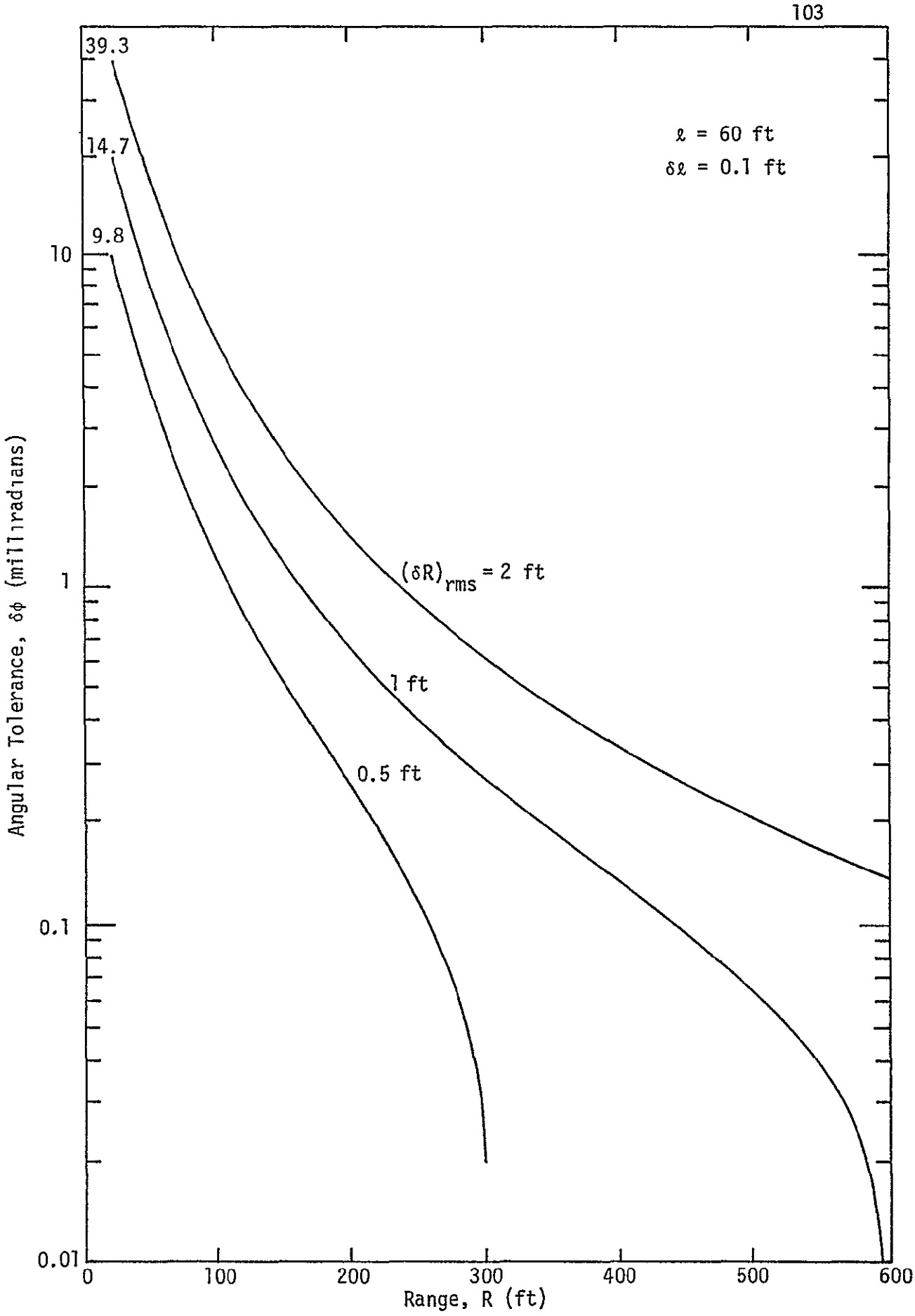


Figure 60. Angle Error Budget Versus Range for Fixed RMS Range Precision

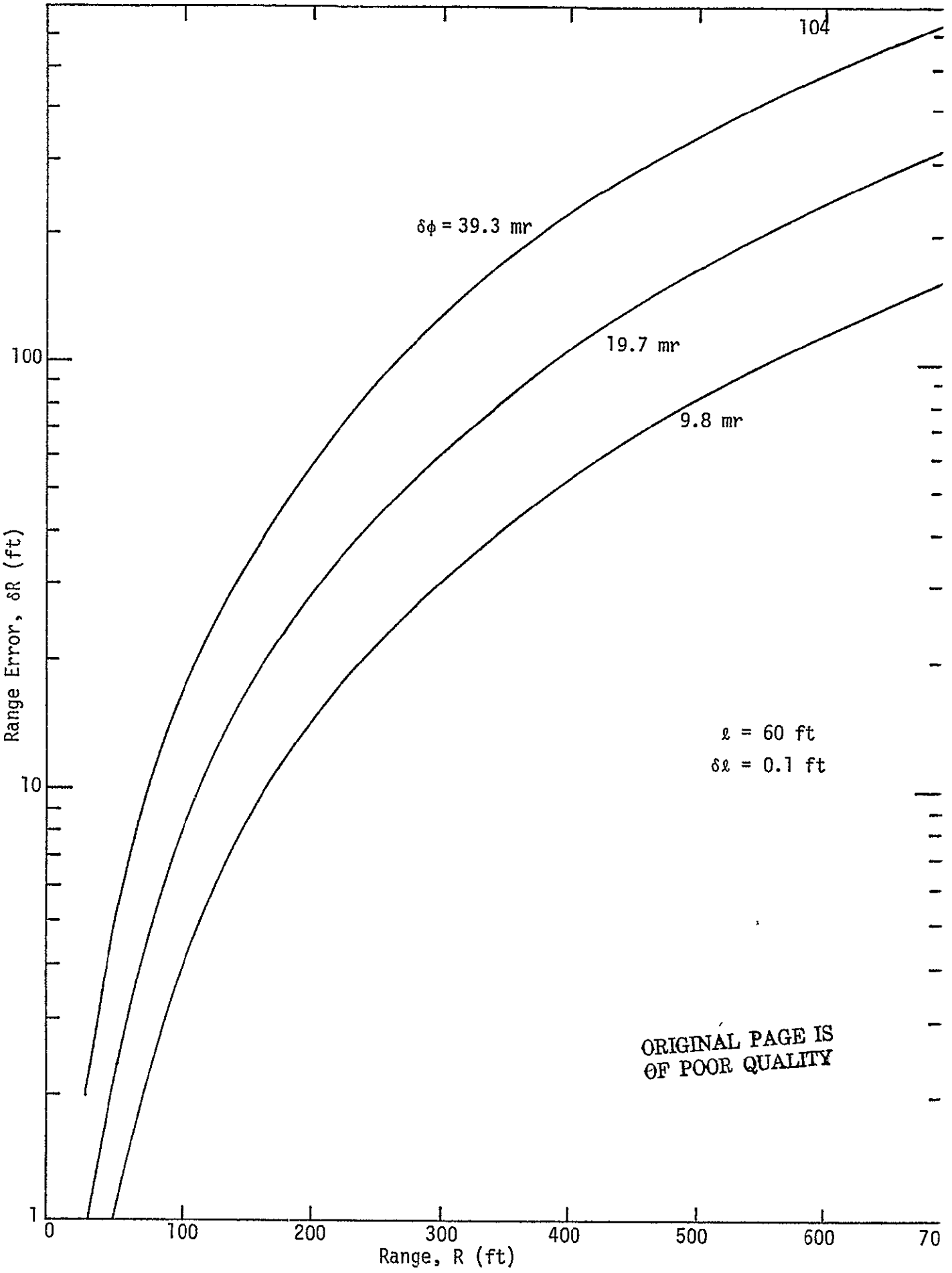


Figure 61. RMS Range Error Versus Range for Fixed Angle Error

further restricting the angle error tolerance $\delta\phi$, particularly if closed-loop trackers are employed.

Error Analysis for $\dot{R}$

The corresponding formulas for range rate $\dot{R}$ and range rate error $\delta\dot{R}$ follow in similar fashion after taking the time derivative of (97):

$$R = D \cot \phi$$

$$\dot{R}(\phi,\dot{\phi}) = -D \csc^2 \phi \, \dot{\phi} \qquad (\dot{D} = 0) . \tag{100}$$

In this case, variations in $\dot{R}$ can arise from variations in the measurement of $\phi$, $\dot{\phi}$, or D. Hence, from (100) and Figure 59:

$$(\delta\dot{R})_{\phi} = -2D \csc \phi \, (-\cot \phi \csc \phi) \, \dot{\phi} \, \delta\phi = -2(-D \csc^2 \phi \, \dot{\phi}) \cot \phi \, \delta\phi$$

$$= -2 \dot{R}(R/D) \, \delta\phi$$

$$(\delta\dot{R})_{\dot{\phi}} = -D \csc^2 \phi \, \delta\dot{\phi}$$

$$= -\frac{R^2 + D^2}{D} \delta\dot{\phi}$$

$$(\delta\dot{R})_{D} = -\csc^2 \phi \, \dot{\phi} \, \delta D$$

$$= \dot{R}(\delta D/D) ,$$

so

$$(\delta\dot{R})_{rms} = \sqrt{(\delta\dot{R})_{\phi}^2 + (\delta R)_{\dot{\phi}}^2 + (\delta\dot{R})_{D}^2}$$

$$= \sqrt{\left[(2R/D)^2(\delta\phi)^2 + (\delta D/D)^2\right] \dot{R}^2 + \left(\frac{R^2 + D^2}{D}\right)^2 (\delta\dot{\phi})^2} \tag{101}$$

and

$$\delta\dot{\phi} = \frac{D}{R^2 + D^2} \sqrt{(\delta\dot{R})_{rms}^2 - \left[(2R/D)^2(\delta\phi)^2 + (\delta D/D)^2\right]\dot{R}^2} . \tag{102}$$

## 5.2 Direct Rangefinder (No Angle Measurement)

This method employs two independent rangefinders to measure the legs a and b of the range triangle. If the baseline $\ell$ is also known,

the perpendicular range to the satellite can be determined. Although no angle measurements are used, an automatic system would require closed-loop angle trackers to point the lasers continuously at the satellite. These trackers could also provide an independent and redundant range determination based on the triangular method (section 5.1). However, if the lasers are pointed manually, no trackers are needed.

The desired expression for range R in terms of a, b, and $\ell$ is easily deduced (in the co-planar case) from the geometry of Figure 58. By the law of cosines,

$$\cos \beta = \frac{a^2 + \ell^2 - b^2}{2a\ell}$$

and

$$R^2 = a^2 - (a \cos \beta)^2$$

$$R = a\sqrt{1 - \left(\frac{a^2 + \ell^2 - b^2}{2a\ell}\right)^2} \qquad (103)$$

In the special case when $\alpha = \beta$, $a = b$,

$$R = a\sqrt{1 - \left(\frac{\ell}{2a}\right)^2} = \sqrt{a^2 - D^2}\,, \qquad (104a)$$

where $D \triangleq \ell/2$.

Error Analysis

Squaring (104a) gives

$$R^2 = a^2 - D^2\,. \qquad (104b)$$

Hence,

$$R\,(\delta R)_a = a\,\delta a$$

$$R\,(\delta R)_D = -D\,\delta D\,,$$

so

$$(\delta R)_{rms} = \sqrt{(\delta R_a)^2 + (\delta R_D)^2} = \frac{1}{R}\sqrt{a^2(\delta a)^2 + D^2(\delta D)^2} \qquad (105)$$

and

$$\delta a = \frac{1}{a}\sqrt{R^2(\delta R)^2_{rms} - D^2(\delta D)^2}\,, \tag{106}$$

where $\delta a$ is the rangefinder precision required to ensure a perpendicular range accuracy of $(\delta R)_{rms}$ ft at range R, for specified $\delta D$.

The angle error can be similarly found to be equal to

$$(\delta\beta)_{rms} = \frac{\sqrt{(\delta D)^2 + (D/a)^2(\delta a)^2}}{R}\,.$$

If D is known without error, then the rms angle error can be written as

$$(\delta\beta)_{rms} = \frac{D\ \delta a}{R\sqrt{R^2 + D^2}}\,.$$

## 5.3 Description of Electro-Optical Concepts

In this section, various electro-optical concepts for implementing the ranging techniques of section 5.2 are described, and recommended concepts are selected for cooperative and noncooperative satellites. All of the concepts considered derive the necessary geometrical information by measuring the distance or angular position of a fixed reference point on the approaching satellite by means of two EO sensors positioned at either the same or opposite ends of the platform baseline. The satellite reference point may be either self-luminous (beacon concept) or illuminated by a laser (or lasers) located on the platform (laser/retro or laser spot tracker concepts).

Purely passive concepts such as tracking the satellite by solar illumination or thermal (black-body) radiation have not been examined in detail because the former is too variable and unreliable while the latter presents a radiation signature that is too weak and spatially diffuse for accurate terminal guidance, particularly in the presence of strong celestial or earth backgrounds

The sensors considered are all designed to operate over a limited field of view. While some are nulling devices, some means must be employed to steer the sensors continuously This is because

the angular position of the reference point changes during satellite approach. The same capability is required for the lasers, which produce an inherently narrow beam that must be kept continuously on the illuminated reference point in order to ensure an accurate range or angle measurement.

The necessary steering capability can be provided by one or both of the following methods: (1) manual steering of either one or two television systems fitted with viewing reticles and electrically slaved to the sensors and/or lasers, and (2) automatic steering by means of closed-loop trackers. The first method is essentially an open-loop approach which is limited by the achievable tracking precision of a human operator. Since suitable TVs are already available, this is an attractive possibility, provided the tracking jitter is not excessive.

The second method can provide much better tracking precision than manual tracking (a particularly important advantage with the triangulation technique). However, it is more complex since it requires a complete closed-loop servo control system, and it does not provide automatic acquisition unless a special acquisition mode is designed into it. (A hybrid approach, combining manual TV acquisition with handover to closed-loop tracking, is also a very practical solution to this particular problem.)

Several types of two-axis tracking sensors can be considered for closed-loop trackers. Among these are silicon quadrant or continuous-position sensing detectors (for visible and near-IR wavelengths) and moving-reticle type star trackers using a photomultiplier tube. All of these sense the displacement of an optical image of a point source relative to two orthogonal axes (e.g., azimuth and elevation) and thereby measure the angular position of the satellite reference point with respect to the instantaneous line of sight (LOS). The resulting error signal can be used to command a closed-loop servo system. Shaft angle encoders would be needed to measure the net LOS rotation relative to coordinate axes fixed in the docking platform, as required for the triangulation technique

Although closed-loop TV tracking is technically feasible, it has been excluded from detailed consideration because of its complexity and cost relative to other methods. It should be noted, however, that TV

trackers are especially vulnerable to image blooming and tube failure resulting from excessive image brightness such as might occur due to a strong sunglint off the satellite.

### 5.3.1 Cooperative Satellites

A cooperative satellite is defined to be one that carries with it one of the active or passive components of a complete docking system. For the EO system considered here, this component may be either a beacon or a retro-reflector array. The beacon may be activated either from on-board the satellite or remotely, by a signal transmitted from the docking platform. (In the latter case, it would be regarded as a transponder.) Pulsed operation is preferable to a CW mode, both to conserve average power and to aid in background discrimination. If a retro array is used, a suitable laser or other high intensity illumination source must be made available on the platform.

Both the beacon and the reflector array provide a tracking/ranging reference point that has a fixed location on the satellite, contributing to more stable tracking than can be achieved by tracking a laser-illuminated spot on the skin of the satellite. This tracking reference is also generally much brighter than the illuminated skin and therefore produces higher signal-to-noise ratios in the tracker.

#### Beacon

The beacon concept utilizes ranging by the triangulation method. It was shown in section 5.1 that this method is capable of achieving sufficient range precision at minimum range, using closed-loop trackers of ordinary accuracy. (The adequacy of manual TV tracking is less certain, but this technique may also be viable.) If the precision achievable beyond the minimum range is also deemed acceptable (see Figure 61), then the beacon is the preferred concept for cooperative satellites because (1) no active sources are needed on the docking station; (2) manual acquisition via TV is easily implemented by slaving the tracking sensors to the TV line-of-sight (the sensor's field of view must be large enough to accommodate LOS differences due to parallax); (3) problems associated with pointing of a laser illuminator or range-finder are avoided; and (4) the beacon provides a strong, reliable signal exhibiting less fluctuation than is present with other methods.

The primary drawback of a beacon for a cooperative satellite is that it consumes some spacecraft power. It also requires timely maintenance to ensure that it operates reliably at the time of docking.

The following two types of beacons are viable candidates:

(a) Xenon Aircraft Beacon (Recommended Concept). The Xe beacon is recommended over other alternatives subject to the proviso that excessive spectral filtering is not needed to contend with sunglint background. If such filtering should be found necessary (through later analysis) and results in unacceptable signal loss, then the Gallium Arsenide beacon described below would be favored instead, because of its intrinsically narrowband output.

Aside from the question of the filtering required, if any, the Xenon beacon is a highly attractive concept for cooperative satellites because of its wide beam, visibility, TV-compatible output spectrum, and because it is a standard catalog item requiring only minimal interfacing design. A small, pulsed beacon drawing a few watts of average power should be sufficient for docking control out to a range of at least 1000 ft. It may be advisable to include a simple reflector to confine the beam to the forward hemisphere, thereby increasing the intensity relative to the isotropic mode.

(b) Gallium Arsenide (GaAs) Beacon. This device consists of a close-packed array of GaAs laser diodes with an associated pulse and simple optics to project the beam. Arrays and pulsers are commercially available Uncoded GaAs diodes emit at a wavelength of about 0.9 μm (900 nm) in the near-infrared, unless special doping is used to shift the output to a shorter wavelength. Aluminum-doped GaAs (GaAlAs) diodes emitting at wavelengths of 0.8 μm or less can be obtained from at least one commercial vendor at the cost of somewhat reduced peak power per diode. This expedient may be necessary to make the beacon visible to the TV for tracking and/or acquisition. Even so, a TV with an extended-red response may be required.

The raw output beam from a GaAs diode array tends toward a conical shape having a full-angle divergence on the order of 30 degrees at the 50% intensity points. By the use of a simple optical mixer or "scrambler," the output can be made highly uniform, and it is then particularly well

suited for a wide-angle beacon, with little or no additional optics. The requisite intensity is achieved by employing a sufficient number of diodes in the array. Since the individual diodes are typically only a few mils wide in the longer face dimension, the overall size of the array is quite small, and it is relatively lightweight.

Cooled GaAs arrays offer substantially higher average power and efficiency and also emit at a slightly shorter wavelength. However, for the present application, these advantages are more than offset by the additional complexity and maintenance requirements of the associated cryogenics. Hence, an uncooled array is recommended unless further analysis shows that adequate intensity cannot be achieved without cooling.*

In comparison to the Xenon beacon, the GaAs beacon offers the advantage of an intrinsically narrow output spectrum (helpful for background discrimination), compact design (if cryogenic cooling is not required), potentially lower power consumption (depending on the array size and beamwidth employed), and possibly longer service-free intervals. On the other hand, the GaAs beacon is power-limited to a relatively narrow beam and hence imposes some constraints on satellite orientation, and its infrared output is poorly matched to the spectral response of the TV. Further analysis will be needed to make a definitive choice between these alternatives.

Laser/Retro

This concept utilizes a retro-reflector array on the satellite and one or two lasers on the docking platform. Several types of reflectors may be considered. If the array is comprised of individual corner-cube reflectors, the return beam will be highly directional and will only be visible to a sensor co-located with the laser. Other devices for enhancing the laser return include glass-bead type reflectors and reflective tape, which tend to be somewhat less directional than corner-cube reflectors. A fairly broad return beam is necessary if a tracking sensor is to be located at the opposite end of the baseline from the laser.

*Radiative cooling to space may be an effective alternative to cryogenic cooling and should be considered.

Because of their narrow beams, the lasers must be pointed continuously at the retro as the satellite closes in range. Steering can be accomplished by either of two methods. First, the beam divergence may be increased sufficiently (using external optics) to permit manual TV steering, provided that a sufficient SNR can be maintained with the broadened beam. Alternately, a closed-loop tracker (or trackers) can be employed. In this case, the beam(s) must be nutated or conically scanned about its axis to generate a tracking signal, while its divergence must be compatible with the tracking accuracy, jitter and lag of the tracker, to ensure that the beam does not drift off the retro.

With either open-loop or closed-loop tracking, acquisition can be achieved by manually pointing with a wide beam, using radar data to define the uncertainty volume. Acquisition will be signaled by the appearance of a bright spot on the TV monitor. The beam divergence can then be reduced, if desired, to improve the SNR for closed-loop tracking.

The laser/retro concept can be implemented in several ways, the principal ones being the following:

(a) One laser illuminator/rangefinder, one angle tracker. In this method, a CW-modulated laser serves as both a rangefinder transmitter, with a co-located receiver, and as an illuminator for an angle tracker, also co-located with the transmitter. This hybrid system measures the length and angle of one side of the range triangle and hence represents a combination of the rangefinding and triangulation techniques.

(b) Two laser rangefinders. This range-only approach measures the lengths of the two legs of the triangle, as described in section 5.2. If corner-cube retros are used, the two return beams will be isolated from each other in angle (each laser/sensor "sees" a different retroreflector of the array) and lasers of the same wavelength can be employed. Otherwise, different wavelengths and spectral filters should be used to prevent possible mutual interference from overlapping beams. By the addition of one or two angle trackers, as in (a), the system can provide a redundant or backup determination of range by triangulation.

(c) Two laser illuminators/trackers. This variation uses the lasers only as illuminators for their associated angle trackers, and perpendicular range is obtained by triangulation. Two illuminators

are needed only if corner-cube or other highly directional retro reflectors are used on the satellite.

The laser/retro concept shares most of the virtues of the beacon, with the additional advantage that the satellite is required to carry only a passive device that consumes no power. Of course, this simply transfers the active device to the docking platform. Another significant advantage is that an illuminator or rangefinder laser can also be used for tracking/ranging noncooperative satellites, as described in the following section, whereas beacon systems cannot.

The major disadvantages of the laser/retro concept are the potential difficulty in acquiring the retro with a laser and the possible requirement for a closed-loop laser pointing and tracking system, which would substantially increase the complexity and cost relative to the beacon system.

Searchlight/Retro

This concept envisions high-intensity, noncoherent, broad-beam sources on the platform to floodlight the entire satellite as it approaches. Little or no steering of the sources would be required. The retro-reflectors would appear as relatively bright points against a lesser background of random glints and diffuse reflection from the skin of the satellite. By properly thresholding the tracking sensors, it should be possible to discriminate against this background In other respects, the concept is identical to the two-laser illuminator/tracker method described above.

Possible sources include the Xenon and GaAs beacons discussed earlier, situated on the platform rather than on the satellite. The major uncertainty concerns the source power necessary to provide a sufficient retro-return at maximum range. Otherwise, the concept is an attractive one, since steering requirements are minimal.

### 5.3.2 Noncooperative Satellites

As noted earlier, passive tracking methods based on solar reflection or thermal emission from the satellite do not appear to be viable candidates for this application. Consequently, only active EO concepts using lasers (or possibly other high intensity sources) on the docking

platform need to be considered for noncooperative satellites. Furthermore, the requirement for a well-defined tracking point excludes broad-beam sources that would floodlight the satellite, since the multiple glints produced would only confuse a tracking sensor. Thus, the only viable approaches for passive satellites are those involving lasers on the station, since they are capable of illuminating a small spot at ranges of 1000 ft or more.

The options available with lasers are basically similar to those for the laser/retro concept, as described above, except that the beams are reflected from the skin of the satellite instead of from a retro-reflector assembly. However, certain important differences should be noted.

First, since no retro is involved, the reference point must be designated by the operator during acquisition. This point should be selected to minimize the changes of drifting off the target, i.e., it should lie within the main body of the satellite and not on one of its extremities. If manual tracking is employed, some experimentation may be necessary to determine an optimum spot size· a small spot maximizes the brightness and defines the best reference point, but a larger spot (wider beam) is less sensitive to pointing jitter.

A second difference is that skin tracking permits a single laser illuminator to be used with two tracking sensors, since the spot is visible from different positions (this is not possible with a retro). On the other hand, this same property makes it necessary to use separate wavelengths if the two-laser rangefinder method is employed.

Finally, reflection from the satellite skin provides a much weaker and more variable intensity than that possible with a retro. Hence,the tracker SNR will be lower and tracking or ranging may be degraded unless more powerful lasers are used.

Although several implementations of skin tracking and ranging appear viable, a particularly attractive method is to use a single laser illuminator/rangefinder with a co-located rangefinder-tracker receiver and a second separate tracker at the opposite end of the baseline. This system would provide a redundant range determination by triangulation (two trackers) and by ranging and tracking (hybrid).

# REFERENCES


1. C. L. Weber, W. K. Alem, and M. K. Simon. "Study to Investigate and Evaluate Means of Optimizing the Ku-Band Combined Radar/Communication Functions for the Space Shuttle," Axiomatix Report No. R7710-5, October 28, 1977.

2. Hughes Aircraft Company Monthly Review, Viewgraph No. 76544-7, December 1977.

3. P. A. McCollum and B. F. Brown. Laplace Transform Tables. Oklahoma Engineering Experiment Station, Oklahoma State University, Publication No. 137, 1964.

4. C. L. Weber. "Optimization of Proposed Radar for the Ku-Band Radar-Communication System," Appendix A, Axiomatix Report No. R7408-5, August 22, 1974.

5. N. Nahi. Estimation Theory and Applications. Wiley, 1969.

6. C. Chen. Introduction to Linear System Theory Holt, Rinehart, and Winston, 1970.

7. L. K. Timothy and B. E. Bona. State Space Analyses. An Introduction. McGraw-Hill, 1968.

8. B. Friedman. Principles and Techniques of Applied Mathematics. Wiley, 1956.

9. D. Childers and A. Durling. Digital Filters and Signal Processing. West Publishing Company, 1975.

10. E I. Jerry. Theory and Application of the Z-Transform Method. Wiley, 1964.

11. D. K. Barton. Radar System Analysis Prentice-Hall, 1964.

12. D. K. Barton and H. R. Ward. Handbook of Radar Measurement. Prentice-Hall, 1969.

13. Aviation Week, November 7, 1977, pp. 24-25.

# APPENDIX A

## MODELING A CONTINUOUS STOCHASTIC PROCESS BY A DISCRETE TIME STOCHASTIC PROCESS

In this appendix, we determine precisely how a continuous random process is modeled by a discrete time process. The discrete time process can then be directly programmed on a digital computer. The primary interest here is in linear systems, so we restrict attention to a vector valued linear system. As a specific example, a scalar first-order constant coefficient linear system is modeled.

Consider the k-dimensional continuous time vector random process $\underline{x}(t)$, which is modeled by [A-1]:

$$\dot{\underline{x}}(t) = \underline{A}(t)\,\underline{x}(t) + \underline{B}(t)\,\underline{u}(t)\,, \tag{A-1}$$

where $\underline{A}(t)$ is a k×k matrix, $\underline{B}(t)$ is a k×r dimensional matrix, and $\underline{u}(t)$ is an r-dimensional vector white noise process with zero mean and covariance matrix:

$$E[\,\underline{u}(t_1)\,\underline{u}'(t_2)] = Q(t_1)\,\delta(t_2 - t_1)\,, \tag{A-2}$$

where $\delta$ represents the Dirac delta function and (') represents the transpose vector.

We wish to model the continuous system by the discrete time linear system

$$\underline{x}(k+1) = \underline{A}(k)\,\underline{x}(k) + \underline{B}(k)\,\underline{u}(k)\,, \tag{A-3}$$

where the dimensionality of the matrices and vectors in (A-3) is identical to those in (A-1). By modeling, we explicitly mean that the first- and second-order statistics of $\underline{x}(k)$ will be identical to those of $\underline{x}(t)$ at the time $t = kT$, where T is the sampling period of the discrete time process The time T can also be interpreted as the update time of the digital computer, whether this be a real-time or an off-line modeling process.

In our model, we will make use of the state transition matrix [A-2], $\underline{\Phi}(t)$, which is the solution of the differential equation

$$\dot{\underline{\Phi}}(t) = \underline{A}(t)\,\underline{\Phi}(t)$$

$$\underline{\Phi}(0) = \underline{I} \,. \tag{A-4}$$

In the special case where A(t) is a constant, i.e , A(t) = A, then

$$\underline{\Phi}(t) = \exp(\underline{A}t), \qquad t \geq 0 .$$

Continuous System Model

Equation (A-1) is a continuous linear first-order differential equation and has the explicit solution

$$\underline{x}(t) = \underline{\Phi}(t)\left\{\underline{x}(0) + \int_0^t \underline{\Phi}^{-1}(\tau)\,\underline{B}(\tau)\,\underline{u}(\tau)\,d\tau\right\}, \; t \geq 0, \tag{A-5}$$

where $\underline{x}(0)$ is the initial value of $\underline{x}(t)$ at $t = 0$. At time kT, the continuous system in (A-5) can be written as

$$\underline{x}(t) = \underline{\Phi}(kT)\left\{\underline{x}(0) + \int_0^{kT} \underline{\Phi}^{-1}(\tau)\,\underline{B}(\tau)\,\underline{u}(\tau)\,d\tau\right\}, \tag{A-6}$$

and at time (k+1)T, it becomes

$$\begin{aligned}\underline{x}((k+1)T) &= \underline{\Phi}((k+1)T)\left\{\underline{x}(0) + \int_0^{kT} \underline{\Phi}^{-1}(\tau)\,\underline{B}(\tau)\,\underline{u}(\tau)\,d\tau \right.\\ &\qquad \left. + \int_{kT}^{(k+1)T} \underline{\Phi}^{-1}(\tau)\,\underline{B}(\tau)\,\underline{u}(\tau)\,d\tau\right\}\\ &= \underline{\Phi}((k+1)T)\left\{\underline{\Phi}^{-1}(kT)\,\underline{x}(kT) + \int_{kT}^{(k+1)T} \underline{\Phi}^{-1}(\tau)\,\underline{B}(\tau)\,\underline{u}(\tau)\,d\tau\right\}.\end{aligned} \tag{A-7}$$

Therefore, for the continuous time system, we have that

$$\underline{x}((k+1)T) = \underline{\Phi}((k+1)T)\,\underline{\Phi}^{-1}(kT)\,\underline{x}(kT) + \underline{\Phi}((k+1)T)\int_{kT}^{(k+1)T} \underline{\Phi}^{-1}(\tau)\,\underline{B}(\tau)\,\underline{u}(\tau)\,d\tau \tag{A-8}$$

from which the expected value is given by

$$E[\underline{x}(k+1)T] = \underline{\Phi}((k+1)T)\,\underline{\Phi}^{-1}(kT)\,E[\underline{x}(kT)] \tag{A-9}$$

and the covariance matrix at time (k+1)T is

$$\text{cov}[\underline{x}(k+1)T] = \underline{\Phi}((k+1)T)\int_{kT}^{(k+1)T}\underline{\Phi}^{-1}(\tau)\,\underline{B}(\tau)\,\underline{Q}(\tau)\,\underline{B}'(\tau)[\underline{\Phi}^{-1}(\tau)]'\,d\tau\;\underline{\Phi}^{-1}((k+1)T) \tag{A-10}$$

Discrete System Model

Similar expressions are obtained for the discrete time model via (A-3). In particular, the mean is given by

$$E[\underline{x}(k+1)] = \underline{A}(k)\,E[\underline{x}(k)] \tag{A-11}$$

and the covariance matrix is

$$\text{cov}[\underline{x}(k+1)] = \underline{B}(k)\,E[\underline{u}(k)\,\underline{u}'(k)]\,\underline{B}'(k)\,. \tag{A-12}$$

Equating Discrete and Continuous Time Models

In order for the first moment of the discrete time model to be equal to that of the continuous model requires that $E[\underline{x}(k+1)]$ in (A-11) be equal to $E[\underline{x}(k+1)T]$ in (A-9) for all k. This is the case when

$$\underline{A}(k) = \underline{\Phi}((k+1)T)\,\underline{\Phi}^{-1}(kT)\,. \tag{A-13}$$

The second-order statistics become equal when $\text{cov}[\underline{x}(k+1)]$ in (A-12) is equal to $\text{cov}[\underline{x}((k+1)T)]$ in (A-10) for all k. This provides the requirement that

$$\underline{B}(k)\,E[\underline{u}(k)\,\underline{u}'(k)]\,\underline{B}'(k) = \underline{\Phi}((k+1)T)\int_{kT}^{(k+1)T}\underline{\Phi}^{-1}(\tau)\,\underline{B}(\tau)\,\underline{Q}(\tau)\,\underline{B}'(\tau)[\underline{\Phi}^{-1}(\tau)]'\,d\tau\;\underline{\Phi}'((k+1)T) \tag{A-14}$$

These results are applied to specific one-dimensional cases which are used throughout the radar simulation.

Example 1. Consider the one-dimensional version of (A-1) where the coefficients are constants. Therefore,

$$A(t) = A$$

$$B(t) = B$$

and

$$\Phi(t) = \exp(At) \tag{A-15}$$

Also, let the correlation function of $u(t)$ be $Q(\tau) = (N_0/2)\,\delta(\tau)$, where $N_0$ is the one-sided power spectral density of the white Gaussian source noise in watts/Hertz.

Then, from (A-13),

$$A(k) = \exp[A(k+1)T]\exp(-AkT)$$

so that

$$A(k) = \exp(AT), \tag{A-16}$$

which is a constant depending only on the parameters A in (A-14) and the computer update time T.

Similarly, from (A-14),

$$B^2(k)\,E[u^2(k)] = \exp[2A(k+1)T]\int_{kT}^{(k+1)T}\exp(-A\tau)\,B^2(N_0/2)\exp(-A\tau)\,d\tau \tag{A-17}$$

which reduces to

$$B^2(k)\,E[u^2(k)] = \frac{N_0B^2}{4A}\exp(2AT)[1-\exp(-2AT)] \tag{A-18a}$$

or, equivalently,

$$B^2(k)\,E[u^2(k)] = \frac{N_0B^2}{2A}\exp(AT)\sinh(AT)\,. \tag{A-18b}$$

In a stable system, A in (A-14) will be less than zero. Then, when $T\to\infty$,

$$B^2(k)\,E[u^2(k)] = \frac{N_0B^2}{4|A|}\,, \tag{A-19}$$

which from (A-12) can be seen to also be the variance of $x(k+1)$, i.e.,

$$\lim_{T \to \infty} E\left[(x(k+1))^2\right] = N_0 B^2/(4|A|) \ . \qquad \text{(A-20)}$$

By letting $T \to \infty$ in the continuous time representation in (A-6), the same result is obtained.

Example 2. Consider the case of white noise through a first-order Butterworth (RC) filter, as shown in Figure A-1.

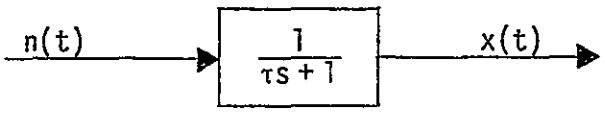


Figure A-1. White Noise Through a First-Order Filter

The white noise has one-sided PSD of $N_0$ watts/Hz and the filter time constant is $\tau$. The differential equation for the filter in Figure A-1 is

$$\dot{x}(t) = (-1/\tau)\, x(t) + (1/\tau)\, n(t) \qquad \text{(A-21)}$$

where when compared to (A-14) and (A-1), it is seen that

$$A = -1/\tau$$

$$B = 1/\tau \ . \qquad \text{(A-22)}$$

From (A-16), the constant A(k) in the discrete time model is

$$A(k) = \exp\,(-T/\tau) \qquad \text{(A-23)}$$

and, from (A-18)

$$B^2(k)\, E\left[u^2(k)\right] = \frac{N_0 (1/\tau)^2}{2(-1/\tau)} \exp\,(-T/\tau) \sinh\,(-T/\tau) \ . \qquad \text{(A-24)}$$

In (A-24), either B(k) or $E[u^2(k)]$ can be chosen arbitrarily. If we elect to set

$$B(k) = 1 \ , \qquad \text{(A-25)}$$

then

$$E[u^2(k)] = \left(\frac{N_0}{2T}\right)\left(\frac{T}{\tau}\right) \exp(-T/\tau) \sinh(T/\tau). \qquad \text{(A-26)}$$

A block diagram of the model is shown in Figure A-2. The output of the random noise generator (RNG) is a Gaussian random variable with zero mean and unit variance. The sample of u(k) is obtained by scaling this random variable by the standard deviation of u(k). The resulting sequence of random variables {x(k)} will have first- and second-order statistics which are identical to those of x(t) in Figure A-1 at times t = kT

As the sampling time approaches infinity ($T \to \infty$), $A(k) \to 0$, which implies that the samples are independent as is logically anticipated. Also, (A-10) shows that the variance of any sample is equal to $N_0/4\tau$. This is also anticipated because it represents the steady-state variance at the output of an RC filter whose time constant is $\tau$. (The two-sided noise bandwidth of an RC filter $B_i = 1/2\tau$).

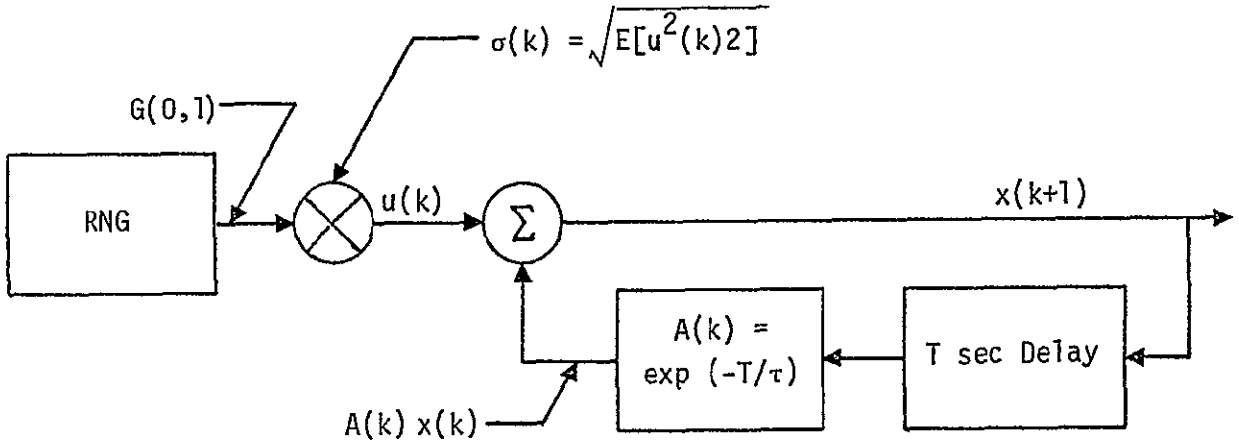


Figure A-2. Diagram of Discrete Time Model for First-Order Stochastic Process

# REFERENCES

A-1. N. E. Nahi. Estimation Theory and Applications. Wiley, 1969.

A-2. L D Zadeh and C. A. Desoer. Linear System Theory. McGraw-Hill, 1963.